TECHNICAL UNIVERSITY
OF CRETE

School of Electrical And Computer Engineering

DIPLOMA THESIS

Deconvolution microscopy based on modulation transfer function

---

by
Charalampos Boras

A thesis submitted in partial fulfillment of the requirements
for the Diploma of Electrical and Computer Engineering

in the

Electronics Laboratory
Department of Electrical and Computer Engineering

THESIS COMITTEE
Professor Costas Balas (Supervisor)
Professor George N. Karystinos
Professor Zervakis Michael

June 2019

Acknowledgements

After a series of unexpected events and situations that emerged during my undergraduate studies, I would like to thank the people who, with their role, have helped me to accomplish this important goal in my life.

First of all, I would like to thank my family, John, Voula and Panayotis, for the inexhaustible help and support they have provided me throughout my student life. Second, I would like to thank my wife, who believed in me, followed me and supported me, making my days better. I would also like to thank my supervisor, Professor Costa Balas, who gave me valuable knowledge and guidance in the field of optoelectronics and imaging diagnostics, as well as his trust, who accepted me in his team with his excellent support and cooperation.

Last but not least, I would like to thank my thesis advisor and colleague, Tsparas Athanasios, for giving me the inspiration and the will to learn and to work for new scientific fields. I also thank the other members of the workshop, who in any way I needed them, they were there to help me and share their knowledge.

Abstract

Due to the widespread use of the light microscope as a diagnostic tool for many scientific fields like medicine, biology, chemistry as well as for industrial applications, light microscopy has been undergoing vast and continuing innovations both regarding the hardware and software domain. The optical resolution of light microscopes is physically constrained by the phenomenon of diffraction. Out-of-focus light and light originated from adjacent areas of a sample are superposed degrading the quality of the image of the object under study. In this degradation, the Point Spread Function (PSF) of the optical system is the main culprit and it is the one that determines the optical resolution. This degradation effect can be eased by sophisticated and expensive confocal microscopy systems or reversed to some degree by much cheaper widefield deconvolution microscopy methods.

Deconvolution processes need a PSF as much as accurate it can be in order to provide satisfactory and realistic results. The description of the PSF can be done either by mathematical models or by experimental measurements. Experiments for this purpose include measurements of fluorescent microbeads as well as estimation of the Modulation Transfer Function (MTF) of the optical systems which finally yields the PSF.

However, the conditions of capturing a digital image and the type of noise attributed to the optical systems have led to the creation of many types of deconvolution algorithms that focus and manage these features in a different way. Thus, even a valid PSF of an optical system produces different results when using different algorithm. It is known that the visual perception does not always concur with the quantitative measurements of these processes and ultimately the human eye is making the final decision about the validity of the deconvolution results.

This diploma thesis, based on a previous study [28] of the same laboratory and using the experimental methods of extracting PSF and deconvolution, focuses on developing a method that attempts to provide a qualitative comparison of the deconvolution results, which is consistent and verifies visual perception. The method was based on specific variables, such as spatial resolution, noise and image contrast, which were considered to have the greatest contribution to the validity of a result. The final classification list of their algorithms is ranked according to their relative successful deconvolution in terms of satisfying these variables. Also, the resulting measurements indicate the behavior of each algorithm in combination with the selected PSF on each sample.

This work is integrated into a graphical user interface that provides all the tools for extracting experimental PSFs, implementing a range of iterative and non iterative, deconvolution-algorithms, qualitative analysis of deconvolution results to create ranking list and export statistics for creating completed reports in each experiment.

Contents

List of Figures

List of Tables

List of Abbreviations

ESF Edge Spread Function.

FISTA Fast Iterative Soft-Thresholding Algorithm.

FWHM Full Width at Half Maximum.

ICTM Iterative Constrained Tikhonov-Miller algorithm.

JVC Jansson-Van Cittert algorithm.

LSF Line Spread Function.

LW LandWeber algorithm.

MTF Modulation Transfer Function.

NA Numerical Aperture.

NIF Naive Inverse Filter.

OTF Optical Transfer Function.

PSF Point Spread Function.

RIF Regularized Inverse Filter.

RL Richardson Lucy algorithm.

RLTV Richardson Lucy - Total Variation algorithm.

SeDDaRA Self-Deconvolving Data Reconstruction Algorithm.

SNR Signal to Noise Ratio.

SSIM Structural SIMilarity index.

TRIF Tikhonov Regularized Inverse Filter.

Chapter 1

Introduction

The microscope is a tool that enables humans to magnify tiny objects and microorganisms so that they can see and study them. Due to this important feature it is used by many scientific fields such as medicine, biology and chemistry as well as industry. The wide range of applications of the microscope and the development of technology have produced enormous and continuous innovations in the field of microscopy. It is known that an optical system, such as a microscope, exhibits intrinsic physical constraints due to the characteristics of the components constituting it. As discussed in the next chapter, a subject under study is not depicted as it is in reality. In particular, its image is degraded due to many reasons including blur, glare, scatter of light and incoming photon related noise.Blur, is a degradation created by the phenomenon of diffraction of optical elements (e.g., lenses) and results in a reduction in the optical resolution of the sample. The way the blur overtakes and overlaps the neighboring areas of a sample can be expressed as a degradation function that characterizes an optical system.

With the help of digital imaging and image processing, this function, also known as Point Spread Function PSF, can be calculated and reverse the degradation by following a deconvolution method in order to extract in a more precise and optimal way, the information of the object under study. Deconvolution processes need a PSF as much as it can be in order to provide satisfactory and realistic results. The description of the PSF can be done either by mathematical models or by experimental measurements. Experiments for this purpose include measurement of fluorescent microbeads as well as estimation of the Modulation Transfer Function MTF of the optical systems which finally yields the PSF.

The various conditions of digital capture of an image and the various forms of deggradation that can be presented, otherwise affect the results of deconvolution even if a PSF is quite accurate. This fact has led to the development of many deconvolution algorithms that attempt to approach this problem in such a way as to achieve the best possible result. It is known that visual perception does not always coincide with the quantitative measurement of these processes and ultimately the human eye is the final decision about the validity of the deconvolution results.

This diploma thesis, based on a previous study [28] of the same laboratory and using the

experimental methods of extracting PSF and deconvolution, focuses on developing a method that attempts to provide a qualitative comparison of the deconvolution results, which is consistent and verifies visual perception. The method was based on specific variables, such as spatial resolution, noise and image contrast, which were considered to have the greatest contribution to the validity of a result. The final classification list of their algorithms is ranked according to their relative successful deconvolution in terms of satisfying these variables. Also, the resulting measurements indicate the behavior of each algorithm in combination with the selected PSF on each sample. This work is integrated into a graphical user interface that provides all the tools for extracting experimental PSFs, implementing a range of iterative and non iterative, deconvolution-algorithms, qualitative analysis of deconvolution results to create ranking list and export statistics for creating completed reports in each experiment.

In order for someone to be introduced to the above-mentioned matter, at first the basic physical concepts are gradually explained. Beginning with how lenses in general work, how their providing magnification is defined and in which way the optical resolution of an optical system is limited, one can get to know the basic stuff behind the field of optics. Then, the anatomy of a modern conventional microscope is described. At this point, the concept of fluorescence and the anatomy of a fluorescent microscope is explained, since the test images used in this thesis contain a fluorescence microscope.

Knowing the parts of an optical system and how the its provided images are physically degraded, one can go deeper into how a PSF can be mathematically modelled and how it can alternatively be experimentally measured. Since the blur effect in an image is mathematically described using the concept of convolution, then the de-convolution methods used for the de-blurring of the captured image are analyzed. Finally, it is described the development of the proposed method of qualitative assessment of deconvolution results which is driven around the investigation of selected characteristics.

Chapter 2

Background information and theory

2.1 Microscopy

Microscopy is the technical field of using microscopes to view objects and areas of objects that cannot be seen with the naked eye (objects that are not within the resolution range of the normal eye). There are three well-known branches of microscopy: optical, electron, and scanning probe microscopy. Optical (light) microscopy, which is the case of study, uses visible light and a system of lenses in order to project a magnified image of a specimen under study on the eye or on a camera sensor.

2.2 Magnification of lenses

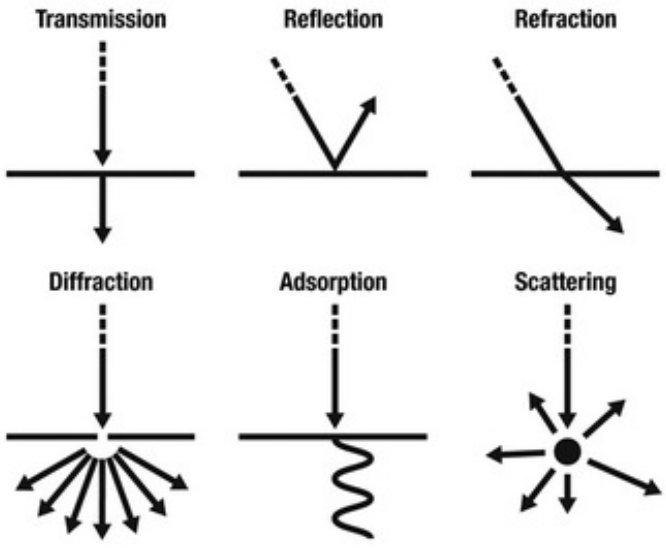

Figure 2.1: Principal interactions of light with a medium
Source:
`http://physicsweekly.weebly.com/reflection-refraction-and-diffraction.html`

Light can interact with a medium in many ways, depending on the material of themedium, the angle of the incidence and the wavelength. Figure 2.1 is self explanatory. As for diffraction (expounded in Sec.2.4.1), this phenomenon is based on theprincipals of constructive and destructive wave interference. Light behaves in thesame way as a mechanical wave encountering an obstacle or passing through a slit. Itis defined as the bending of light around the corners of an obstacle or a slit (aperture)into the region of geometrical shadow of the obstacle. In order to exhibit diffraction, this obstacle or this slit must be comparable in size with the wavelength of the encountering wave. From this, also it follows that an obstacle or a slit can have sharp edges. In microscopy, all these kinds of interaction are significant. Transmission, reflection, refraction are used to build a path for the light rays. Diffraction, absorption and scattering, though, eventually act as degrading factors for the microscoped image. For the purposes of light microscopy, the basic components relative to the optical train are lenses and filters.

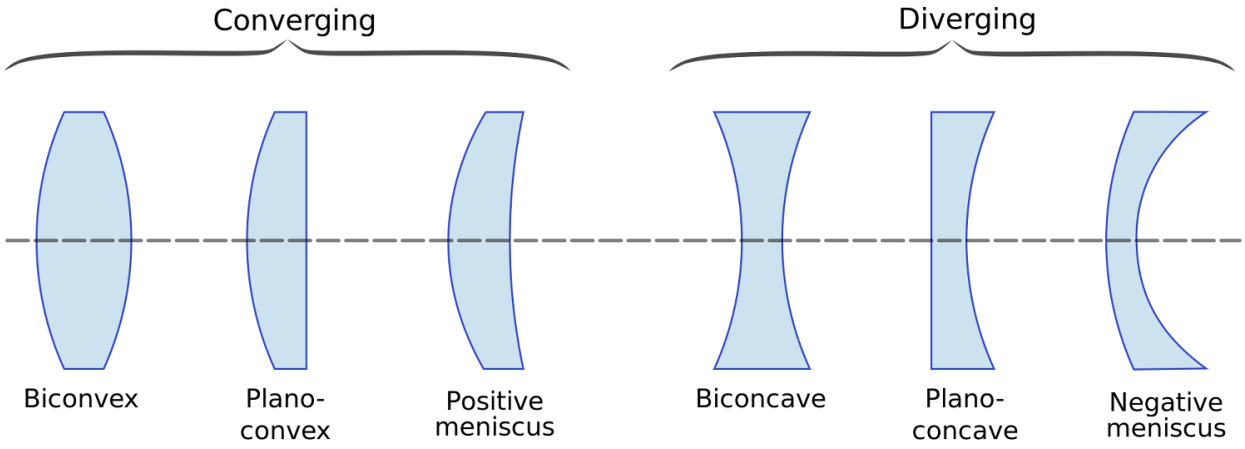

Figure 2.2: Different shapes of simple lenses
Source: `http://data.allenai.org/tqa/optics_L_0755/`

2.3 Lenses

Lenses come in different shapes (Fig. 2.2). They can be grouped and form a compound system with special properties (i.e better focusing, better magnification or eradication of aberrations). Two are the main characteristics of a lens. The distance over which initially parallel light rays are brought to a focus (focal length f) and the magnification. Image formation happens when light rays converge either in real or seem to do so (virtually). [10]

- A real image is formed in the plane where light rays converge in real (using converging lenses) and the object to be pictured is placed farther than the focal length of the lens. When the object is placed in between f and $2f$ the image is bigger than the object, whereas when it is placed in a distance bigger than $2f$ the image is smaller. A real image is always inverted and can be formed in a screen. For a converging lens, the focal length is said to be positive, which is the reason why they are also called positive.

- A virtual image is formed in the plane where light rays seem to converge (continuing ,virtually backwards, the rays coming out of the lens). This happens in diverging lenses or when the object to be pictured is placed inside the focal distance of a converging lens. A virtual image is always erect and cannot be projected onto a screen as it on the same side of the lens as the object.

2.3.1 Thin lenses

In the simple case of just one thin convex lens(thickness is negligible) (Fig. 2.3), the equation of the thin lens (Eq. 2.1) and the provided magnification (Eq. 2.2) can be computed, using the metric relations of the formed triangles: [12]

$$\frac{1}{s_1} + \frac{1}{s_2} = \frac{1}{f} \tag{2.1}$$

, where s_1: object to lens distance
$s2$: real image to lens distance
f: focal length

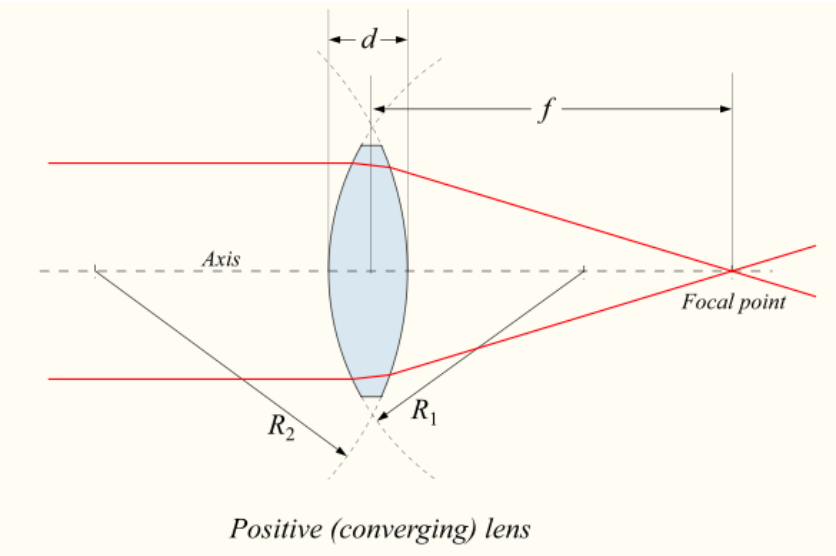

Figure 2.3: Image formation of an object with a convex lens
Source: `https://en.wikipedia.org/wiki/Lens_(optics)`

$$M = \frac{y_i}{y_o} = \frac{s_2}{s_1} \tag{2.2}$$

, where y_i: image height
y_o: object height

Usually, the object is put on the f_o, so the above equation becomes:

$$M = \frac{y_i}{y_o} = \frac{s_2}{f_o} \tag{2.3}$$

2.3.2 Lenses with important thickness

When the thickness of the lens is not negligible, in order to compute the effective focal length, radii of the curvature (RoC) of each side of the lens, along with the refractive index (r.i) of the lens medium must be known. So the corresponding equation is:

$$\frac{1}{f} = (n-1)\left[\frac{1}{R_1} - \frac{1}{R_2} + \frac{(n-1)d}{nR_1R_2}\right] \tag{2.4}$$

, where R_1: RoC of closer to the light source lens side
R_2: RoC of farther to the light source lens side n: r.i of the lens medium
d: lens thickness

2.3.3 Two lenses system (thin lenses)

A compound microscope system of two lenses provides better magnification than that of one lens. It consists of at least two converging lenses; the objective and the eyepiece. The former has a focal length $f_o < 1\,cm$ and the latter has a f_e of a few cm. The total magnification M of the two lenses is given by the product of the magnifications of the individual lenses. Thus, we have:

$$M = M_{objective} \times M_{eyepiece} \tag{2.5}$$

The individual magnifications are given by Eq. 2.2, which in order lead to:

$$M = \frac{S_2}{S_1} \times \frac{S_2^{'}}{S_1^{'}} \tag{2.6}$$

The distances between object-objective lens S_1, objective lens-real (first) image S_2 and real image-eyepiece lens $S_1^{'}$ may vary. But the distance between the eyepiece lens and the virtual (final) image $S_2^{'}$ is set to $25cm$. This is because $25cm$ is the closest point at which an object can be brought into focus by a "normal" human eye. Closest distance is important, because apparently the image of the object will be the most detailed it can be. Eventually, the eye perceives the final magnified image as if it were in that distance of $25cm$.

When the object is put on the f_o, the intermediate image is formed on the f_e. Hence the above equation becomes:

$$M = \frac{T}{f_o} \times \frac{25\,cm}{f_e} \tag{2.7}$$

, where T: distance between f_o and f_e, usually $16\,cm$

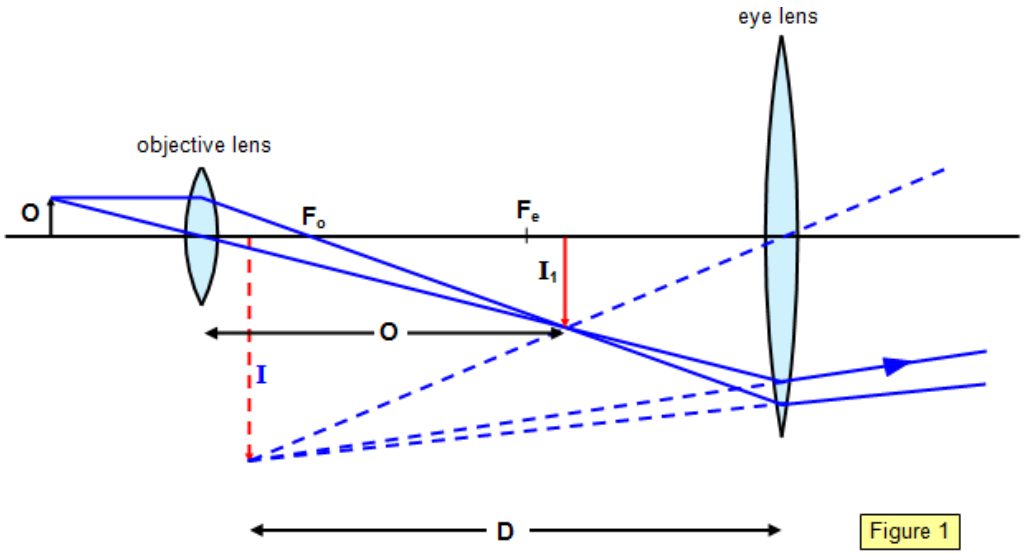

Figure 2.4: An objective-eyepiece compound
Source: https://physics.stackexchange.com/questions/307050/why-we-take-objective-of-short-focal-length-and-eye-piece-of-long-focal-length-i

2.3.4 Conventional microscope lenses

In a typical microscope a third lens is added, namely the tube lens, for the reason that the objective lens projects incoming light into infinity. The tube lens forms the real image on its focal point. Light rays originating from the two ends of the object are adequate for the purpose of explaining conventional microscope lenses. To take it from the start: The objective (Fig. 2.5(2)) is designed to project the incoming light rays of the object (Fig. 2.5(1)) into infinity. Then, the tube lens (Fig. 2.5(3)) produces a magnified intermediate image (Fig. 2.5(4)) which in turn is captured by the eyepiece (Fig. 2.5(5)) and finally shown to the eye (Fig. 2.5(6)). The resulting viewing angle δ_1 of the case A is much larger than δ_2 of case B, where the object is seen directly from a distance of approximately 25 cm. Regarding the overall magnification of such a system, it can computed by the product of the individual magnifications of the objective and the eyepiece lenses. [11]

2.3.5 Using an image capturing system instead of the eyepiece

In cases that recording of the specimen in an imaging system of a sensor and a computer monitor is preferred, the eyepiece can be omitted. The magnification is produced by the optical system (i.e objective, tube lens) and the electronic imaging system which provides a magnification factor due to the optical to electronic system adaptor (computer monitor adaptor). The total magnification of the system can be computed as:

$$M_{overall} = M_{optical} \times M_{electronic} \tag{2.8}$$

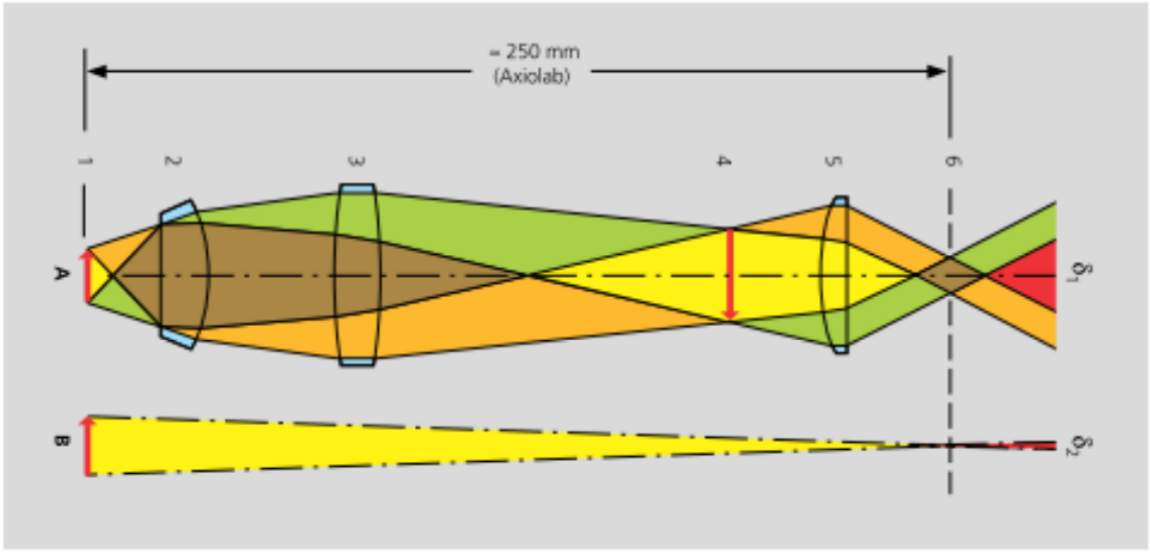

Figure 2.5: An objective-tube-eyepiece compound

The optical magnification in case of just one objective and an adapter is given by:

$$M_{overall} = M_{objective} \times M_{adaptor} \tag{2.9}$$

The electronic magnification is the ratio of the active sensor diagonal and the useful monitor diagonal:

$$M_{electronic} = diagonal_{monitor}/diagonal_{sensor} \tag{2.10}$$

2.3.6 Limits of magnification - Useful magnification

As it was mentioned above, greater magnification can be achieved using two or more lenses. So, the question is if there are any boundaries to magnifying an object infinitely. The short answer is no. Despite the fact that with an infinite number of lenses an infinite magnification is achieved, after a point that huge magnification is useless because "deeper" details of the magnified object cannot be resolved further. So the maximum useful magnification for a conventional optical microscope it is known to be 2000x. In terms of the tinyest possible distinguishable area of an object, the conventional optical microscope can produce a virtual image of a 200 nm diameter spot of the object. This is approximately the width of an average-sized bacterium. The smaller this distinguishable area is, the bigger the resolution of the microscope is. However, in practice this resolution of 200 nm cannot be approached due to lenses imperfections. Further improvements have been accomplished by the nobel prize-awarded Super Resolution Microscopy which circumvents the aforementioned limit and brings it to the nanodimension. The explanation to the existence of a limit to the resolving power of the microscope, lies in the concept of diffraction which is eventually the reason why more and more magnification power of lenses lead merely to a magnification of the smallest distinguishable area, without unveiling further details.

2.4 Diffraction-limited resolution

2.4.1 Diffraction

Lens-systems have an opening which allows a cone of light to pass through. Here lies the resolution limitation of the microscope (and of every optical device incorporating apertures). As it was mentioned in the early introduction of this section, light bends around the corners of an obstacle or a slit (aperture) into the region of geometrical shadow of the obstacle when the size of the latter is comparable with the wavelength of the incoming light. From this, also it follows that light bends around the sharp edges of an obstacle or an aperture.

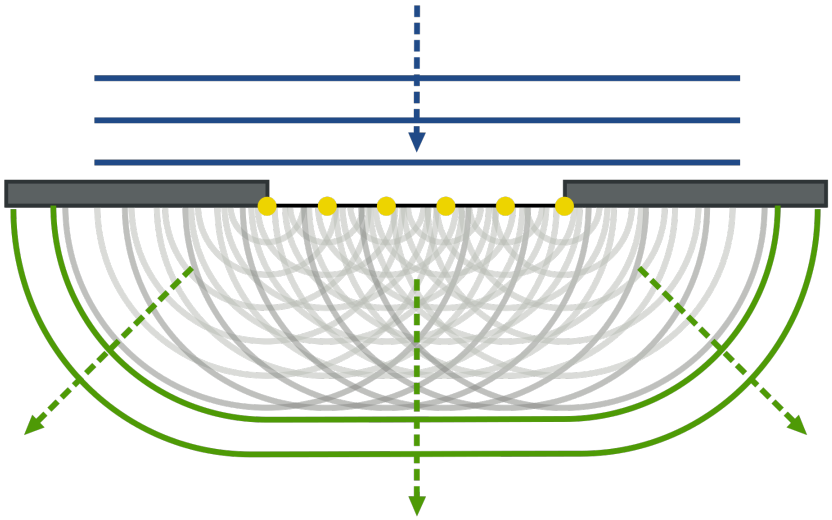

Figure 2.6: Diffraction by Huygens-Fresnel principle
Source: `https://en.wikipedia.org/wiki/Huygens%E2%80%93Fresnel_principle`

The significance of the phenomenon of diffraction in the case of image capturing lies in the fact that light does not travel linearly from the aperture towards the sensor (camera or human eye), but instead spreads to a cone angle. As it was mentioned earlier, light diffraction behaves in the same way a mechanical wave behaves entering a slit. The spreading of the post-aperture light can be explained by the Huygens-Fresnel principle. It argues that every single point of a wave front (wavelet) acts like a source of new spherical waves. These emanating waves interfere constructively or destructively with themselves creating a characteristic pattern in the post-aperture area. In Fig. 2.6, this principle is visualized with the use of 6 wavelets at the level of the aperture. While these waves propagate the total aggregating wave front takes the form of the green lines, giving the effect of the spreading of light.

When the spreading light eventually "hits" the sensor, a two-dimensional diffraction pattern appears on it. This is the resolved image of the point light source. So, as long as the light bends after it passes through the slit, the resolved image is larger. This means that

the final captured image is a degraded form of the true point source. Fig. 2.7 exhibits a case where light arrives at the aperture in plane wave fronts. That is accomplished when the light source, the aperture and the sensor are far apart in order for the spherical source waves to expand in such a degree that their wave fronts become plane or close to plane. Another occasion is when curved wave fronts enter the objective lens of the microscope and come out as plane ones. This is the Fraunhofer diffraction. In case where the incoming wave fronts are curved and sensor is relatively close to the aperture, Fresnel diffraction applies. Fraunhofer diffraction helps the understanding of the parameters that affect the level of light bending and the diffraction patterns on the sensor, because of its simplicity compared to Fresnel diffraction. The figure shows the sensor plane and the intensity of light in each point on it.

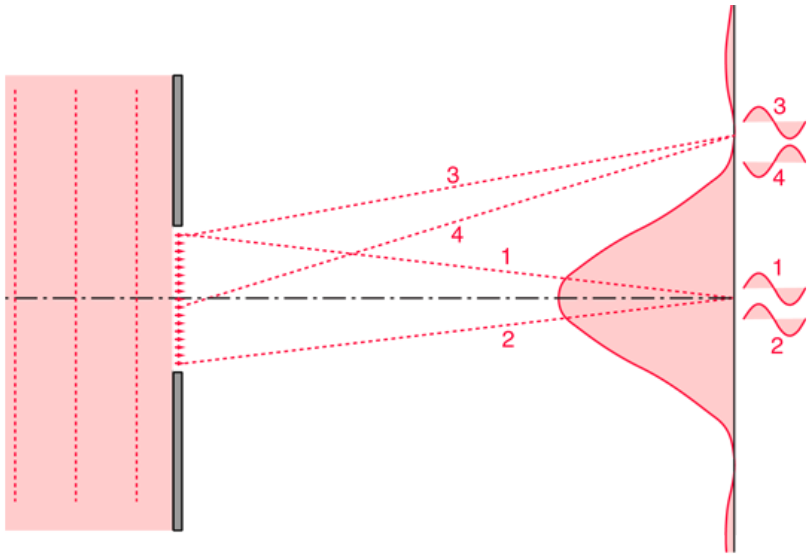

Figure 2.7: Fraunhofer diffraction
Source: `http://hyperphysics.phy-astr.gsu.edu/hbase/phyopt/sinslitd.html#c1`

A wave of light interferes constructively with another of the same wavelength λ when their path lengths differ by m multiples of λ . They interfere destructively when their path lengths differ by $(m + \frac{1}{2})\,\lambda$. In Fig. 2.7 rays 3 and 4 arrive 180 degrees out of phase on the sensor and lead to a minimum light intensity in that point. Rays 1 and 2 arrive in phase and lead to maximum light intensity.

In order to calculate how much the light diffracts, after it passes the aperture, it is sufficient to calculate the angle of the first intensity minimum over the optical axis (aperture middle). From Fig. 2.8, using trigonometric small-angle approximations (because Fraunhofer approach considers that aperture to slit length $L \gg w$ and thus $(\theta' \approx \theta)$ and applying the destructive interference condition $\frac{w}{2}\sin\theta = \frac{\lambda}{2}$, it can be shown that the angle of first intensity minimum (first trough or dark fringe) is:

$$\sin\theta = 1.22\frac{\lambda}{w} \tag{2.11}$$

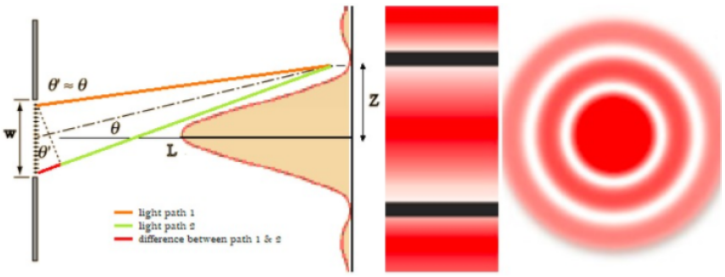

Figure 2.8: Angle of first intensity minimum (left) - Diffraction pattern formed on the sensor across the vertical line the diffraction curve extends (1D) (middle) - Diffraction pattern formed across the whole sensor plane (2D - Airy disk) (right)
Source: [28]

The above equation makes clear that the longer the wavelength of the incoming light, the larger the level of light bending after the aperture. Additionally, the bigger the aperture, the smaller the degree to which the light diffracts. Hence, in order to have a better resolved image of the true point source regardless its wavelength, the bigger the aperture is, the better this can be achieved. Bigger aperture means longer lens so as the latter gathers all the light that passes through the aperture. To express how large cone of light a lens can gather, a quantity is introduced:

2.5 Numerical aperture and resolution

Numerical Aperture of a lens (Numerical Aperture (NA)) : characterizes the range of angles over which the lens can accept (or emmit) light. It is a function of the refractive index n of the medium in which the lens is working (i.e air, water, oil) and half the angle (θ) of the largest pencil of light that the lens can accept (or emmit). [12]

$$NA = n \sin \theta \tag{2.12}$$

From this definition along with the aforementioned simple aperture characteristics, it can be concluded that the bigger the numerical aperture, the smaller the diffraction spreading and thus the better the resolution of a point source. But in order to quantify the resolution of the lens-aperture system, the smallest distance between two diffraction patterns, caused by two point sources, must be found so that they both can be resolved (seen separately). This distance is called the Rayleigh resolution limit and is defined as the distance between the crests of the two diffraction patterns, when the crest of the main lobe of the first one meets the first trough of the second one. It is equivalent to the distance between the crest of the main lobe and the first dark fringe. This lateral resolution is a function of wavelength and numerical aperture.

Because of refraction and reflection phenomena that appear when light passes from the coverslip of the specimen to the objective through a gap of air, it is preferable that an

immersion oil (high refractive index medium) is used. This allows light to travel straight towards the objective, leading thus to a larger effective NA. So, the refractive index of the immersion oil, also, plays a role in the final formation of the diffraction pattern.

$$r_{lateral} = \frac{1.22\lambda}{2n\sin\theta} = \frac{0.61\lambda}{NA} \tag{2.13}$$

, where r: lateral resolution of the lens-aperture system
λ: wavelength of light
n: refractive index of the medium surrounding the point sources
θ: half-angle of the cone of light that enters the lens NA: effective numerical aperture of the lens-aperture system

A condenser lens is often used so as to focus the illuminating cone of light onto the sample. This has to be computed too. The lateral resolution is now given by:

$$r_{lateral} = \frac{1.22\lambda}{NA_{obj} + NA_{cond}} \tag{2.14}$$

In a properly configured microscope, the condenser must have equal NA with the objective. So, this leads to the first resolution equation (Eq. 2.13)

2.5.1 Digital Resolution

When it comes to capturing an image and translate it to a digital one, the question of how the resolution is related to the image pixels arises. The image 2D signal in order to be aliasing-free and properly represent the analog true signal needs to be sampled accordingly to the $Nyquist\,theorem$. The latter states that a signal in general needs to be sample in a rate $f_s > 2f_{max}$, with f_{max} the highest frequency that is wished to be recorded. In an image, frequency has the meaning of periodic changes of luminance of the depicted objects. Thus the corresponding "period" has to do with distance between this changes. The Nyquist sampling rate can be modified to: $D_s < D_{min}/2$, where D corresponds to distance (or size). This gives the imaging sample rate (pixel size) which should be 1/2 the size of the smallest object (resolution) that is wished to be recorded. In practice, an image pixel usually represents distance that is 2.3 - 3 times smaller than the optical resolution. [27]

Let it be that the sampling process is completed. In order to find the physical distance that is represented by a pixel without knowing the sampling rate, the sensor pixel size and the magnification of the optical system must be known:

$$physical\ distance = \frac{sensor\ pixel\ size}{overall\ magnification} \tag{2.15}$$

2.6 Anatomy of an optical microscope

As it was mentioned, this study concentrates on brightfield, fluorescence and confocal microscopy. Brightfield microscopy is achieved using and configuring appropriately an optical

microscope. Fig. 2.9 shows the optical train inside a modern optical microscope. Light emanated from a source travels through a system of diaphragms (apertures), plates and lenses in order to be configured in a way that it evenly disperses across the plane of the field of view of the focused specimen. The final stage of this source light-configuring system is the condenser, which focuses the cone of light onto the specimen plane. Then, the re-emmitted light from the sample travels through the objective-eyepiece or/and the objective-camera sensor system. Focus knobs are used, as the name implies, to adjust the microscope tube or the specimen stage for proper focusing. The coarse focus knob adjusts in the centimeter range, whereas the fine focus knob adjusts in the micrometer range. There are also knobs for the adjustment of the desired field of view of the sample.

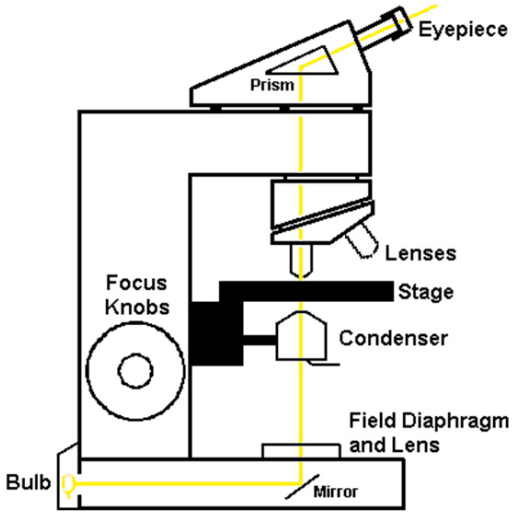

Figure 2.9: Basic parts of a typical optical microscope
Source: `http://www.doctorc.net/Labs/Lab2/lab2.htm`

When specimens, living or non-living, organic or inorganic, absorb and subsequently re-radiate light, the process is described as photoluminescence. If the emission of light persists for up to a few seconds after the excitation energy (light) is discontinued, the phenomenon is known as phosphorescence. Fluorescence, on the other hand, describes light emission that continues only during the absorption of the excitation light. The time interval between absorption of excitation light and emission of re-radiated light in fluorescence is of extraordinarily short duration, usually less than a millionth of a second.

2.7 Fluorescence microscope

For each fluorescent substance, there is a certain range of wavelengths that cause its stimulation. After the absorption of the excitation light, the substance emits light of longer wavelength which is finally captured. In order to illuminate the specimen with the wavelength band which excites it, an excitation filter is placed right after the light source. Similarly,

in order to observe the re-emitted fluorescent light, an emission filter is placed right before the eyepiece or the camera sensor. These filters are termed barriers, since they block by absorption the unwanted light. Due to the epi-illumination fluorescence microscope design, there must be a specialized filter that will reflect the excitation light towards the specimen and will allow re-emitted light to pass through it. Such a filter is named a dichroic mirror or else a dichromatic beamsplitter. Reflection occurs via destructive and illuminance-reducing interference with alternating layers of high and low refractive indeces, whereas transmission happens via constructive and reinforced interference with the layers. For this reason, such filters belong to the family of interference filters. Specifically, successive layers of dielectric materials, with thickness values ranging between one-quarter and one-half of the target wavelength consist the main body of these filters. In many of the current epi-illumination fluorescence microscopes, the excitation, emmision filters along with the dichroic mirror are altogether incorporated into a single fluorescence filter cube. The whole design of the microscope is epigramatically shown in Fig. 2.10 and is termed widefield epi-illumination fluorescence microscope. [9]

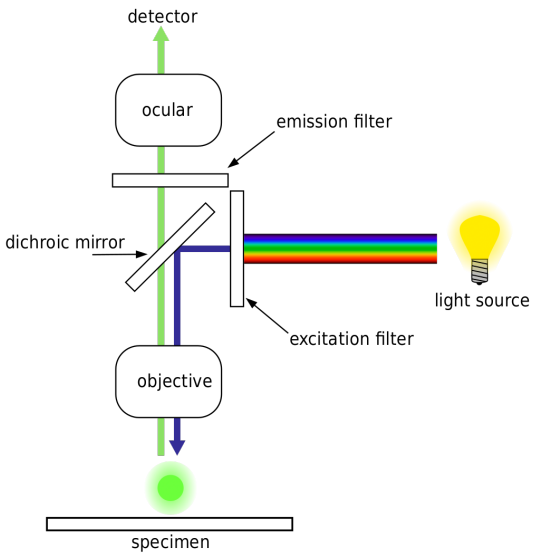

Figure 2.10: Widefield epi-illumination fluorescence microscope schematic
Source: `https://en.wikipedia.org/wiki/Fluorescence_microscope`

2.7.1 Fluorescence

[18] Fluorescence may be exhibited naturally by some materials or biological structures (autofluorescence/primary fluorescence) as well as exhibited by artificially added fluorescent markers (secondary fluorescence). Fluorescent molecules are also called fluorescent probes, fluorochromes or simply dyes. When they are conjucated to a larger macromolecule, through absorption or covalent bonds, they are termed fluorophores. Thanks to this attachment, the distribution of the corresponding macromolecule of a fluorophore can be observed.

Due to heat transfer within fluorophores or interactions between fluorophores and other molecules, the re-radiated light has less energy than the absorbed light. So, the emitted light has a longer wavelength than that of the excitation light. This difference between the maxima of the excitation-emission bands is termed as Stokes shift. Typically, the emission band is a mirror of the excitation one. In general, fluorescence investigations are conducted in the range of ultraviolet to visible spectrum (250 - 270 nm).

The distribution of electrons and the overall molecular geometry can be determined by electronic states. Several different electronic states exist, depending on the total electron energy and the symmetry of various electron spin states (paired or unpaired spins - opposite or same spins in an orbital). The number of unpaired electron spins in an electronic state defines the state name in the numeration form of singlet, doublet, triplet etc. The ground state of most organic molecules is an electronic singlet, that is no electron spins are unpaired. The excitation process has no effect in changing the spin-pairing, hence the excited states are singlets too. Each electronic state is further subdivided into vibrational and rotational states associated with the atomic nuclei and the bonding orbitals. In fluorescence, various transitions are taking place through different paths among energy levels. Transitions involved in absorption and emission of light by a fluorochrome can be shown in a Jablonski energy diagram (Fig. 2.11).

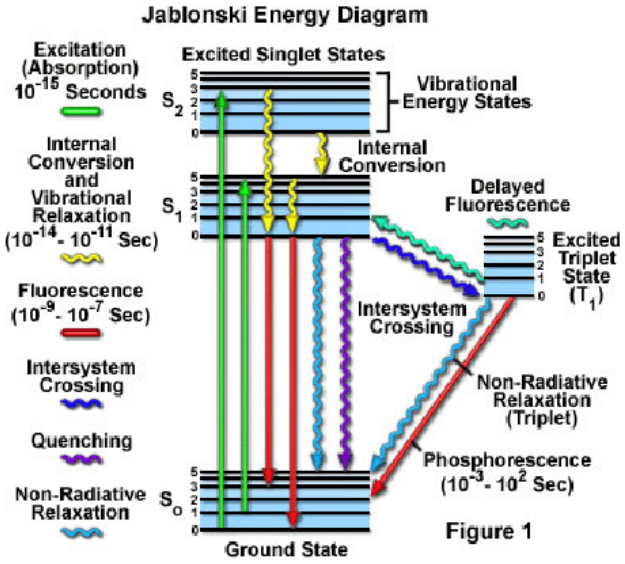

Figure 2.11: Jablonski energy diagram showing transitions involved in absorption and emission of light by a fluorochrome. Straight lines show absorption or emission of a photon, whereas wavy lines show non-radiative processes
Source: `https://www.olympus-lifescience.com/en/microscope-resource/primer/lightandcolor/fluoroexcitation/`

Absorption leads the molecule to an excited singlet state depending on the energy of the incident photon which has to be at least equal to the corresponding energy of an excited

state. This takes place "instantly", in approximatelly a femtosecond. Afterwards, several processes will occur with varying probabilities. The most likely will be non-radiative relaxation to the lowest vibrational energy level of the first excited state. This is the vibrational relaxation which can happen directly or through an internal conversion process. From this point forward, many paths can be taken. One is the desired fluorescence emission which is usually accompanied by transitions to higher vibrational energy levels of the ground state. Other roads are energy dissipation nonradiatively as heat or energy transfer due to molecules collision (i.e quenching) or transition to an intermediate triplet excited state at its lowest vibrational state. The latter transition is known as intersystem crossing, again with no radiation. From that point, excitement back to the higher-energy singlet state might occur, resulting in a delayed fluorescence after a radiative relaxation. The other possibility is relaxation to the ground state, even though transition from an excited triplet state to the ground singlet state is forbidden. It might happen again in the form of heat, but also with the emission of a photon, which is termed phosphorescence. Because of this forbidding law, phosphorescence is very rare, with a probability of several orders of magnitude lower than that of fluorescence.

Considering the aforementioned different transition paths, it is clear why fluorescent light is of longer wavelength than that of the absorption light, justifying the Stokes shift. Bearing energy of light is inversely proportional to the wavelength of it. Specifically, radiative relaxations are of high probability when they start from the lowest vibrational state of the first excited state and when they culminate in the highest vibrational state of the ground state. Hence, the emission energy leap is much smaller than the absorption energy leap. Contributing factors to this phenomenon are heat conversions, resonance energy transfer (RET) and quenching processes. In RET, energy is transfered with non-radiative long range dipole-dipole interactions between fluorophores. In quenching, energy might be transfered through collisions between fluorophores and other molecules (usually oxygen, halogens and amines) that are translated as coupling of electronic orbitals between the interacting molecules. Also, formation of non-fluorescent complexes can reduce the population of active excitable molecules, thus limiting the absorption of incident light.

Another unwanted pheonomenon, regarding energy and intensity loss, is photobleaching. Fluorochromes can lose the ability of fluorescence permanently due to long exposition to high intensity light which cause chemical destruction to them.

In general, the decay of fluorescence intensity as a function of time in a uniform population of molecules excited with a brief pulse of light is described by an exponential function:

$$I(t) = I(0)\, e^{-t/\tau} \tag{2.16}$$

, where $I(0)$: initial fluorescence intensity
τ: time in which fluorescence intensity falls in $1/e \approx 37\%$ of $I(0)$
The exact decaying degree depends on the particular fluorochrome. In addition to this, other parameters are also used to describe and compare different fluorochromes:

- Extinction coefficient: Ability of light to absorb light. Those chromophores that have a high extinction coefficient also have a high probability of fluorescence emission, in the expense though of their intrinsic lifetime (below).
- Quantum yield: Gauge of the efficiency of fluorescence emission. It describes the probability that an excited molecule will end up in emitting a photon, either through a direct or a delayed fluorescence process.
- Fluorescence lifetime: The characteristic time that a molecule remains in an excited state prior to returning to the ground state.

2.8 Point Spread Function

Fig. 2.8 shows the formation of a diffraction pattern on the sensor plane. Because this pattern is the spreaded light initially emanated from a point source, it is given the name Point Spread Function (PSFs). The term "function" is valid because the spreading, as it was said, depends on the NA of the lens-aperture system, the refractive index of the immersion oil (if it exists) and the λ of the source light.

By simulating the single-slit phenomenon in a computer, the PSF can be visualized. Using 2,3 and 9 in-phase wavelets of the Huygens-Fresnel model (Fig. 2.12), it can be shown how a PSF is formed across the aperture-sensor plane space. As long as there is no finite number of wavelets, also a simulation of "infinite" ones is shown in Fig. 2.13

The resolution on the image plane (lateral resolution) is given by Eq. 2.13 . The tiniest discernible distance in the optical axis (depth axis) is larger that the lateral one. It can be computed by:

$$r_{axial} = \frac{2\,\lambda\,n}{(NA)^2} \tag{2.17}$$

This leads to the same conclusion as for the lateral resolution. That is, the shorter the λ or/and the larger the NA, the better the axial resolution. The PSF can either be calculated theoretically by various models or be measured experimentally.

2.8.1 Theoretical PSF

Taking into account how the wave fronts of light interfere with a propagation medium, a mathematical expression can be built gradually [19]. This expression will be in terms of wave amplitude and phase as a function of the 2D coordinates of the propagating wave of light at a specific, perpendicular to the optical axis, plane z (depth plane). The emission of waves from a point source can be seen as an input impulse:

$$u_0(x, y) - A_0\delta(x, y) \tag{2.18}$$

, where A_0 : initial wave amplitude of the emmitting source of light

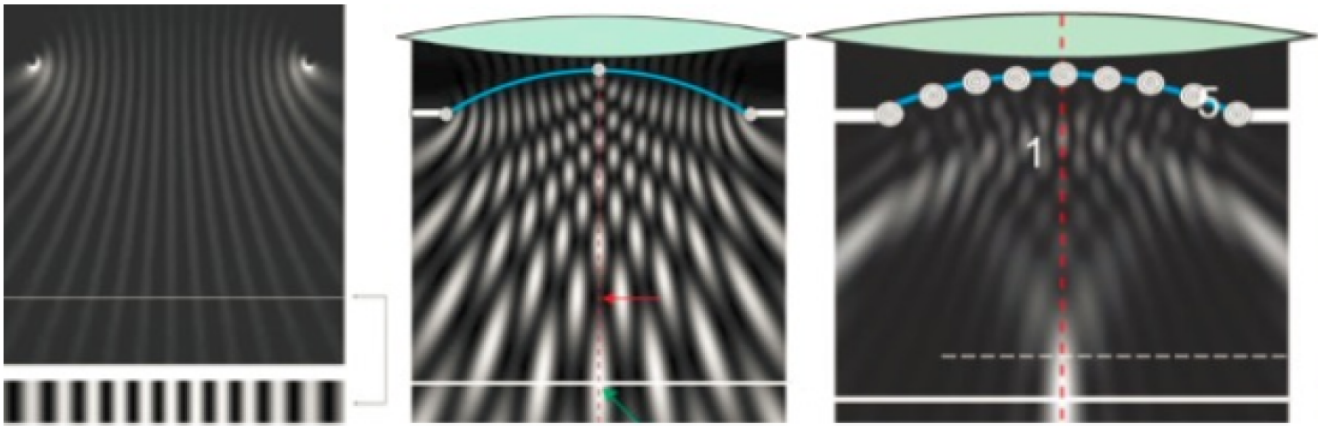

Figure 2.12: PSF formed by 2,3 and 9 wavelets of the Huygens-Fresnel mode
Source: Youtube: "iBioEducation" channel - "iBiology Microscopy Course" - "Microscopy: Point Spread Function (Jeff Lichtman)" - video snapshots

At first, light travels in free space meaning no lenses or apertures are included. The free-space system has an impulse response, let it be $h(x, y; z)$. Thus, the output wave amplitude of this system at the depth plane z_0 just before the lens, will be:

$$u(x, y; z_0) - h(x, y; z_0) * A_0\delta(x, y) = A_0 h(x, y; z_0) \tag{2.19}$$

, where $*$ is the convolution operation sign

The affected transmission of light through the lens-aperture system of focal length f can be described with a pupil function which captures every optical aberration in the amplitude and phase that takes place between the object focus plane and the image plane. These aberrations [24] (deviations from the ideal optical path) happen due to irregularities or misalignments in any component of the imaging system light path, especially the objective lens but also other lenses, mirrors, filters or apertures. Such aberrations are present in various forms. Speaking about rays of the same wavelength: Astigmatism, where rays that propagate in two perpendicular planes, have different focal spots. Coma, where slanted parallel rays entering a lens, eventually focus on different spots on the image 3D space. Defocus, where rays do not focus on the a priori designed focal spot. Chromatic aberration, where rays of different wavelengths have different focal spots. Spherical aberrations, where rays from different points across the lens, focus on different spots of the optical axis. Distortion, where a rectilinear object eventually appears curved. These aberrations can be integrated to a scale-causing factor as for the wave amplitude. Thus an ideal lens-aperture system will have a scaling factor of 1 for every point of the pupil plane. Possible deviations will cause the scaling factor to diminish. Consequently, a pupil function integrates amplitude and phase factors, thus making it a complex function:

$$P(x, y) = p(x, y)e^{j\Phi(x,y;f)} \tag{2.20}$$

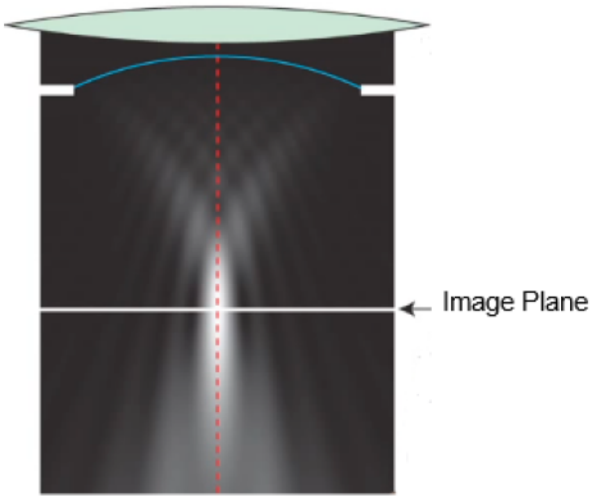

Figure 2.13: PSF formed by "infinite" wavelets of the Huygens-Fresnel model. The hourglass-like shape of the PSF in the center defines the detail in which the point source is resolved. The red dotted line is the optical axis along which the light travels
Source: Youtube: "iBioEducation" channel - "iBiology Microscopy Course" - "Microscopy: Point Spread Function (Jeff Lichtman)" - video snapshots

So, the wave fronts equation when light enters the free-space just after the exit of the lens becomes:

$$u'(x, y; z_0) = A_0 h(x, y; z_0) p(x, y) e^{j\Phi(x,y;f)} \tag{2.21}$$

Note: no convolution operation here, as the pupil function plays a scaling role.

Finally, when light reaches the image plane, the free-space impulse response function at the image plane z_1 convolves with the so far computed wave front equation. This leads to the wave function at the image plane which is the 2D PSF (on focus):

$$PSF(x, y) = u'(x, y; z_0) * h(x, y; z_1) = \left(A_0\, h(x, y; z_0)\, p(x, y)\, e^{j\Phi(x,y;f)} \right) * h(x, y; z_1) \tag{2.22}$$

The above process can be also done in order to compute the wave function in different planes from the image focus plane. Hence, a 3D PSF is formed. In reality, though, a single 3D model is not sufficient to completely describe image formation throughout the 3D object space. This is because PSF is often a function of the location of the point source in the object space. Thus, in reality every point of the object corresponds to a different PSF. A system, the Point Spread Functions of which behave in this way, is called a shift-variant system.

Different approximations can be made, depending on the nature of diffraction, the possible consideration of shift-variance and the amount and degree of effect of possible aberrations,

if the latter are taken into account.

Assuming there are no aberrations and that the Fraunhofer approach is valid, a more specific PSF can be built. A pupil function for a circular aperture of radius α through which light is transmitted unaffected has the value 1 inside the area encompassed by the aperture in the axes system x', y'. The polar coordinate translation is:

$$r = \sqrt{x^2 + y^2} \quad \text{and} \quad \theta = \arctan(y'/x') \tag{2.23}$$

At the image plane the axis system (x,y) is translated in polar coordinates as:

$$\rho = \sqrt{x^2 + y^2} \quad \text{and} \quad \psi = \arctan(y/x) \tag{2.24}$$

According to Principles of Optics by Born and Wolf, as stated in [21], the diffraction pattern wave function (amplitude) is the Fourier Transform of the pupil function.
From this it follows that:

$$D(x, y) = \int_0^{\alpha} \int_0^{2\pi} e^{-ikr\rho\cos(\theta-\psi)}\, r d\,\theta dr \tag{2.25}$$

, where $k = 2\pi/\lambda$ (wavenumber)

Using the Bessel function of the first kind and order 0, the above equation can be modified as:

$$D(\rho) = 2\pi C \int_0^{\alpha} J_0(kr\rho) r dr \tag{2.26}$$

, where C: constant

PSF is in terms of intensity of light which is proportional to the squared amplitude of the wave function. So, from the above equation arises that:

$$PSF(\rho) = \left| 2\pi C \int_0^{\alpha} J_0(kr\rho) r dr \right|^2 \tag{2.27}$$

For an aberration-free and shift-invariant in all directions PSF, the 3D Born and Wolf approximation can be useful [13]. The constraint is though, that the observed fluorophore particle is located at the focal plane of the objective lens but right beneath the coverslip. The model is expressed in the Kirchhoff's diffraction integral formula as:

$$PSF(x, y, z) = \left| \int_0^1 J_0 \left[k \frac{NA}{n_i} \sqrt{x^2 + y^2}\, \rho \right] e^{-\frac{1}{2} jk\rho^2 z \left(\frac{NA^2}{n_i} \right)} \rho d\rho \right|^2 \tag{2.28}$$

, where PSF: scalar
J_0: Bessel function of the first kind of order 0 (Bessel function appear in problems of wave propagation)
k: wavenumber of the emitted light in vacuum ($k = 2\pi/\lambda$),
n_i: refractive index of the immersion oil

The Gibson and Lanni PSF model takes into consideration the consequences of the optical path modifications that occur when light rays follow trajectories other than that for which the optics were designed. It integrates the optical path difference (ODP),which is the difference between ideal trajectories and real trajectories, taking into account parameters determining path fluctuation: thickness (t_{oil}) and refractive index (n_{oil}) of the immersion oil, thickness (t_g) and refractive index (n_g) of the coverslip and the thickness (t_s) and refractive index (n_s) of the sample.

Any deviation of any of these parameters from the optimal values for which the optics were designed will cause spherical aberrations. The resulted prolonged focus spot has the effect of an assymetry in the 3D PSF on the depth axis. In the case of microscopy, this is a common phenomenon which increases as the object focal plane moves deeper into the sample, thus inducing more refractive index mismatches inside the sample as well as between the sample, the coverslip and the immersion medium. Spherical aberration is the reason why PSF is shift-variant on the depth axis.

As for the Gibson and Lanni model, it incorporates shift-variance only in the depth axis. It can be seen as a generalization of Born and Wolf in the sense that the fluorophore particle can be located at any depth within the sample. It also considers three optical layers (sample-coverslip-immersion) instead of two (glass-immersion). The model description again in the Kirchhoff's diffraction integral formula is:

$$PSF(x,y,z) = \left| \frac{C}{z_d} \int_0^1 J_0 \left[k\alpha\rho \frac{\sqrt{x^2+y^2}}{z} \right] e^{jW(\rho)} \rho d\rho \right|^2 \tag{2.29}$$

, where PSF: scalar,
C: a normalizing constant,
z_d: tube lens-detector distance,
$W(\rho)$: phase aberration induced:

$$W(\rho) = k\Bigg\{ n_s t_s \sqrt{1 - \left(\frac{NA\rho}{n_s}\right)^2} + n_g t_g \sqrt{1 - \left(\frac{NA\rho}{n_g}\right)^2} + n_{oil} t_{oil} \sqrt{1 - \left(\frac{NA\rho}{n_{oil}}\right)^2} - n_g^* t_g^* \sqrt{1 - \left(\frac{NA\rho}{n_g^*}\right)^2} - n_i^* t_i^* \sqrt{1 - \left(\frac{NA\rho}{n_i^*}\right)^2} \Bigg\}$$

2.8.2 Experimental PSF

Prediction of all the various phenomena that take place in the optical train is proved to be a complex problem. Thus, the existing theoretical PSF models do not integrate every optical path deviation from the ideal path. The problem of diffraction pattern formation was examined using the concept of point sources of light. In fact, this is abstract, since there cannot be an infinitelly small object. However, from the concept of optical system resolution, it follows that a sub-resolution object can be considered as an infinitelly small object. Hence, depicting such an object, a real PSF can be built, which incorporates all optical train defects.

For that reason, several methods have been proposed, such as using quantum dots and fluorescent microbeads. Quantum dots are semiconductor particles with size of some nanometres that emit light of specific frequencies if electricity or light is applied to them. The disadvantage, though, is that good preparations of these are hard to obtain as they easily form aggregates, thus not being "single points" anymore.

Fluorescent microbeads are of various materials. [20] Even though in theory, they must be as small as they can be, this is impractical because these beads exhibit low Signal to Noise Ratio (Signal to Noise Ratio (SNR)) and meagre signal. Thus, they are usually chosen to have size more than half the resolution of the optical system, such as 150 nm. A sufficient fluorescent signal by beads is possible either when they aggregate or when they receive a bigger quantity of excitation light. Big aggregation hinders the determination of a single bead because of the overlap by each single bead diffraction pattern. As for more intense excitation light, this has the danger of causing untimely photobleaching to the beads, thus diminishing their life span. Since the level of the light signal intensity is meagre, photon noise of the bead image capture is very pronounced which means a very low SNR.

2.8.3 Modulation Transfer Function

Physical meaning and PSF-MTF-OTF relation

As examined in Seq. 2.4.1 - numerical aperture and resolution, the distance between the diffraction pattern crests of the images of two point sources of light, defines the resolution of the optical system. So, expanding this concept to more point sources aligned in a

straight line, it is safe to say that the closer to each other they are, the more the corresponding diffraction patterns are overlapped, deteriorating thus the depicted contrast among the point sources. Further expanding to parallel lines of point sources (line sources) in a way that they form bright and dark stripes upon a plane parallel to the image sensor plane (square wave), the same conclusion can be made. The depicted line sources will exhibit an overlap of their diffraction patterns, thus diminishing the contrast among them. Consequently, the imaging lens, camera sensor, and illumination play key roles in determining the resulting image contrast. The lens contrast is typically defined in terms of the percentage of the object contrast that is reproduced. The sensor's ability to reproduce contrast is usually specified in terms of decibels (dB) in analog cameras and bits in digital cameras.

The term modulation of MTF is exactly the above-mentioned contrast. How well the optical system can transfer this contrast / modulation from the object to the image, is the second term. As for the term function, it is so because modulation transfer depends on the particular distance among the aforementioned line sources (to keep the last example) or otherwise the spatial frequency of these line pairs. A line pair is a bright (white) and a dark (black) stripe altogether, mathematically forming a pulse of light. The unit of spatial frequency is line pairs per milimeter or cycles per milimeter (lp/mm or cycles/mm).

To express the contrast percentage of an image of bright and dark stripes, the maximum and minimum intensity values must be used. A full-bright stripe is 1- valued, whereas a full-dark stripe is 0-valued. The contrast expression is given by: [2]

$$\%\, Modulation = \frac{I_{max} - I_{min}}{I_{max} + I_{min}} \times 100 \tag{2.30}$$

Assuming no resolution loss by the optical system, it is clear that the modulation transfered is 100%. That is the optical system reproduces the contrast of the object in its whole 100%.

At a particular spatial frequency, the transfered contrast of an object depends on its off-(optical)axis distance. Specifically, the MTF decreases as the object is farther from the optical axis. Also, as the line pairs per milimiter get more and more, there is a limit where the optical system cannot anymore resolve them. At this point the modulation becomes 0%. The corresponding spatial frequency is the cut-off frequency.

A said above, changes in depicted contrast of an object pattern are described by MTF. Yet, optical system aberrations also cause changes in PSF intensities which in turn result in a linear lateral shift of the object pattern. This pattern-phase shift is desbrived by a function called Phase Transfer Function (PTF). Altogether, these contrast changes and phase shifts are incorporated in a complex function called Optical Transfer Function (OTF): [3]

$$OTF = |OTF|e^{iPTF} = MTFe^{iPTF} \tag{2.31}$$

OTF can also be defined in terms of PSF, as :

$$OTF(v) = \int PSF(x)e^{-i2\pi vx} \tag{2.32}$$

where x is the spatial coordinate in the image plane.

This equation implies that OTF is the Fourier transform of PSF. Intuitively, this can be comprehensible and be deduced from the below thinking using only the MTF (no lateral phase shifts of the image pattern): The point source acts like an input impulse to the system, resulting to an impulse response which is the PSF. It is known that, mathematically, in order to build an impulse, "all" frequences are needed. So, the Fourier Transform of an impulse is a plane wave, integrating infinite frequences. Ideally, if the PSF was identical to the point source, that plane wave would be the Fourier Transform. But since the PSF is different incorporating a resolution limit, instead of a plane wave, only a range of spatial frequencies will contribute to the formation of the PSF. Yet, these contributing frequencies form the MTF. The upper boundary of this spectrum depends on the above-mentioned resolution limit. As for an ideal aberration-free PSF, the cut-off frequency of its MTF is: $1/2\lambda f$.

2.9 Experimental Measurement of MTF - Slanted Edge Method

Generally, there are 3 ways of measuring a MTF. Either by using a square wave as examined in 2.8.3 or by a sine wave (smoother changes between dark and bright areas) or by the slanted edge method. What is examined below is related to the slanted edge method.

From the aforementioned relation between inpulse response and infinite frequencies,it is safe to say that in order to measure what band of spatial frequencies are resolvable by an optical system, its output with an impulse as input must be found. Specifically, the impulse is a 2D signal, allowing thus the imaging measurement of this line profile which it turn gives the line spread function. In practice, the theoretical impulse is not directly feasible as it requires zero width and infinite intensity. So, eventually the measurent of the MTF is done indirectly with experimental processes termed edge-gradient methods. [14]

Firstly, an edge profile is measured. An edge profile is ideally a step function. In the case of images, it is a dark 2D area followed by a bright one, forming thus a "step of light". The reproduced edge is translated through the optical system in a degraded degree. Specifically, there is no immediate change in light intensity from dark to bright, rather a smoother ESF. So, the acquired image of the edge can be called an ESF. The terms edge profile and ESF are used alternately. Then the computation of the discrete first derivative of the ESF will give the PSF. Finally, the modulus of the Fourier Transform of the PSF will grant the wanted MTF.

The above method can be executed with more than one ways. An edge profile can be taken from picturing a very precisely designed edge for this purpose, thus with no deforma-

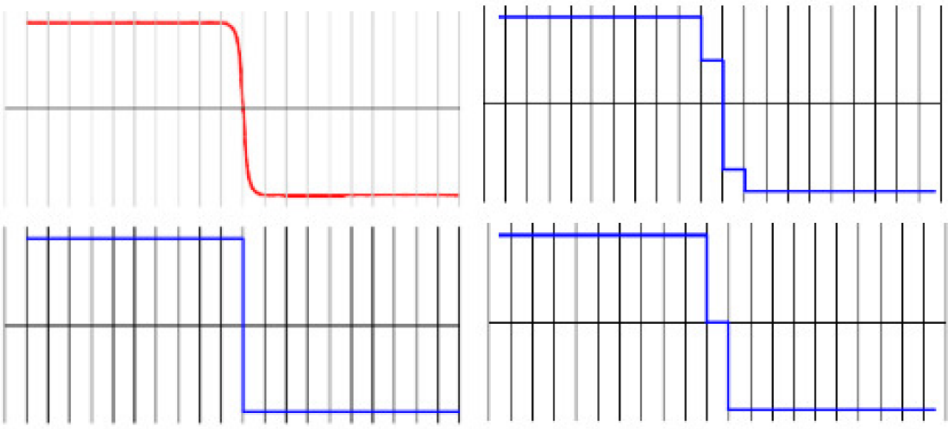

Figure 2.14: The true analog ESF (along 1 spatial direction for simplification) (top left) will be digitized but with a quantization error which depends on the number of pixels in the horizontal axis of the sensor and the single pixel size. Top right, bottom left and bottom right show 2, 0 and 1 samples respectively which define the edge.
Source: `http://dougkerr.net/Pumpkin/articles/MTF_Slant_Edge.pdf`

tions along the edge. As a second way, an edge feature from image data can be captured providing the wanted edge profile. However, this requires a captured edge of sufficiently high optical quality, meaning negligible noise and clear edge details.

Regarding the first approach, in order to capture the edge profile, it must be sampled. As a first thought, the edge can be sampled parallel to the pixel columns of the camera sensor. However, the theoretical resolution of a sensor array is not sufficient to discern the luminance change of the edge with sufficient resolution. There can be different digitization occasions depending on the sensor. This can be visualized in Fig. 2.14.

2.9.1 Slanted Edge Principle

[22] Fortunately, "fake" enhanced resolution of the sensor can be realized by rotating the edge profile (usually by 5 degrees), thus forming an angle between it and the pixel grid (Fig. 2.15).

Since every evenly spaced vertical line, parallel to the edge, has the same luminance, it can be observed that every center of a pixel is assumed the role of a sample of the ESF. Hence, this "trick" provides a much better sampling of the ESF. By applying trivial trigonometric equations: Spacing of ESF $samples = pixel\ pitch \times sin(\alpha)$, where α is the angle of rotation of the edge profile. So, the smaller the pixel pitch and the angle are, the better the sampling is. Because, though, the pixel detectors actually do not pick up the luminance at a point (dots in the example of Fig. 2.15), but rather respond to an average of some sort over a region (bin) approaching the domain of the pixel, certain special steps have to be taken in the evaluation of the ESF from the set of collected pixel detector values (examined below).

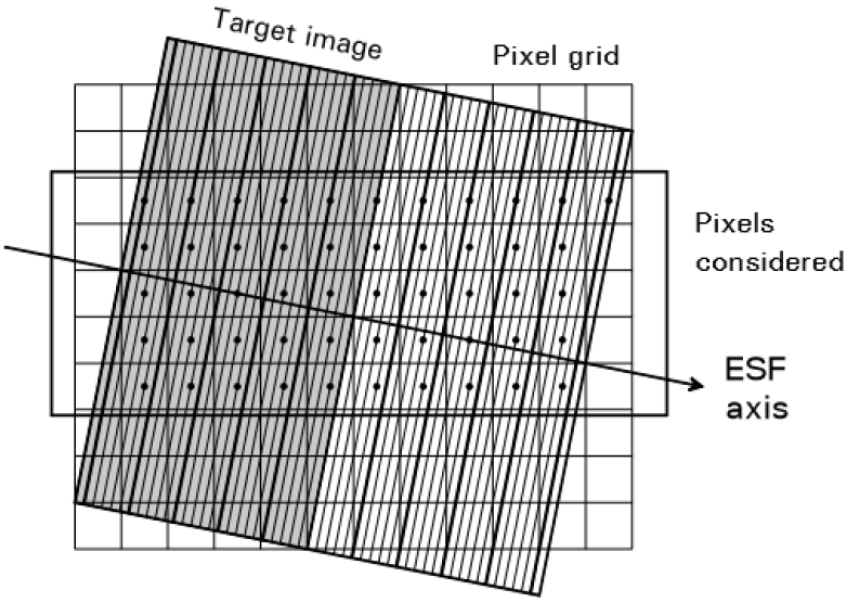

Figure 2.15: Every center a pixel is assumed the role of a sample of the ESF
Source: `http://dougkerr.net/Pumpkin/articles/MTF_Slant_Edge.pdf`

2.9.2 Standardized MTF Evaluation Method

The whole process of measuring the MTF is standardized by the ISO 12233 and implemented by little or no modifications to the latter: [14]

- ROI identification: First, the region of interest (ROI) (m lines, n pixels) surrounding the edge is selected. The luminance from each RGB photosensor of the ROI is measured (a pixel consists of 1 red 2 green and 1 blue photosensors).
- OECF transformation: The image data are transformed with an opto-electronic conversion function (OECF). This function is a relationship between input luminance and digital output levels for an opto-electronic digital image capture system.
- Luminance record computation: A luminance array is computed as a weighted sum of red, green, and blue image records at each pixel.
- Derivative of each data line: The 1D discrete derivative of each line along the horizontal axis of the sensor is taken. In that way, the edge location and direction can be estimated. Note: the derivative of each line gives the 1D PSF which with the rest PSFs form the Line Spread Function (LSF).
- Centroid computation for each line: The centroid of a straight 1D line is actually its middle point. It is a translation of the line "weight". When, though, each point of the line has an intensity integrated to it, the centroid is found in a different point along the line depending on the intensity distribution. In the case of a first derivative of a line, the centroid is located upon or near the spike of the derivative.

- Linear fit of the centroids: In order to define the slanted edge, all the locations of the centroids are fitted with a linear equation.
- Projection of the image data along the edge direction: As stated in the slanted edge principle of this subsection, each pixel or more precisely each element of the luminance arrays, plays the role of a sample for the ESF. So, with a linear fit to line, a 1D "super sampled" ESF is formed.
- Data binning with 1/4 of original sampling rate: The previous step results in a 4x oversampling. At this step, a binning process (replacing of each 4 samples with a value that represents them) is done with a $1/4x$ sampling rate.
- Derivative of ESF and windowing: This grants the LSF.
- Fourier transform of LSF: A discrete FT of the LSF (1D LSF = PSF) gives the OTF, as examined in 2.8.3
- Modulus of OTF and normalization: As the wanted MTF describes a percentage of modulation transfer, the modulus of the OTF must be normalized in range 0-1.

Chapter 3

Image formation and deblurring technologies

3.1 Sources of image degradation

Through different stages in the opto-electronic digital image capture system, many aspects of unwanted noise are introduced. The sources of degradation to the image can be classified as: [29]

- Photon shot noise: Due to the particle nature of light and the irregular distribution of photons among the pixels, some fluctuations of photon events occur. This is heavily observed when the light of the environment of the object is of low intensity. Random arrivals of photons can be modeled with Poisson distributions.
- Thermal noise: Electronics of the imaging system while in operation cause thermal agitation of electrons that were previously at equibrium. This results in faulty pixel electron charge measurements. The random activation of electrons due to heat can be modeled with Gaussian distributions.
- Scatter: Specimens with high heterogeneity of refractive indeces cause a scattering of light that because of its intrinsic complexity cannot be predicted and therefore to be modeled. Scatter increases as specimen thickness.
- Glare: Imperfections or misalignments of the components across the optical train cause a glare effect that can corrected with material and alignment improvement.
- Blur: Diffraction phenomena put a limit in image resolution. So, when an optical system magnifies an object close to its intrinsic resolution, a blurred version of the true object is observed. Also, blurring happens when light from out-of-focus parts of the sample is recorded on the focus image plane and/or light of adjacent areas mix among each other. This form of noise is independent from the above-mentioned types of degradation. Blur removal is possible with the use of deblurring techniques.

Currently used microscopy technologies are targeted in different aspects of blur removal. One target is the eradication of effects related to diffraction phenomena or more specifically

the improvement of the Airy disk so as to have a smaller radius and the surrounding diffraction pattern so as to exhibit ripples of lower intensity. This goal has been achieved by the nobel-awarded Super Resolved Fluorescence Microscopy technologies. They allow images to be taken with a higher resolution than the diffraction limit of an optical microscope, enhancing the resolution from 200 nm to 100 nm. Two different methods accomplish the super resolution goal; Stimulated Emission Depletion Microscopy (STED) and Single-Molecule Microscopy, just for mention. The other target is the removal of defocused light from the focused image and of superpositioned light of on-plane neighboring areas. For this goal there exist two solutions: Confocal Microscopy and Deconvolution Microscopy.

3.2 Deblurring technologies

3.2.1 Conofocal Fluorescence Microscopy

[25] The basic element of a fluorescence confocal microscope is a pinhole that is place before a light detector (i.e photomultiplier tube or PMT). This pinhole allows only light coming from planes very close to the focal one to pass through. The advantage arising from this is that lateral as well as axial resolution are enhanced. One disadvantage is though, that blocking a significant percentage of the incoming cone of light leads to low signal intensity. This can be solved by long exposures to fluorescent light. However, this has the danger of quicker photobleaching, thus allowing less time for fluorescence observation as well as photoxicity phenomena. The latter incorporate the toxic danger of some fluorochromes when the are attached to cells under study. Light activates some processes within the labeled cells that eventually compromise them entirely and damage their subcellular components. This danger increases as fluorochromes are repeatedly or heavily exposed to light.

3.2.2 Widefield Fluorescence Deconvolution Microscopy

[29] An alternative way to remove the out-of-focus light is to record images at a series of focal planes using a widefield microscope and then use a detailed knowledge of the imaging process to correct it by computer image processing. Apart from defocused light, superpositioned light from on-plane neighboring areas has a blurring effect across this single plane. This happens since PSFs of adjecent points on a plane mix with each other. Fortunately, altogether the defocused and the on-plane superpositioned light can be restored back to their area of origin. Restoration has the meaning of reversing the process of blurring and ultimately the effect of the PSF on the image (either on a 2D or a 3D image). The image of an object can be divided in individual areas. Through the linearity property of optical systems, the image of all the individual areas is equal to the ensemble of the images of each area seperately. This means that:

$$\begin{aligned} Image(object) =& Image(\alpha 1 + \alpha 2 + ... + \alpha n) \\ =& Image(\alpha 1) + Image(\alpha 2) + ... + Image(\alpha n) \end{aligned}$$

, where α corresponds to a particular individual point.

Since, it is known that the depiction of an individual area of a particular lumincance is spreaded by the weights of the PSF of the optical system and assuming a shift-invariant PSF, it can be deduced from the above equation that:

$$\begin{aligned} Image(object) =& \sum_{A_1} \alpha_1 \odot PSF + \sum_{A_2} \alpha_2 \odot PSF + ... + \sum_{A_n} \alpha_n \odot PSF \\ =& \alpha * PSF \end{aligned}$$

, where $\odot$: element-wise multiplication,
α: vector consisting of all the 'α' areas of the image,
$*$: convolution operation sign,
A_k: number of elements of α_k area; same size as PSF.
Thus, the convolution result y (with an omnipresent noise) of a true underlying fluorescent signal x with the PSF h is given by:

$$y = h * x + n \tag{3.1}$$

where the images and the noise are represented by matrices.

So, in order to reverse as said the above process of the convolution of the object with the PSF, a de-convolution process must be realised. Deconvolution methods vary, as de-convolution is not just a simple step back to the original underlying image of the object to be depicted. These methods are computationally complex to some significant degree and so a trade-off between restored image quality and time consumed to produce it has to be determined.

Brief explanation of convolution: Let it be two matrices x and y. x will be convolved with y and the result will be z. y has to be at most the size of x. The operation is as follows: y matrix or else the convolution kernel "scans" x in a top to down and left to right direction. This "scan" is defined as the element-wise multiplication of x and y elements and the assignment of the sum of the multiplications to the central element of the sub-matrix of z that is scanned at that moment. The discrete convolution is mathematically defined as:

$$y[p] = (x * h)[p] = \sum_{\mathbb{N}^3} x[r]h[p - r] \tag{3.2}$$

, given at a 3D location $p \in \mathbb{N}^3$

The above equation can be transformed via notation of linear algebra into a more easily read one:

$$y = Hx + n \tag{3.3}$$

, where n: additive noise
x, y: vectors corresponding to true and observed image respectively. For a 2D image a vector consists of the concatenation of the image rows.
H: circulant matrix corresponding to the convolution operation.

It is not needed to examine further this concept of the convolution with a circulant matrix, since for deconvolution of large or a big group of images it is way too timeconsuming for realistic applications.
Instead, the discrete FT of the Eq. 3.1 is used mostly in the deconvolution algorithms due to higher speed of computation and less used memory compared to non-FT solutions:

$$\hat{Y} = \hat{H} \odot \hat{X} + \hat{N} \tag{3.4}$$

, where the capital letters indicate the corresponding Fourier Transforms. Note: FT of a convolution in the spatial domain gives element-wise multiplication in the frequency domain.

As Fourier analysis states, a periodic signal is considered an infinite sum of sines and cosines of different harmonic frequencies with each sine and cosine contributing with varying amplitude. This can be extended to non-periodic signals, assuming their period is allowed to reach infinity. So, generally FT gives all the frequencies that contribute in building the original signal. In that notion, there exist another transform that uses signals limited in time and frequency, which are termed wavelets, in order to decompose a signal to its contributing wavelets. This transform is called Wavelet Transform. When a wavelet transform is executed, one wavelet from a wide family of wavelets is used. The used wavelet is scaled in time in order to handle higher or lower frequencies of the signal to be decomposed. Wavelet Transforms are used in the algorithm explained at the end of this section Fast Iterative Soft-Thresholding Algorithm (FISTA).

Thinking about solutions to the deconvolution problem, the first thing that comes to mind is to modify Eq. 3.3 (assuming the noise power is low) as $x = H^{-1}y$. This naive approach is proved not to work. The reason is that the inverse problem of deconvolution is known to have a high condition number (rendering it an ill-conditioned problem) which means that a small error in the input causes a big error in the output. This means that from a set of observed images with little differences among them, the estimated "true" images of each observed one will differ significantly. Specifically, the explicit solution is a poor choice since it is sensitive to any noise in the observed image. From the above, it occurs that there is no single solution to the naive inverse deconvolution method.

Thus, the best solution is to find the estimate which provides the best approximation of the true image. To know if a good estimate has been found, the deconvolved image is convolved again with the PSF and it is expected the difference of the observed image with the re-convolved image estimate to be infinitesimal in some way. This difference can be computed in many ways which will be examined in the next chapter.

Generally, the best estimate minimizes a cost function which corresponds to the aforementioned difference or otherwise residual:

$$\mathscr{C}(x) = \|y - Hx\|^2 \tag{3.5}$$

Continuing with the FT-form of the cost function, the $\underset{x}{\operatorname{argmin}}\,\mathscr{C}(x)$ is to be found, or else the x that makes the first derivative of the cost function to be zero. It is true that:

$$\mathscr{C}(x) = (y - Hx)^T(y - Hx) = y^T y - x^T H^T y - y^T Hx + x^T H^T Hx \tag{3.6}$$

, where T denotes the transpose matrix.

From this it follows that:

$$\frac{\partial \mathscr{C}(x)}{\partial x} = 0 \Rightarrow x = H^{-1}y \tag{3.7}$$

or in the Fourier domain:

$$\hat{X} = \frac{\hat{Y}}{\hat{H}} \tag{3.8}$$

As it can be seen, this solution corresponds to the aforementioned naive solution, but in the frequency domain. Since, the FT of the observed image is divided by the FT of the PSF which may contain close to zero elements, it is very probable for the estimate to exhibit very large values, thus resulting in amplifying the already existing noise. A better approach is to add some constraints (regularization) in the cost function which helps easing noise amplification problem.
All the algorithms explained below are in agreement with [20] and [26].

3.3 Inverser Filter Algorithms

3.3.1 Tikhonov Regularization (TRIF)

The cost function is modified as:

$$\mathscr{C}(x) = \|y - Hx\|^2 + \lambda\|x\|_2^2 \tag{3.9}$$

, where λ is the regularizing parameter that balances the contribution of the two terms and penalizes absolute high values of the solution. It consists a trade-off between data fidelity and regularization, since transition in absolute high values might be image details as well as noise. So, higher λ gives a smoother image. Minimization of such a problem (where more than one unkown terms appear) can be solved with Lagrange multipliers. The solution is given by:

$$x = (H^T H + \lambda I)^{-1} H^T y \tag{3.10}$$

, where I is the identity matrix. This can be expressed in the Fourier domain as:

$$\hat{X} = \frac{\overline{\hat{H}}\hat{Y}}{\overline{\hat{H}}\hat{H} + \lambda 1} \tag{3.11}$$

, where $\overline{\hat{H}}$ denotes the conjucate of $\hat{H}$ and 1 is a matrix of ones. When equations refer to the frequency domain, $\odot$ is omitted for simplification.

3.3.2 Regularized Inverse Filtering (RIF)

This method uses a cost function that when minimized it imposes smoothness on the estimate. That is accomplished by penalizing high values of the 2^{nd} derivative of $\hat{X}$. That is, the cost function becomes:

$$\mathscr{C}(x) = \|y - Hx\|^2 + \lambda \|Lx\|_2^2 \tag{3.12}$$

, where L is a differential operator, like the Laplacian operator ∇^2.

Differentiation of an image acts as a high-pass filter, so minimization also of the 2nd term of the $\mathscr{C}(x)$ ends up in a smoother solution. But yet again, the "amount" of smoothness imposed, depends on λ. Again the method of Lagrange multipliers gives the solution:

$$x = (H^T H + \lambda L^T L)^{-1} H^T y \tag{3.13}$$

In the Fourier domain, this is expressed as:

$$\hat{X} = \frac{\overline{\hat{H}}\hat{Y}}{\overline{\hat{H}}\hat{H} + \lambda \overline{\hat{L}} L} \tag{3.14}$$

Note: this FT solution gives a generalization of the classic Wiener filtering solution. To derive Wiener filtering solution, λ is defined as $1/\sigma_n$, with σ_n the noise variance. Also $L^T L$ must impose a whitening transformation on x.

3.3.3 Wiener Filter

The Wiener filter integrates an estimated Noise-to-Signal power ratio (NSR). The solution is expressed as:

$$\hat{X} = \frac{\overline{\hat{H}}\hat{Y}}{\overline{\hat{H}}\hat{H} + NSR} \tag{3.15}$$

3.4 Constrained Iterative Algorithms

Inverse filtering algorithms suffer from sensitivity to the PSF. Small errors in the estimation of the PSF may result in major artifacts in the solution. An alternative to this, is the option of iterative methods. They minimize a residual/cost function as well as inverse algorithms do, but by generating a series of improving approximate solutions. Often, the Wiener Filter solution is used as the initial guess. The advantage of them in contrast to the inverse solutions is that estimates exhibit better stability and less sensitivity to errors of the PSF. The disadvantage is though, that they are computationally intense.

3.4.1 Landweber LW

This algorithm minimizes the unregularized $\mathscr{C}(x)\|y - Hx\|^2$ using the iterative gradient descent approach. More specifically, one way to find the local minimum of a general function $F(x)$ starting from a particular point α, is to iteratively take steps proportional to the negative of the gradient of the function at the current point. This is because $F(x)$ decreases faster if we move against the direction of $\nabla F(\alpha)$

So, starting with α and with b being the next point closer to the local minimum of $F(x)$ (or global if $F(x)$ is convex), we reach b via: $b = \alpha - \gamma \nabla F(x)$, with γ being the step size or relaxation factor describing the speed of convergence of this method.

Thus, this can be expanded to more iterations and with an initial guess x_0 and the sequence $x_0, x_1, x_2, ..., x_n$ we take the gradient descent general solution:

$$x_{n+1} = x_n - \gamma_n \nabla F(x_n), \quad n \geq 0 \tag{3.16}$$

The importance of the step size can be explained with the concept of the level sets. A level set is a set where the function takes on a given constant value. This can be visualized in Fig. 3.1. In the center, the minimum of the function resides. In this case, the wider the "circle", the bigger the value of the function. So, taking little steps each time against the derivative of the function in a point of a "circle", directs us to the minimum in the center. Here, we can see that the size of the step plays an important role, in the issue of convergence to our solution. Specifically, A small step-size guarantees convergence, but leads to very slow convergence, meaning more time to reach the center. On the other hand, A big step leads to faster but less stable convergence (more like circling around the center).

To continue with the gradient descent solution the gradient of $\mathscr{C}(x)$ must be computed.

$$\nabla \mathscr{C}(x) = -H^T y + H^T H x = -H^T (y - Hx) \tag{3.17}$$

The same applies for vector functions, so substituting the gradient in the Eq. 3.16 gives:

$$x_{n+1} = x_n + \gamma H^T (y - Hx), \quad 0 < \gamma < 2/\sigma_1^2 \tag{3.18}$$

where σ_1 the largest singular value of H, that is $\sqrt{\lambda_{max}(H^T H)}$

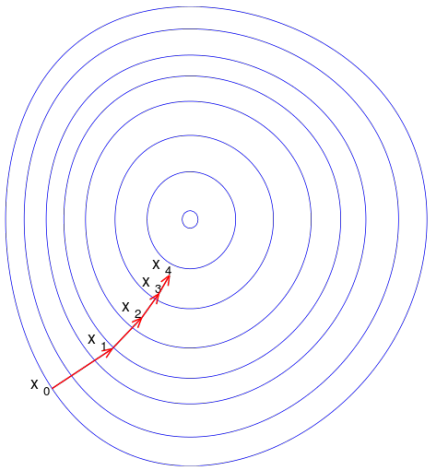

Figure 3.1: Gradient descent
Source: `https://en.wikipedia.org/wiki/Gradient_descent`

When Fourier Transforms signals are inversed, the spatial-domain result exhibits some overshoots and undershoots, especially in high-contrast areas where the signal drops or rises abruptly. When undershoots happen they may cause the signal to have negative values at some points. For this reason, a non-negative projection must be imposed to the values of the result:

$$\mathscr{P}_{(\Re^+)}\{x\} = max(x, 0) \tag{3.19}$$

Hence, the final form of the solution becomes:

$$x_{n+1} = \mathscr{P}_{(\Re^+)}\{x_n + \gamma H^T(y - Hx_n)\}, \quad 0 < \gamma < 2/\sigma_1^2 \tag{3.20}$$

For the sake of speed, the above equation can be modified as below. In that way, each iteration performs fewer operations. Thus, the solution becomes:

$$x_{n+1} = \mathscr{P}_{(\Re^+)}\{Ax_n + G\}, \quad 0 < \gamma < 2/\sigma_1^2 \tag{3.21}$$

, where $A = I - \gamma H^T H$ and $G = \gamma H^T y$
In the practical form for algorithms, this is expressed as:

$$x_{n+1} = \mathscr{P}_{(\Re^+)}\{\mathscr{F}^{-1}\{\hat{A}\hat{X} + \hat{G}\}\}, \quad 0 < \gamma < 2/\sigma_1^2 \tag{3.22}$$

, where $\mathscr{F}^{-1}$: inverse Fourier Transform
$\hat{A} = 1 - \gamma\overline{\hat{H}}\hat{H}$ and $\hat{G} = \gamma\overline{\hat{H}}\hat{Y}$

3.4.2 Iterative Constrained Tikhonov-Miller (ICTM)

Iterative Constrained Tikhonov-Miller algorithm (ICTM) uses iterative gradient descent to minimize the Regularized Inverse Filter (RIF) cost function (Eq. 3.12). The gradient of C (x) is:

$$\nabla \mathscr{C}(x) = -H^T y + (H^T H + \lambda L^T L)x \tag{3.23}$$

Substituting in the gradient descent equation (Eq. 3.16) with projection to $\Re^+$ gives the ICTM solution:

$$x_{n+1} = \mathscr{P}_{(\Re^+)}\{\, x_n + \gamma(H^T y - (H^T H + \lambda L^T L)x_n)\,\} \tag{3.24}$$

As in the LandWeber algorithm (LW) solution, the ICTM solution is modified as:

$$x_{n+1} = \mathscr{P}_{(\Re^+)}\{Ax_n + G\} \tag{3.25}$$

,where $A = I - \gamma(H^T H + \lambda L^T L)$ and $G = \gamma H^T y$

In the practical form for algorithms, this is expressed as:

$$x_{n+1} = \mathscr{P}_{(\Re^+)}\{\mathscr{F}^{-1}\{\hat{A}\hat{X} + \hat{G}\}\} \tag{3.26}$$

, where $\hat{A} = 1 - \gamma(\overline{\hat{H}}\hat{H} + \lambda\overline{\hat{L}}\hat{L})$ and $\hat{G} = \gamma\overline{\hat{H}}\hat{Y}$

3.4.3 Jansson-Van Cittert (JVC)

The Eq. 3.3 can be manipulated in the following way:

$$y - Hx = 0 \Rightarrow y - Hx + x = x \tag{3.27}$$

In iterative form, along with the use of some weighting coefficients and the nonnegative projection, the Jansson-Van Cittert algorithm (JVC) solution is:

$$x_{n+1} = \mathscr{P}_{(\Re^+)}\{x_n + w \odot (y - Hx)\} \tag{3.28}$$

, where W: weighting coefficient matrix defined as:

$$K[1 - \frac{2}{B - A}|x_n - \frac{A + B}{2}|] \tag{3.29}$$

A, B: min and max values of x_k respectively, K: constant

In the practical form for algorithms, this is expressed as:

$$x_{n+1} = \mathscr{P}_{(\Re^+)}\{x_n + w \odot \mathscr{F}^{-1}\{\hat{Y} - \hat{H}\hat{X}\}\} \tag{3.30}$$

This algorithm is quite straightforward and simple, but it exhibits slow convergence to an acceptable solution. This might mean that more iterations are needed. However, due to the fact that JVC does not take into account the additive noise of the image, as iterations increase it is possible that resonance effects will be created and constructive image artifacts will be generated. To partially overcome these problems, the initial guess is filtered with a Gaussian or a Wiener filter and each of 4-7 iterations is smoothed with a Gaussian filter of variable width.

3.4.4 Gold

This algorithm manipulates the Eq. 3.3 in a way to form an iterative multiplicative solution. Note: the multiplications and division are element-wise.

$$y = Hx \Rightarrow \frac{y}{Hx} = 1 \Rightarrow \frac{y}{Hx}x = x \Rightarrow$$
$$x_{n+1} = \mathscr{P}_{(\Re^+)}\left\{x_n \frac{y}{Hx}\right\}$$

In the practical form for algorithms, this is expressed as:

$$x_{n+1} = \mathscr{P}_{(\Re^+)}\left\{x_n \frac{y}{\mathscr{F}^{-1}\{\hat{H}\hat{X}\}}\right\}$$

The same conclusions of JVC apply to the GOLD algorithm, although multiplicative formulation of GOLD gives a more rapid convergence than JVC.

3.4.5 Richardson-Lucy (RL)

The previously examined algorithms did not took into consideration any existing noise. But, the statistical information of the noise in the observed image y can be used in order to reconstruct a more precise image. To find the estimate x, one must answer to the question: Which image of the very many possible ones, is the most likely to be the desired underlying true image x, given the noisy image y?. The meaning of probability is actually in terms of a normalized frequency of photon events in each image pixel.

The above x and y symbols denote the image matrices. So, the unknown x is expressed as:

$$\hat{x} = \underset{x}{\operatorname{argmax}}\, p(x|y) \tag{3.31}$$

, where $\hat{x}$ denotes the estimated image x.

Thus, the estimate is the image with the Maximum A Posteriori (MAP) probability.
It is known that:

$$p(x|y) = \frac{p(x,y)}{p(y)} = \frac{p(y|x)p(x)}{p(y)} \tag{3.32}$$

From the two above equations it follows that:

$$\hat{x} = \underset{x}{\operatorname{argmax}}\, p(y|x)p(x) \tag{3.33}$$

This is equal to minimizing the negative logarithm of the argument, providing the cost function:

$$\mathscr{C}(y,x) = -\,ln\, p(y|x) - \lambda\, ln\, p(x) = L(y,x) + \lambda\, \Omega(x) \tag{3.34}$$

, where λ: regularization parameter, $\Omega(x)$: smoothing function.

There are two subfamilies of algorithms. Those that do not use the regularization function and follow a Poisson-distributed noise and those that use the regularization function but follow a Gaussian-distributed noise for the sake of math simplification. Richardson-Lucy belongs to the first category, which minimizes the likelihood $y|x$, thus making it a Maximum Likelihood Estimation (MLE) algorithm.

In the Richardson Lucy algorithm (RL) concept, every image pixel follows the Poisson distribution, that is the probability of obtaining a noisy pixel y_m given its noise-free averaged value μ_m, which is expressed as:

$$p(y_m|\mu_m) = \frac{\mu_m^{y_m} e^{-\mu_m}}{y_m!} \tag{3.35}$$

Every pixel is statistically independent from the others, so the probability of the whole image is equal to the product of the individual probabilities, giving:

$$p(y|x) = p(y|\mu) = \prod_m p(y_m|\mu_m) = \prod_m \frac{\mu_m^{y_m} e^{-\mu_m}}{y_m!} \tag{3.36}$$

Substituting the above expression into the cost function $\mathscr{C}(y,x) = -ln\, p(y|x)$ gives:

$$\mathscr{C}(y,x) = \sum_m (\, \mu_m - y_m\, ln\, \mu_m + ln\, y_m! \,) \tag{3.37}$$

Since μ is the image of the noise-free averaged pixel values, it is true that μ is actually the noise-free convolution of the true image x and the PSF h (see Eq. 3.1). That is: $\mu = y * h$. Since, though, the $\mathscr{C}(y,\mu)$ contains a sum, it is better to express the convolution (for a single image pixel) in the sum form as: $\mu_m = \sum_l h_{l-m}\, x_l$

So, by setting the derivative of the $\mathscr{C}(y, x_l)$ to zero, with respect to x_l, it follows that:

$$\frac{\partial \mathscr{C}(y, x_l)}{\partial x_l} = \sum_l \left(h_{m-l} \frac{y_l}{\sum_n h_{n-l}\, x_n} \right) - 1 = 0 \tag{3.38}$$

Manipulating the above equation in order to convert it to an iterative multiplicative form, it gives:

$$x_m^{k+1} = K\, x_m^k \left(\sum_l \left(h_{m-l} \frac{y_l}{\sum_n h_{n-l}\, x_n} \right) \right) \tag{3.39}$$

, where K: normalizing energy constant.

This can be written back again to the convolution and matrix notation, as in this way the solution can be executed in the Fourier Transform domain:

$$x^{k+1} = x^k \odot h^T * \left(\frac{y}{h * x^k} \right) \tag{3.40}$$

, where multiplication and division are element-wise and h^T is the flipped PSF matrix.

From the above solution it is apparent that the implementation of the RL algorithm is easy as long as no extra parameters are included. Since noise is integrated in the algorithm, RL is generally more robust to noise than the aforementioned methods. However, RL exhibits very slow convergence to an acceptable image-solution, because it takes more computing time per iteration than the previously mentioned classical algorithms.

3.4.6 Richardson-Lucy Total Variation (RL-TV)

As examined in the previous methods, a regularization in the final solution helps counterbalancing noise amplification. The same can be applied in the RL solution. Specifically, regularization is achieved by minimizing the total variation of the image which is defined as the integral of the absolute gradient of the image. To put it practically, the total variation of a 1D signal is the length of the curve defining the signal itself. This can be expanded for images too. So, to derive the solution image, a mutual minimization of the cost function of the RL (Eq. 3.37) plus the total variation of the image must happen. In a convolution and matrix notation along with a regularization factor, this can be expressed as:

$$\mathscr{C}(x) = h * x - y\, ln(h * x) + \lambda \parallel Dx \parallel_1 \tag{3.41}$$

, where D: 1^{st} order differentiation operator of x,

λ: regularization parameter.

To derive the minimized solution from the $\mathscr{C}(x)$) a multiplicative form of the gradient descent method is used:

$$x_{k+1} = x_k \left[-\lambda \nabla \mathscr{C}(x_k)\right] \Rightarrow$$
$$\Rightarrow x_{k+1} = x_k \odot h^T * \left(\frac{y}{h * x_k}\right) \odot \frac{1}{1 + \lambda\, g_k}$$

, where g_k: the derivative of a regularized version of $\| Dx \|_1$
Note: The L1 norm penalization is known to better preserve image discontinuities compared to L2 norm.

3.4.7 Fast Iterative Soft-Thresholding Algorithm (FISTA)

Alternative regularization terms to the cost function of RIF (Eq. 3.12) can be considered. In particular, sparsity (regularization) constraints in the wavelet domain have proven to yield better preservation of image details and discontinuities. The associated cost function is:

$$\mathscr{C}(x) = \| y - Hx \|_1^2 + \lambda \| W\, x \|_1 \tag{3.42}$$

, where W: a Wavelet Transform operator

Due to the nonsmoothness of the l_1 norm, gradient-descent algorithms cannot be used. However, the problem can be solved efficiently by fast iterative soft-thresholding with the following iterations:

$$z_{n+1} = s_n - \gamma H^T (H\, s_n - y) \tag{3.43}$$

$$x_{n+1} = W^T\, \mathscr{T}(W z_{n+1},\, \gamma\, \lambda) \tag{3.44}$$

, where $\mathscr{T}(\cdot, \tau)$: a soft-thresholding operator with threshold τ.

In general, soft-thresholding means that a signal is srunk into a region determined by the following. When a particular signal value $x \in [-\tau, \tau]$, it becomes 0. When $x > |\tau|$, then it acquires the value $sign(x) \cdot (|x| - \tau)$.

$$p_{n+1} = \frac{1}{2}\left(1 + \sqrt{1 + 4p_n^2}\right) \tag{3.45}$$

$$s_{n+1} = x_{n+1} + \frac{p_n - 1}{p_{n+1}}(x_{n+1}) - x_n \tag{3.46}$$

Again, it is better the equations containing convolution operations to be expressed in the Fourier domain.

3.4.8 Blind Deconvolution

All the previously examined algorithms demand the knowledge of the PSF. But when acquiring the PSF is proved to be difficult for reasons of any kind, then an alternative approach is the use of blind deconvolution methods. They are termed "blind" because they try to estimate the true image out of the blurred one without knowing the impulse response function of the optical system (PSF). So, in order to start making guesses about the estimate, they must apply some constraints both on the estimate and the PSF. The constraints on the estimate may have the form of non-negativity, finite support with the latter referring to the smallest rectangle within which the true object is contained. Finite support has effect on fluorescence and astronomy images where objects are easily identified. The constraints on the PSF may have the form of symmetry, finite support, known parametric form with the latter meaning a particular type of blurring like defocus or camera motion blur.

Implementations of this category of algorithms may vary. In the next chapter, the blind deconvolution is realised with the algorithm explained below (as implemented in the Image Processing Toolbox of MATLABR). Again, x denotes the true image vector, y the observed image vector and h the PSF image vector.

The algorithm uses the standard MLE algorithm described above, together with a PSF estimation for each iteration. The object is computed, using the MLE estimation, as follows:

$$x^{k+1} = Kx^k \odot h^T * \left(\frac{y}{h * x^k} \right) \tag{3.47}$$

Using exactly the same mathematical reasoning, PSF is estimated by maximizing the log likelihood function with respect to h, which gives:

$$h^{k+1} = \frac{1}{N} h^k \odot x^T * \left(\frac{y}{x * h^k} \right) \tag{3.48}$$

, where N is a normalization constant relating to the unit volume.

The following iterations take place as implemented in MATLAB. At first, estimate and PSF predictions (j and k respectively) using the non-negativity constrained are made:

$$j = \mathscr{P}_{(\Re^+)} \left\{ x_n + \lambda_{x,n}(x_n - x_{n-1}) \right\} \tag{3.49}$$

$$k = \mathscr{P}_{(\Re^+)} \left\{ h_n + \lambda_{h,n}(h_n - h_{n-1}) \right\} \tag{3.50}$$

As for the h_0, an initial PSF is assumed. The critical part of the assumption is the initial PSF image size, rather than an attempt to find a good PSF approach. Note: k is normalised so that the PSF pixels sum to the value 1. Normalization is a necessary constraint because given only input image, the algorithm cannot know how much power is in the image vs the

PSF.

$\lambda_{x,n}$ is a coefficient for the estimate prediction that is computed by:

$$\lambda_{x,n} = \alpha_{x,n}^T \beta_{x,n} / \beta_{x,n}^T \beta_{x,n} \quad , \quad 0 \leq \lambda_{x,n} \leq 1 \tag{3.51}$$

Where:

$$\alpha_{x,n} = x_n - j \tag{3.52}$$

and

$$\beta_{x,n} = \alpha_{x,n-1} \tag{3.53}$$

$\lambda_{h,n}$ is a coefficient for the estimate prediction that is computed by:

$$\lambda_{h,n} = \alpha_{h,n}^T \beta_{h,n} / \beta_{h,n}^T \beta_{h,n} \quad , \quad 0 \leq \lambda_{h,n} \leq 1 \tag{3.54}$$

Where:

$$\alpha_{h,n} = h_n - k \tag{3.55}$$

and

$$\beta_{h,n} = \alpha_{h,n-1} \tag{3.56}$$

The above computed estimate and PSF predictions are used in the Richardson-Lucy algorithm that produces the deconvolved estimate of the true image in each iteration.

3.4.9 Self-Deconvolving Data Reconstruction Algorithm (SeDDaRA)

The Self-Deconvolving Data Reconstruction Algorithm (SeDDaRA), [16] is based on the premise that there is enough knowledge of the scene statistics that a suitable model of the scene can be found. Thus, a reference image with similar spatial frequency content, but no blur, is used as a model to extract the blur from the target image.

The mathematical representation of the blurred image $g(x, y)$ is

$$g(x, y) = f(x, y) \odot d(x, y) + w(x, y) \tag{3.57}$$

, where $f(x, y)$ is the real scene $d(x, y)$: the point spread function (PSF) $w(x, y)$: a noise term $\odot$: indicates convolution.

Application of a Fast Fourier Transform (FFT) produces:

$$G(u,v) = F(u,v)D(u,v) + W(u,v) \tag{3.58}$$

, where u, v: the coordinates in frequency space, and the transformed functions are represented by capital letters.

If $d(x,y)$ is known, a deconvolution process can be applied to $g(x,y)$ to estimate $f(x,y)$. For this effort, a pseudo-inverse filter, an approximation of the Wiener filter, has been used. It is a fast process and very robust, and has been shown as effective as iterative deconvolution approaches. [7], [15] The deconvolution is given by:

$$F(u,v) \approx \frac{G(u,v)D^*(u,v)}{|D(u,v)|^2 + C_2} \tag{3.59}$$

where the parameter C_2 is typically chosen as 0.01 multiplied by the average of $|D(u,v)|$. The constant acts as a tuning parameter to guard against amplification of the image noise.

The SeDDaRA process assumes the PSF is space-invariant and has the form:

$$D(u,v) = \Big[K_G \, S \, \{ \, |G(u,v) - W(u,v)| \, \} \Big]^{\alpha(u,v)} \tag{3.60}$$

, where $\alpha(u,v)$ is a tuning parameter
K_G is a real, positive scalar chosen to ensure $|D(u,v)| \leq 1$ $S\{...\}$ a smoothing filter which its application assumes that $D(u,v)$ is a slowly varying function.
Assumptions for this calculation are explained in reference [16].

After some derivation, $\alpha(u,v)$ is found to be:

$$\alpha(u,v) \approx \frac{ln\Big[K_G \, S \, \big|G(u,v) - W(u,v)\big| \Big] - ln\Big[K_{F'} \, S \Big\{ \big|F'(u,v)\big| \Big\} \Big]}{ln\Big[K_G \, S \, \big|G(u,v) - W(u,v)\big| \Big]} \tag{3.61}$$

, where $F'(u,v)$ is a reference image that satisfies:

$$K_{F'} \, S \Big\{ \big|F'(u,v)\big| \Big\} \approx K_F \, S \Big\{ \big|F(u,v)\big| \Big\} \tag{3.62}$$

The presence of a smoothing filter greatly relaxes this condition. In Equation 3.61 K_G and $K_{F'}$ must be determined such that $|D(u,v)| \leq 1$. This condition is satisfied if we set:

$$K_G = \frac{1}{max\left[S\left\{\left|G(u,v)\right|\right\}\right]} \tag{3.63}$$

$$K_{F'} = \frac{1}{max\left[S\left\{\left|F'(u,v)\right|\right\}\right]} \tag{3.64}$$

However, as first reported in Reference [23], SeDDaRA can be approximated by expressing $\alpha(u,v)$ as a constant of frequency α. The value α depends on scene statistics, but often $\alpha = 0.5$ is an appropriate choice. The constant-frequency approximation is often as effective as Equation 3.61, particularly when the PSF has rotational symmetry. Once $D(u,v)$ has been extracted from the averaged image, both functions are inserted into Equation 3.59 to remove the blur. Application of an inverse FFT produces the restored image.

3.5 Artifacts

3.5.1 Ghost Artifacts, Zero-Padding and Edge Tapering

Data subjected to a FFT must necessarily be assumed to be periodic. This implies that borders at opposite sides of the image are implicitly adjoined once periodization is taken into account. Consequently, structures near the borders of an image, once processed, will spill over the opposite border, letting ghosts appear. For this reason, images can be padded with zeros beyond all edges, resulting in an expanded image with dark regions around. If the padding is sufficient the ghost artifacts appear only in the dark regions. Finally, ghosts are cropped out. If it is not wanted images to be expanded, another solution is to blur the regions near the boundaries with the PSF, easing in that way the effect of ghosts after deconvolution. This technique is called edgetapering.

3.5.2 Ringing Artifacts and Early Stopping

As far as all the algorithms are concerned, as it was previously explained in the Landweber algorithm section, inversed signals from the Fourier domain to the spatial one exhibit some overshoots and undershoots in areas of discontinuities and high signal jumps. Fourier Transform is performed in a discretized form allowing a finite number of harmonics to contribute in building the original signal. It is apparent that, the more harmonics included the better the representation of the original signal and the less the oscillations. However, these oscillations do not die out as the number of harmonics increases, but they reach a limit. This peculiar fact is known as the Gibbs phenomenon and explains the cause of ringing artifacts in images being processed with Fourier Transforms.

Hence, oscillations are imposed progressively on oscillations caused by FT. So, in order

to avoid ringing artifact amplification in high contrast areas of images, the number of iterations is preferable not to exceed a limit which can be better found by eye-evaluation of the resulted image. Algorithms in general though, can integrate such an early stopping criterion with the aid of quantitative metrics. Specifically they choose to stop the iterations, when they "see" that no substancial changes are made to the image.

Chapter 4

Quantitative Metrics

After the deconvolution process is done, evaluating the quality of the result can be done in several ways.

4.1 Residual Norm

By reblurring the true image estimate (x) after the deconvolution process, it can be seen how similar this degraded image is with the original (y). If the reblurred image is close to the original image, this means that the deconvolution process worked effectively. The reblurred image is constructed convolving the deconvolution result with the PSF (circulant matrix H).

Hence, the difference $y - Hx$ is desired to be computed. This is called the residual between y and Hx. In order to obtain a single scalar number index, the sum of the squared values of the elements of the residual image [4] or equivalently the squared l_2 norm of the residual image is computed and normalized by the square root of the total number of the residual elements. This is written as:

$$ResidualNorm = \frac{1}{\sqrt{numel}} \|y - Hx\|_2^2$$

, where $numel$: total number of residual image pixels

4.2 I-Divergence

Based on the Kullback–Leibler divergence [17] which is a measure of how a probability distribution diverges from a second expected probability distribution, a metric of difference between images can be computed. Probability distributions are substituted by the images which therefore gives a modified Kullback-Leibler measure, called I-divergence:

$$I - divergence = \sum_{ij} \left\{ (Hx)_{ij} * ln \frac{(Hx)_{ij}}{y_{ij}} - \big((Hx)_{ij} - y_{ij}\big) \right\}$$

, where subscripts i, j denote the image pixel of the i-th row and the j-th column.

4.3 Structural Similarity Index (SSIM)

Structural SIMilarity indexs (SSIMs) [30] is a perception-based model that considers image degradation as perceived change in structural information, while also incorporating important perceptual phenomena, including both luminance masking and contrast masking terms. Structural information is the idea that the pixels have strong inter-dependencies especially when they are spatially close. These dependencies carry important information about the structure of the objects in the visual scene. Luminance masking is a phenomenon whereby image distortions tend to be less visible in bright regions, while contrast masking is a phenomenon whereby distortions become less visible where there is significant activity or "texture" in the image. The SSIMs index is calculated on various windows of an image. The SSIMs formula u and v (of Hx and y respectively) of common size $N \times N$. These comparison measurements concern luminance (l), contrast (c) and structure (s). The product of them produces the following formula in its final form:

$$SSIM(u,v) = \frac{(2\mu_u\mu_v + c_1)(2\sigma_{uv} + c_2)}{(\mu_u^2 + \mu_v^2 + c_1)(\sigma_u^2 + \sigma_v^2 + c_2)}$$

, where μ_u: average of u
μ_v: average of v
σ_u^2: variance of u
σ_v^2: variance of v
σ_{uv}: covariance of u and v
c_1, c_2: variables to stabilize divisions with weak denominators.

4.4 Full Width At Half Maximum (FWHM)

4.4.1 Spatial Resolution

[6] Spatial Resolution refers to the ability of the camera to image two separate objects as they are moved closer and closer to each other in space. One measure of spatial resolution is known as the Full-Width at Half Max (FWHMs) resolution, and is probably the correct method to accurately determine the resolving Power of the camera. If the two objects must be 2 mm apart to be seen as two distinct objects, (as opposed to one single blurred object), the spatial resolution is said to be 2 mm.

Use two sources of the isotope to be imaged:

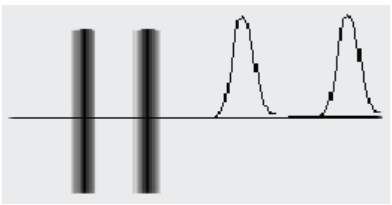

Figure 4.1: Two sources of the isotope

Move the sources toward each other and measure the separation at which the images of the two points cannot be distinguished.

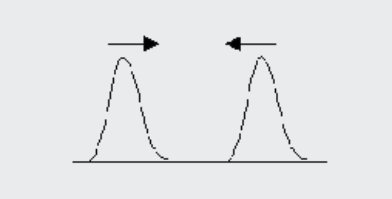

Figure 4.2: Moving sources toward each other

Note that the images will blur together completely at a separation approximately equal to the full-width at half maximum (FWHM) of the image of the point. When the resolution is specified as a single number, that number is usually the FWHM of the point-source image.

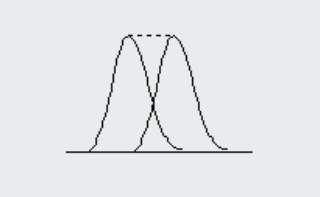

Figure 4.3: The images of the two points cannot be distinguished at fwhm separation

The smaller the number of FWHM, the Better the Spatial Resolution

4.4.2 FWHM in astronomy

[1] The technical term Full-Width Half-Maximum, or FWHM, is used to describe a measurement of the width of an object in a picture, when that object does not have sharp edges. A simple box can be described just by its width, and a rectangle by its width and height. However, the image of a star in an astronomical picture has a profile which is closer to a Gaussian curve, given mathematically by $\exp(-x^2/2\sigma^2)$ or graphically as:

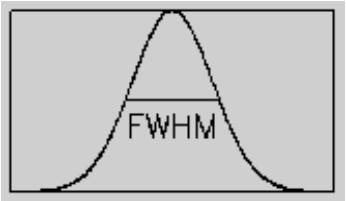

Figure 4.4: The Full Width at Half Maximum

In order to compare different profiles, we can use the Gaussian parameter in the denominator of the mathematical expression, usually represented by the Greek letter sigma (σ). This does not really describe the extent of the profile, but we cannot use the "total width" of the profile, because it extends forever, albeit at a very low level after a distance of a few times sigma. An alternative, which better reflects the approximate size of the star's

image as seen by the eye, is the width across the profile when it drops to half of its peak, or maximum, value (shown in the graph above). This is the full width of the image at half maximum value, or full-width half-maximum, or FWHM. It is a simple and well-defined number which can be used to compare the quality of images obtained under different observing conditions. In the usual sort of astronomical image, the FWHM is measured for a selection of stars in the frame and the "seeing" or image quality is reported as the mean value.

As far as microscopy is concerned, we can use this technique by taking manually selected profiles of a microscope image that include a peak, and measuring FWHM. As we will see below, we can use these metrics as a benchmark for spatial analysis that deconvolution algorithms achieve, since we are interested in seeing the differences between algorithms rather than the value of FWHM itself.

4.5 Deconvolution Results Comparison Method

Having all the results in our hands, an important question that arises is that of comparing them. By comparing we mean, evaluating and classifying them according to their performance in specific features. In the present diploma the results are approached from various angles so as to create a relatively complete comparison between them. The features examined in this diploma are described below:

4.5.1 Peak Score

The main feature of interest is the quantification of the increase in spatial resolution of the image. This is what we try to achieve locally by measuring FWHMs, at manually selected signal peaks. The smallest value means that the algorithm is more aggressive and the result is better focused. If we have an equal FWHM, we also take into account the maximum value of each peak (Fig. 4.5). This easily results in a "Peak Score" where is the ratio of the maximum value of peak to FWHM. The higher the "Peak Score" the greater and the spatial resolution and the value of the contrast.

In the case where the lowest value of our signal, as in our case, is not zero, we assume that the peak height starts from the lowest value, more specifically, the background intensity value as shown in Fig. 4.6

Finally, the formula for Peak Score is:

$$Peak\_Score = \frac{Peak\_Height}{FWHM} = \frac{f_{max} - f_{bg}}{FWHM}$$

4.5.2 Signal And Background Score

Even if one result has a better spatial resolution than another, it may not be valid because of the increase in variance and noise due to the aggressiveness and sensitivity of the algorithm to it. In an image whose tensions belong to a small range of values (i.e. monochromatic), noise can be considered the expected value of the deviation of the stresses from their mean value. By measuring the standard deviation in manually selected areas of the same intensity

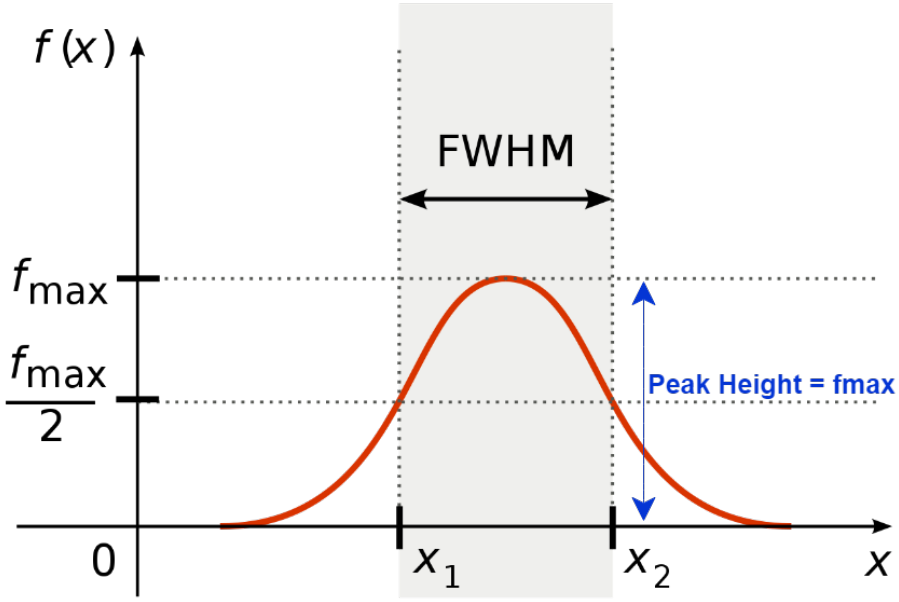

Figure 4.5: FWHM and Peak Height measures

values of each sample's image, for both the background and the signal, we can approximate the noise of the image in these areas. This results in two new values, the "signal score" being the mean value of the signal decreasing the noise degradation (i.e., standard deviation of signal) and respectively the "background / noise score" that is the background / noise average plus the "upgrading" due to noise (ie, standard deviation of background).

$$Signal\_Score = Signal_{Mean} - Signal_{std}$$

$$Background\_Score = Background_{Mean} + Background_{std}$$

4.5.3 SNR Score

Qualitatively, the existence of noise results in visually confusing high noise levels (background-noise) with low (and not only) signal values (for example signal score) so that the structural features of the image not to become discrete or even to change their structure. Thus, it would be legitimate to have an indicator that quantifies this relationship of signal and noise. This can be expressed by the signal-to-noise ratio (SNR). [5]

We consider "SNR score" the signal score to the background-noise score. The higher the SNR score, the more distinct are the structural features of the image and the noise has a lesser effect on the image.

$$SNR\_Score = \frac{Signal\_Score}{Background\_Score}$$

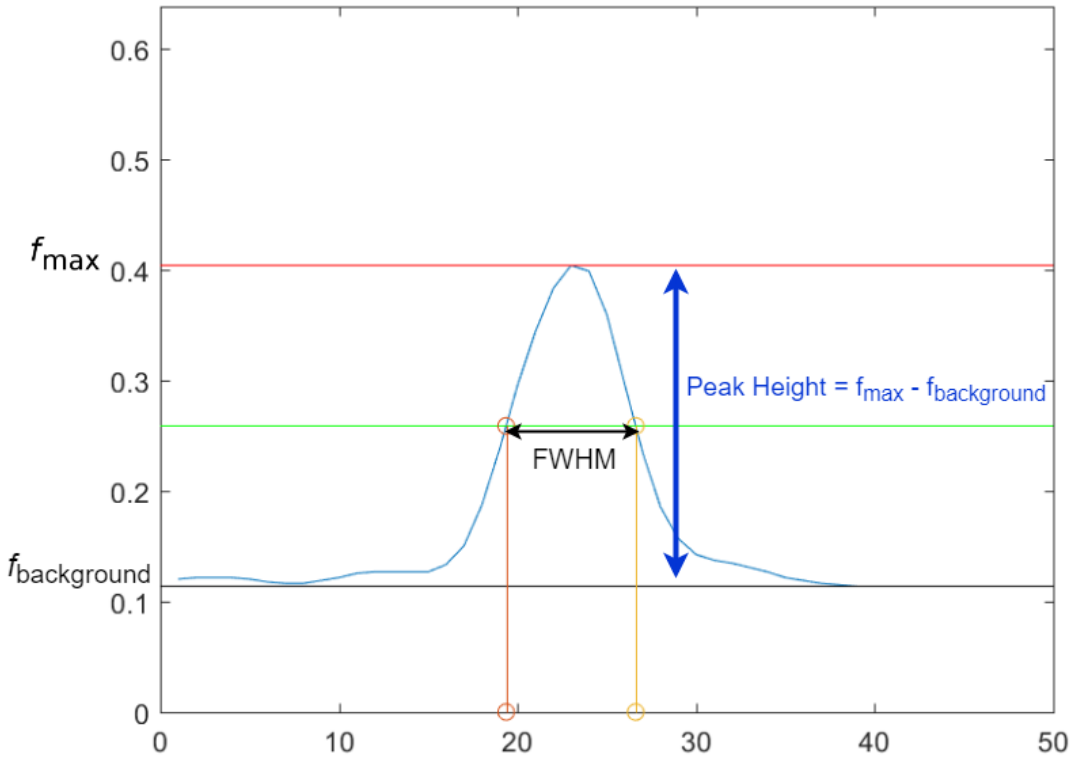

Figure 4.6: FWHM and Peak Height measures with non zero background

4.5.4 Histogram Score

Another feature we look at is the change in the histogram of the image.[8] When the values of the intensities from the useful image data are better distributed, then we have a better overall contrast. The standard deviation of the histogram shows how "stretched" are the intensities in the histogram are. The smaller the value of the standard deviation, the more concentrated the intensity values are in a range, the contrast of the image is smaller than an image with a larger standard histogram deviation, where the values are spread over or over the range prices. We consider "Histogram Score", the standard deviation of the histogram of the image.

$$Histogram\_Score = Histogram\_std$$

4.5.5 Final Score

At this point, it is advisable to point out that the way the areas are selected for the measurements, because it is manual and it is at the discretion of the user to choose the right areas affects the results, but not in a way that changes the classification of the algorithms among them. Also for the same reason, this comparison method can not be generalized and automated for each different sample and should be done on each sample separately. How-

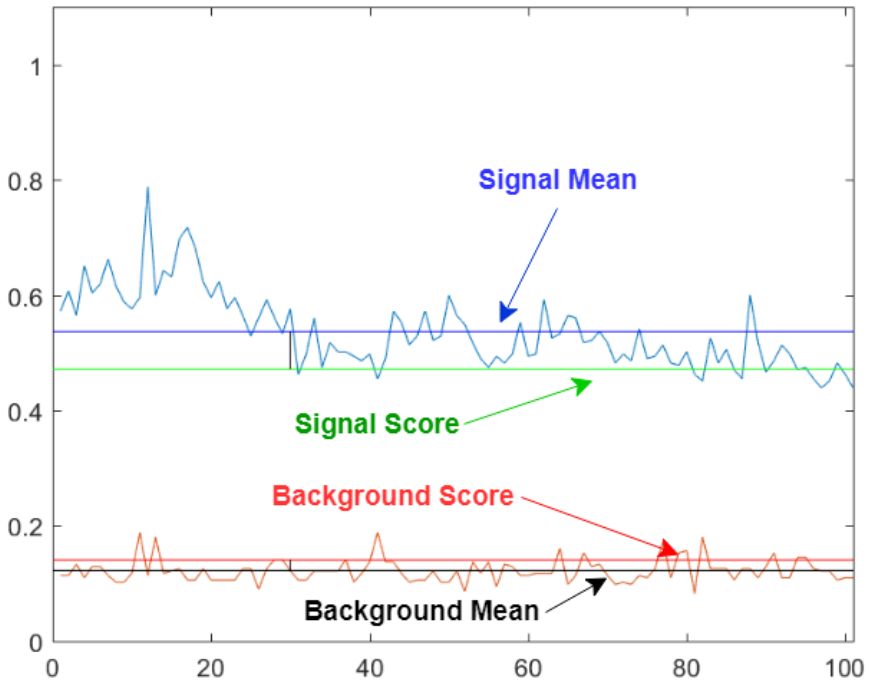

Figure 4.7: Application GUI - start page

ever, each classification could be considered a guide for samples of the same type each time. Having these metrics, in the end, we create a ranking of algorithms and we have a general score of success and validity of the results they produce. We also have a hint on what the practical behavior of each algorithm is in each sample.

The formula that gives us the final score results from the combination of all the "score-scores" as shown below:

$$Final\_Score = Peak\_Score * SNR\_Score * Histogram\_Score$$

Chapter 5

GUI Explanation

The GUI developed for this diploma thesis is built on MATLABR App Designer and is supported in versions: R2017a +. The GUI integrates a set of deconvolution inverse and repetitive algorithms, the ability to export MTF and PSF using the "Slanted Edge" method (and optionally the "Fluorescence Microspheres" method), creating, processing, and exporting comprehensive results comparison reports with final classification according to the validity of the results (Final Score) accompanied by the corresponding files (pictures, diagrams, etc.). There is also the ability to import focused image to compare and produce deconvolution results for further research (such as artificially constructed images and more).

5.1 Getting to know the GUI

By opening the application, it can be seen that it consists of 5 tabs (in red), the order of which is consistent with the order of functions required to produce and compare deconvolution results.

The first tab ("Import Image") includes the function of inserting the specimen we want to investigate (in orange), importing a focused specimen if necessary (in green) and editing the background, where it attempts to lower the values background intensities and background noise (in blue) as shown below.

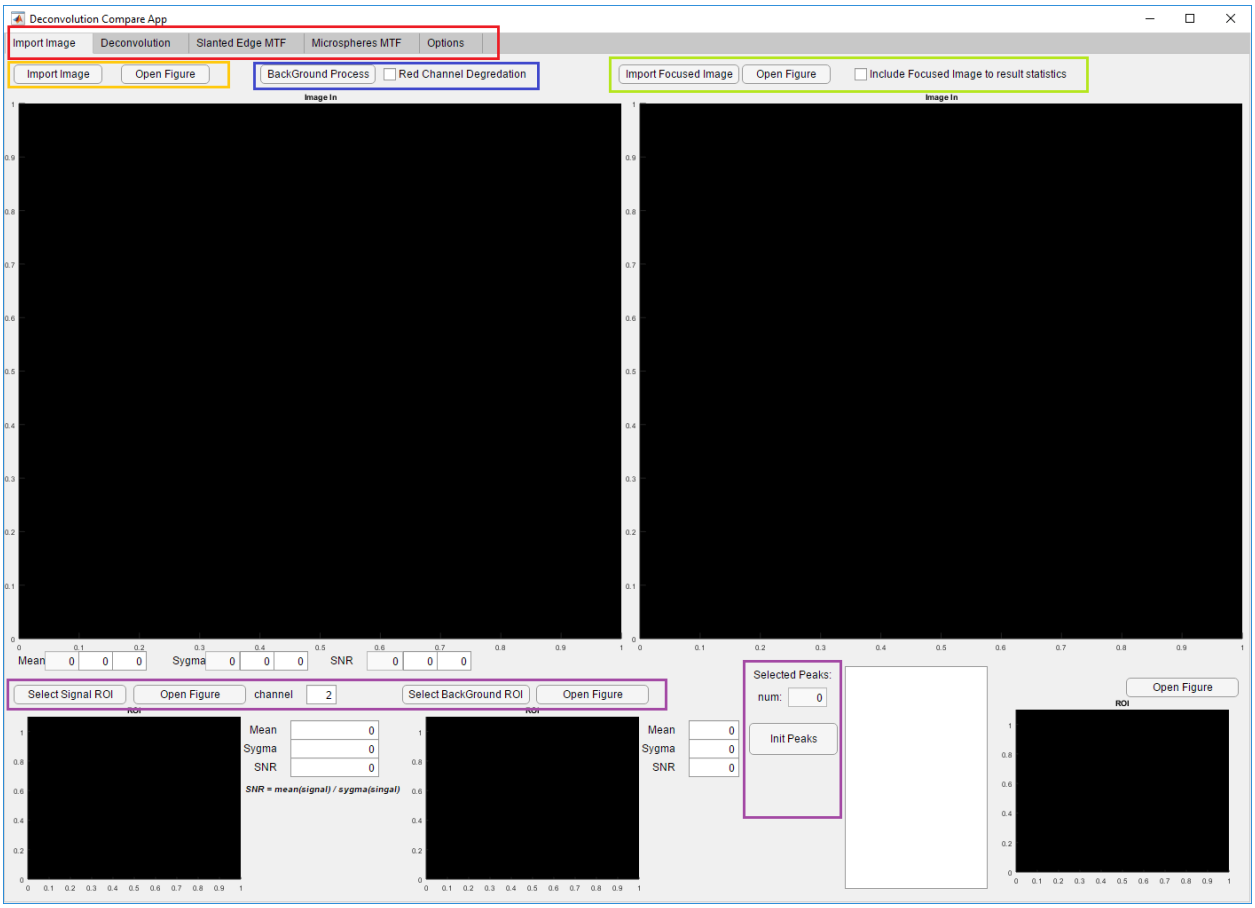

Figure 5.1: Application GUI - start page

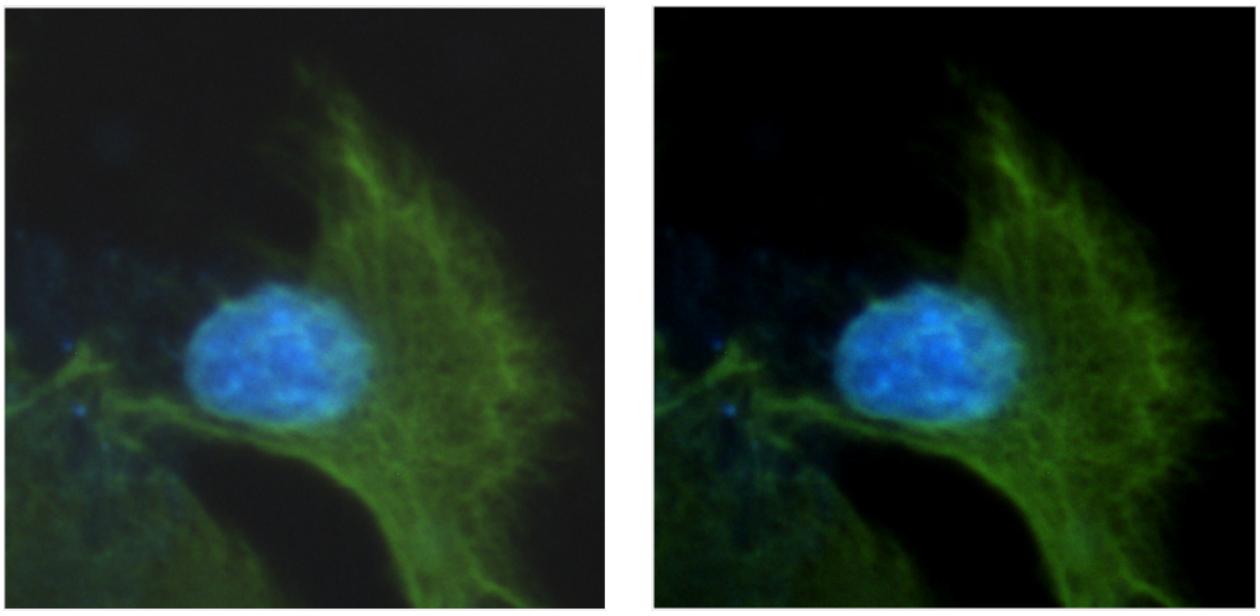

(a) original (b) processed

Figure 5.1: An example of background processing

If we want to create a comparison of results that contains a final algorithm ranking from the Peak Comparison Method, we can initialize the parameters of this method from the bottom of this screen (in purple color). Starting from left to right, we have the option to manually select the signal area, the background area, the peaks to be examined, and at the same time we can see their profiles as shown below. In the yellow selected areas, for example, we see how to manually select a signal and how that profile appears on the chart.

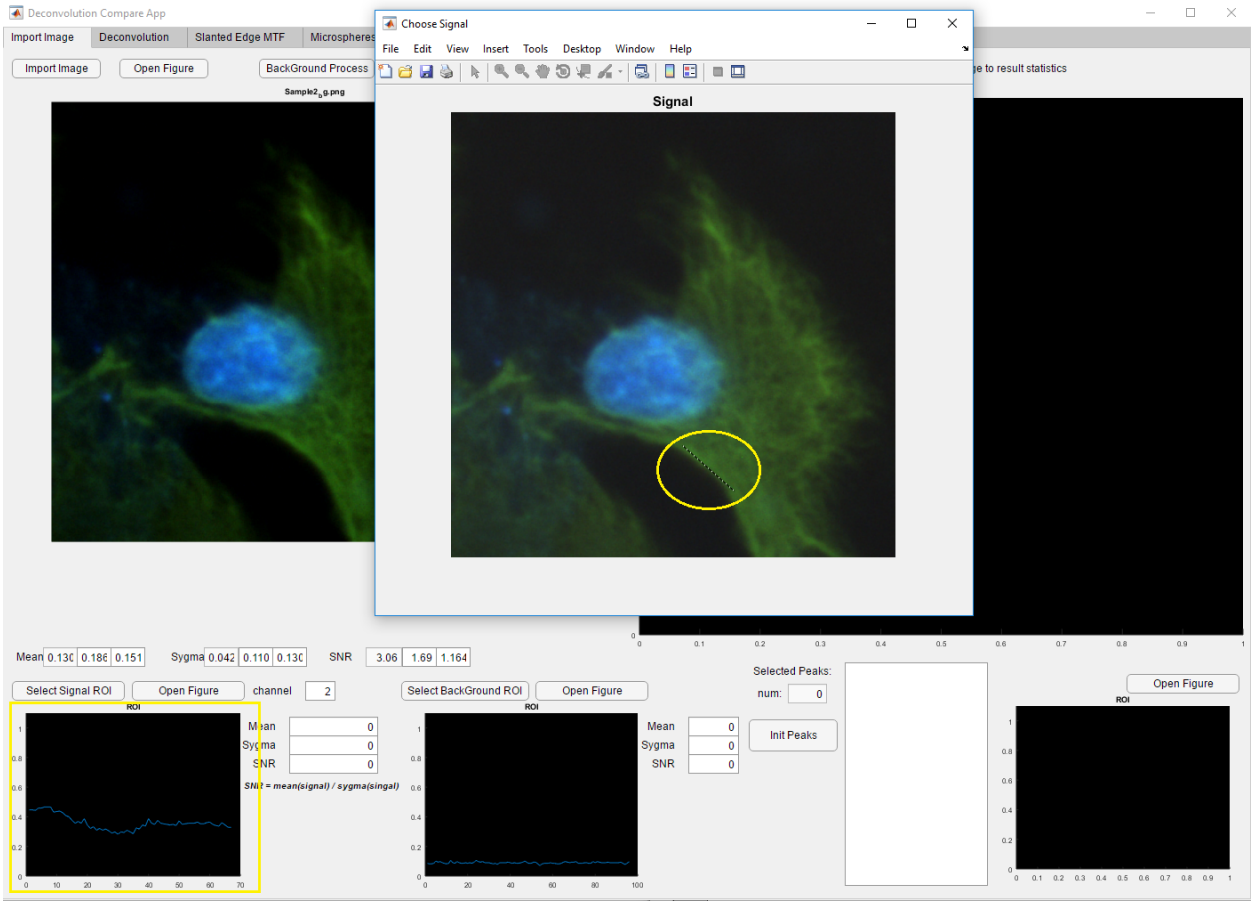

Figure 5.2: Application GUI - signal selection

The following tab ("Deconvolution") includes a variety of options related to the deconvolution process and the production of reference and ranking results.

At the top there is a series of tabs with the names of the deconvolution algorithms (in red), and in the end two tabs, "Decovnolution All" and "Report" (in green). On the deconvolution algorithms tabs (in red) there is a basic structure where it is made so that it is easy to parameterize the algorithms and produce the results.

As we see on the left, in the blue contour area, there are the parameters of the algorithm that can be managed by the user, as well as the "Deconvolve" button, where the output process begins according to the existing parameters. In this area there is a choice of PSF to be used if the algorithm is configured with PSF, as shown for Richardson Lucy - Total Variation

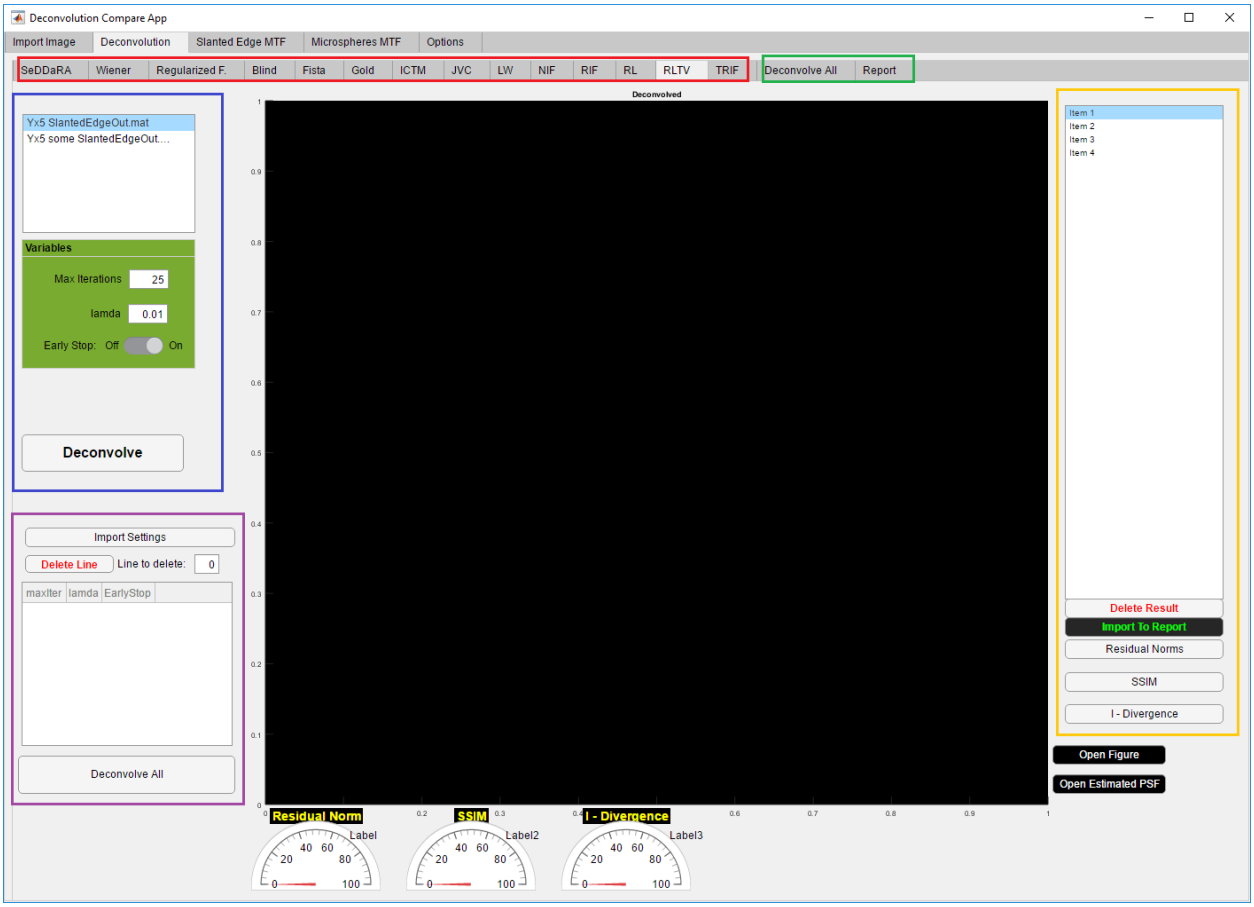

Figure 5.3: Application GUI - Deconvolution options example for RLTV algorithm

algorithm (RLTV). The choice of PSF can be multiple, so the program will produce results for each PSF.

In the bottom-right area with a purple contour, there is an initialization parameter storage table for massive output. The user can enter as many initializations of the algorithm as he wants and then produce all the results together. This function is very useful, first, to save time, due to automation, and the necessity of user existence, to produce each result separately, and secondly, it helps to organize and make easier the comparison of the results produced. Simply, we select the parameters we want from the blue border, and then click on the "Import Settings" button to create and save all the parameters in the table. It is also possible to delete an entry, as well as edit the entries directly on the table. Finally, the "Deconvolve All" button starts the automated output process.

Continuing to the right, in the area with the orange outline, we look at the top of the list of results, from where we can select one of them if we want to appear in the central box. When selecting the result, I-Divergence, SSIM, Residual Norms are displayed at the bottom of the screen in the form of a conter. We can also delete the selected result with the "Delete Result" button. If we want the result to be included in the final report, then we press the

"Import to Report" button, which copies it to the report mode on the Report tab. Finally, you can choose to display the statistics of all the results of each algorithm by pressing the corresponding buttons ("Residual Norm", "SSIM", "I-Divergence").

The penultimate tab, "Deconvolve All", contains functions of mass production of deconvolution results and production and export of reports and ranking list. There are check boxes for each algorithm we want to include. There is a separate option to create a reference folder for the "Deconvolve All" button and the "Deconvolve" button. In the case of choosing to create a reference folder, then a folder containing all the necessary files associated with this research (example original image, algorithm results, comparison statistics, ranking list, and much more) is created. It is also possible to set a prefix for the folder name if two or more different searches are required for the same sample. The different prefix will result in the creation of a reference folder and output of results.

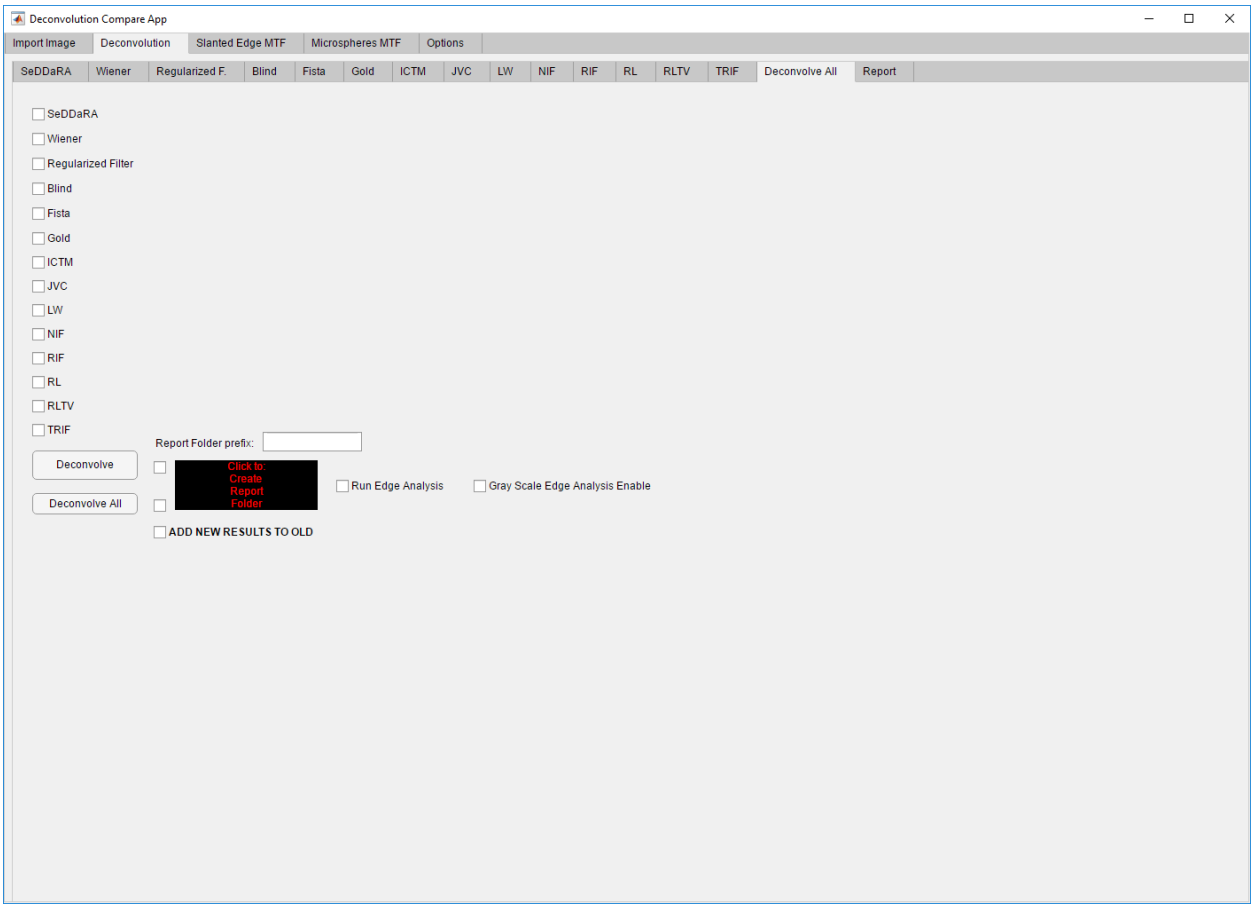

Figure 5.4: Application GUI - Deconvolve All Tab Functionality

Also, if we want to extract a list of algorithms, then select "Run Peak Analysis". There is also the ability to create a ranking list from a single-channel image analysis where it converts the sample and results into a gray scale automatically. Finally, if mass deconvolution has been performed with one of the two buttons, but we want to add more results in a second time, then select the "ADD NEW RESULTS TO OLD" button and start the Deconvolution

process again.

The last "Report" tab is a combination of the "Deconvolve All" tab and the algorithm tabs. In fact, the results transferred with the "Import to Report" button from the algorithm tabs on this tab now appear all together, and it is possible to create comparison and ranking lists as in the previous tab (button " Extract_Report "). It is also possible to store the data of the record as a reference ("Save_Report" button) if data is to be rechecked in a second and not only time, or if additional result is needed and a new list of rankings and a total report are generated.

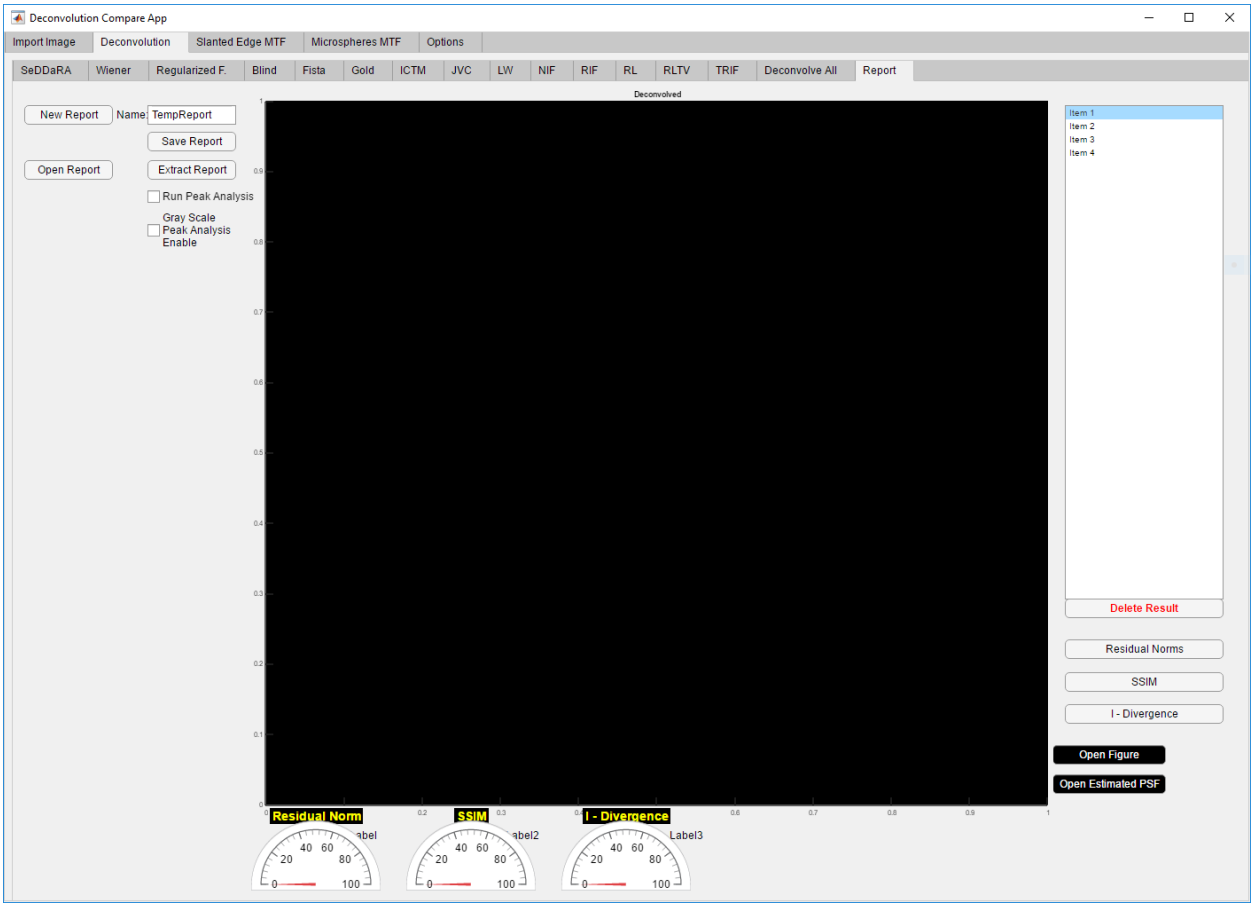

Figure 5.5: Application GUI - Report Manager Tab Functionality

The "Slanted Edge MTF" tab incorporates the PSF output function with the Slanted Edge method. Initially (in red), the user enters the sample with the "Import Slanted Edge Image" button. Then (in green), select the area of interest ("Select ROI" button). Finally (in blue), the capture parameters (pixel size and magnification) belonging to the inserted sample must be adjusted correctly before starting the PSF calculation ("Estimate PSF" button). The calculated PSF and MTF can be displayed in three-dimensional form using the corresponding buttons (in yellow) as shown below.

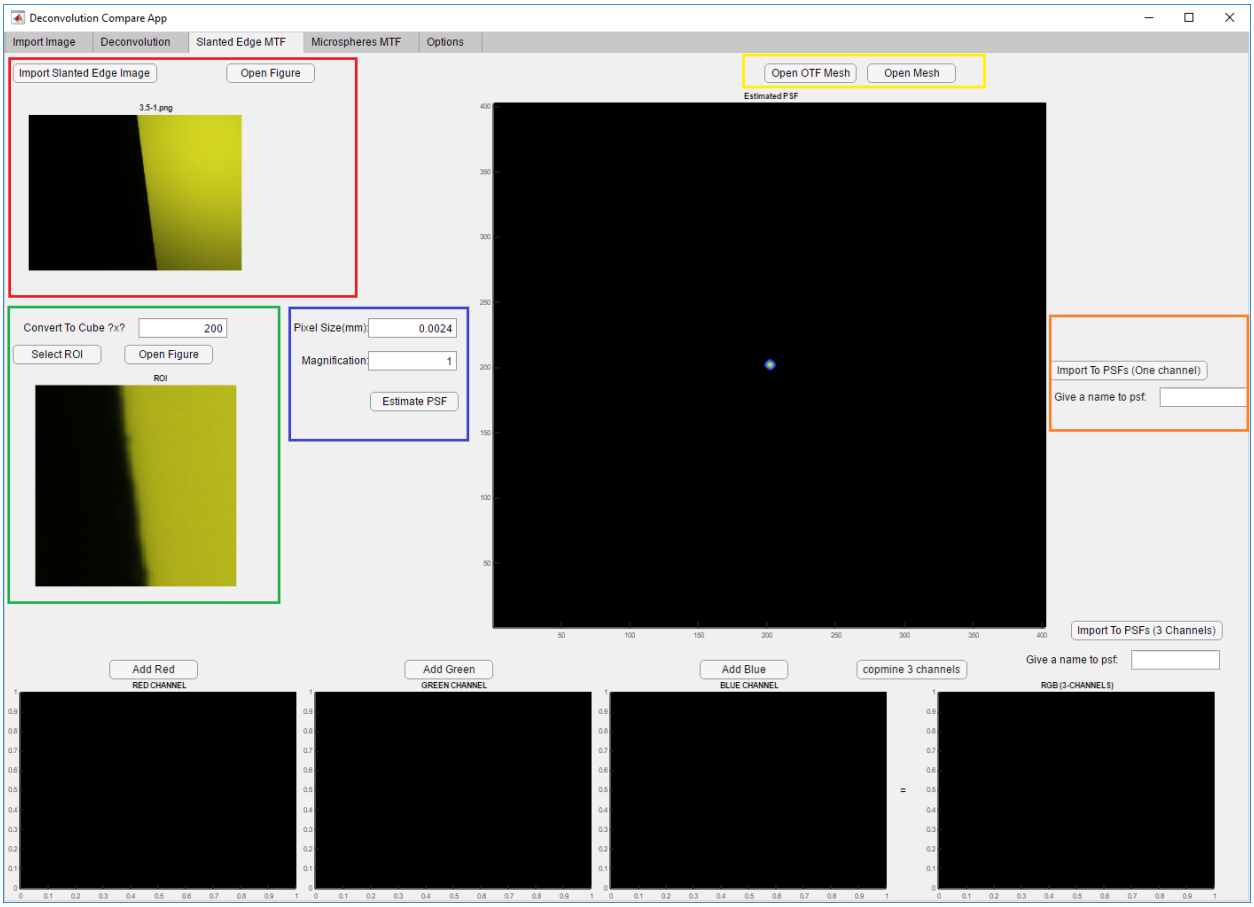

Figure 5.6: Application GUI - Slanted Edge Tab Functionality (PSF Extraction)

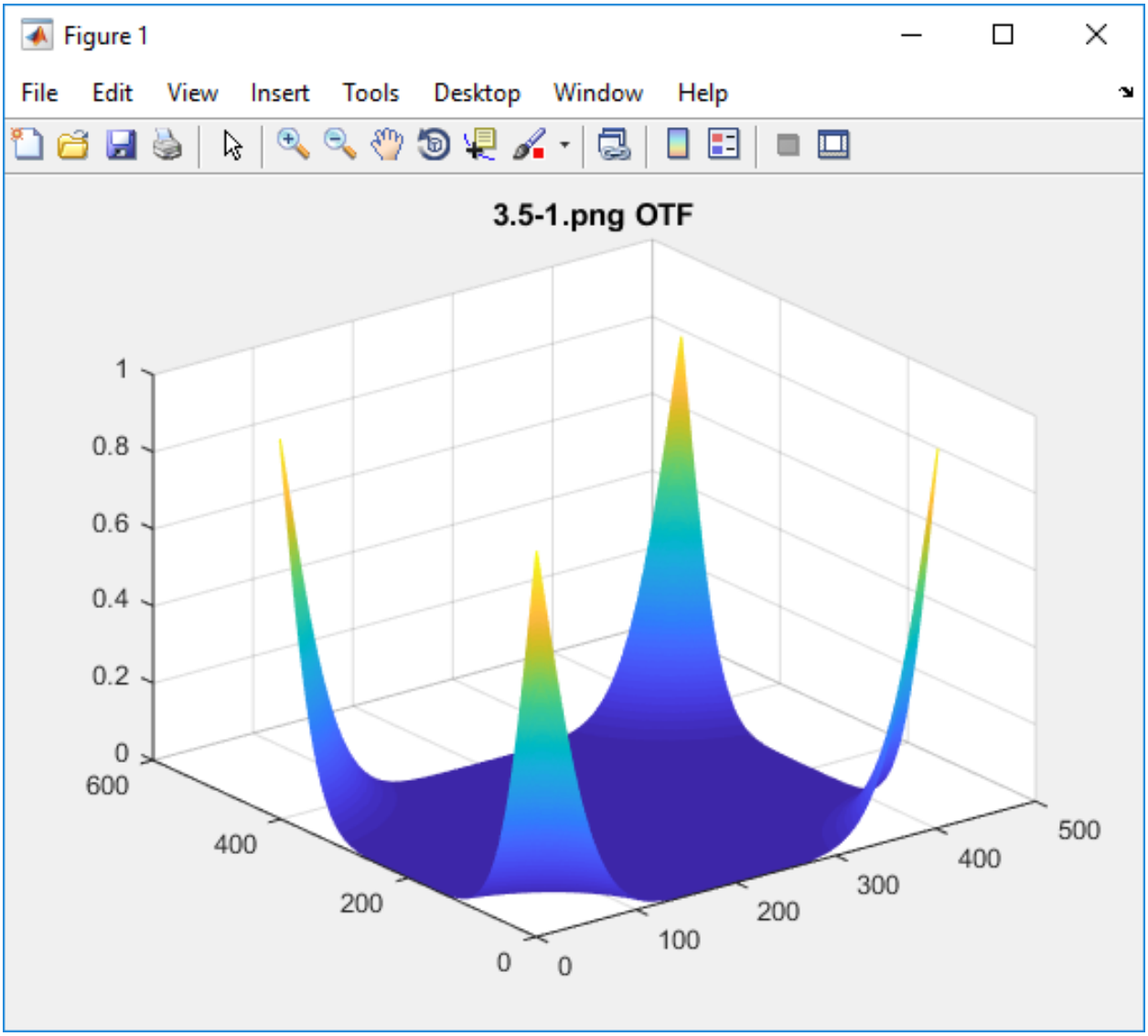

Figure 5.7: Application GUI - Slanted Edge tab showing otf example

Once the PSF has been calculated, the deconvolution algorithms can be entered in the lists to be used, by writing the desired name and by pressing the "Import To PSFs (One channel)" button. As additional functionality, the ability to create three-channel PSF (red, green, blue) has been added to take place at the bottom of the screen. Each add button ("AddRed", "AddGreen", "AddBlue") adds the already calculated PSF of a channel shown in the central box.

5.2 Code Implementation

The code of the above-mentioned application consists of a file system that follows a strict structure.

In the application folder are the following files with the following properties:

1. "DeconvolutionCompare.mlapp" (file): The file where the application opens
2. "DirectoryOrganisation.m" (file): a class that is responsible for managing the file system
3. "_Deconvolution Algorithms" (folder): Folder with the kernels of the Deconvolution algorithms
    - Naive Inverse Filters (NIFs), RIFs, Tikhonov Regularized Inverse Filters (TRIFs), GOLD, JVCs, LW, ICTM, FISTA and SeDDaRA algorithms are implemented by the transfer of the formulae that give the particular image estimates (Subsec. 2.4.2) into MATLAB code. The corresponding files are namesake (except SeDDaRA with file "deconvSeDDaRA_var.m") and have the suffix "_var.m"
    - For the RL, Wiener, Regularized and Blind Deconvolution algorithms, their implementations of the Image Processing Toolbox of MATLAB are used (deconvrl, deconvwnr and deconvblind respectively). RL and Blind Deconvolution are modified only for integrating residual norm computation and early stopping criterion. These algorithms are located in "rl_var.m", "deconvWiener_var.m", "deconvRegularized_var.m" and "deconv_blind_var.m" files respectively.
    - For the RLTV algorithm, the Total Variation factor is "attached" to the RL result in each iteration. It is located in "rltv_var.m" file.
4. "_Utils" (folder): a folder with all the necessary tools for the program
    - "EdgeAnalysisUtils" (folder) :
        - "DeconvolutionResultEdgeAnalysis.m" (file) : matlab classdef, which contains all functions that are responsible for the results peak comparison method and final ranking export.
        - EdgeAnalysisData.m (file) : matlab classdef. Auxiliary file for "DeconvolutionResultEdgeAnalysis.m", with data management functions.
    - "FluerescentBeadsUtils" (folder) :
        - "MicrosphereToMtfPsfHandler.m" (file) : matlab classdef, responsible for mtf-psf extraction with Fluerescent Beads method
    - "MtfExtractionUtils" (folder) :
        - "SlantedEdgeToMtfPsfHandler.m" (file) : matlab classdef, responsible for mtf-psf extraction with Slanted Edge method
    - "Parsers" (folder) : this folder has data parsers and extra functions that are used in deconvolution algorithms funstions entries.
    - "ProgramStateUtils" (folder) :
        - "DeconvolutionReportHandler.m" (file) : matlab classdef, which manages the report creation and extaction

  - "DeconvolutionResultStore.m" (file) : matlab classdef, each object keeps and manage data from one deconvolution result (images, paths ect)
  - "DeconvolutionStore.m" (file) : matlab classdef, data manager. Each object represents and manages the results collection of a deconvolution algorithm
- "DeconvolutionCaller.m" (file) : matlab classdef, responsible for data entries preperation. Collect users selections and parse them to the right forms. Finally call the right deconvolution algorithm/function.
- "deconvolutionWalk.m" (file) : matlab function. Gets collection of initialization variables and psfs, and run deconvolution algorithm for all combinations.
- "PsfHandler.m" (file) : matlab classdef, manages psfs (read/write) data.
- "OtherUtils" (folder) : this folder contains extra functionality

5. "Samples" (folder): folder where the samples to be examined exist
6. "Results" (folder): folder that stores all the results from deconvolution
7. "Reports" (folder): Output folder, all reports and related files
8. "_PSFs" (folder): folder that stores all PSFs calculated by the Slanted Edge method and used by the program for deconvolution
9. "_1.ProgramState" (folder): folder that stores files related to creating reports. main use of the "Report" tab of the program.

Chapter 6

Experiment And Results

6.1 Preparation

For this test, two images were used, from a fluorescence microscope. The first is a Slanted Edge sample and the other one is a sample of cells. The microscope set to the maximum magnification which is x21,9. Images are RGB, size 3096x2080, and taken with 10 second exposure. The Slanted Edge sample is converted to gray scale, and PSFs is extracted from it. It is also possible to manufacture three-dimensional PSFs using different wavelength samples, combining them into an RGB-PSF result. The capture information is:

[ZWO ASI178MC]
Pan=0
Tilt=0
Output Format=PNG files (*.png)
Binning=1
Capture Area=3096x2080
Colour Space=RGB24
Temperature=34,1
Hardware Binning=Off
High Speed Mode=On
Turbo USB=60(Auto)
Flip=Both
Frame Rate Limit=Maximum
Gain=55
Exposure=10
Timestamp Frames=Off
White Bal (B)=86
White Bal (R)=70
Brightness=0
Auto Exp Max Gain=255
Auto Exp Max Exp M S=30000
Auto Exp Target Brightness=100

Mono Bin=Off
Apply Flat=None
Subtract Dark=None
#Black Point
Display Black Point=0
#MidTone Point
Display MidTone Point=0,5
#White Point
Display White Point=1
TimeStamp=2018-05-17T13:01:50.1220601Z
SharpCapVersion=3.1.5059.0

The experimental process aims to produce results of comparing and classifying algorithms according to the characteristics of interest, such as the level of deblur, noise etc, as described in 4.5.

6.2 Process

Beginning with the image of the sample, manually selected five (5) of sharp profile and distinct peak intensities, that measurements be done without problems. In the event that other marks surround the area of a peak, the correctness of the results may be affected. Then, manually, a signal profile and a background profile are also selected. The options are also easily confirmed by viewing profiles in the corresponding windows of the Import Image tab in the application.

Then, on the Deconvolution tab, the algorithm options are set as shown below:

Wiener:	NSR = 0.001		
RIF:	lambda = 0.01		
TRIF:	lambda = 0.01		
LW:	iterations = 15	gamma = 1.7	
ICTM:	iterations = 25	gamma = 1	lambda = 0.01
GOLD:	iterations = 25		
JVC:	iterations = 25		
RL:	iterations = 25		
RLTV:	iterations = 25	lambda = 0.01	
FISTA:	iterations = 40	gamma = 1	lambda = 0.001
	wavelet: symlet2	decomposition levels = 3	
BLIND:	psfSsize : 11		
SEDDARA:	filter type: average	filter size = 148	filter sygma = 74
	Alpha = 0.01	alpha scalar: enable	alpha mean correction: enable
	noise estimation: enable		

* Those algorithms that are susceptible to early stop, the option was enabled.

Then, on the Slanted Edge MTF tab, the Slanted Edge sample is selected and a ROI is selected which is a 200x200 pixels square centered on the edge so that the amount of pixels at low intensity is approximately the same as the percentage of pixels with high intensity. The pixel size is 0.0024mm and the magnification is the maximum x21.9. Then, with the Estimate PSF and Import to PSFs buttons, the computed PSF is calculated and entered into the table of algorithms that accept PSF in their parameters. Then we define the PSF algorithms we just entered by selecting it from each table.

On the "Deconvolve All" tab, select all the algorithms from the list to enter their results in the final report, select the "Click to create report folder" checkbox to create a new folder with the completed report and the checkbox "Run peak analysis" to calculate and extract the comparison results of the algorithms in the report. Finally, press the "Deconvolve" button and wait for the entire process to be completed by monitoring its progress from the corresponding progress bars that appear.

6.3 Results Organization

At the end of the process, the folder "Reports" displays a folder with the corresponding prefix (if provided) and the name of the original image being studied in that report. Included in this folder are all necessary and produced records and results related to this report as shown below:

1. The original image
2. Images-results of deconvolutions
3. "Deconvolution Statistics Table From Original Image.txt" file with detailed measurements of I-Divergences, SSIMs and Residual Norms for each channel (RGB).
4. * .png files with the corresponding charts (for I-Divergence, SSIM and Residual Norm)
5. A PeakAnalysis folder that includes the Peak Analysis records and results as shown below:
   (a) "Channel" _CreatedPeakAnalysisStats.txt where it has the necessary measurements to produce the final score of each result (formula)
   (b) "Channel" _CreatedOneMeasureAnalysisStats.txt, a simpler form of comparison results based only on a profile peak
   (c) "Channel" _FWHM_TABLE.txt where all FWHMs are included for each selected peak
   (d) "Channel" _FWHM_SCORES_TABLE.txt where all FWHM_SCORES for each peak are included
   (e) "Channel" _SNR_ "algorithm used" .png, image files that together show the signal and background profiles on a chart for additional comparison

(f) FinalGeneralRankingTable.txt the final ranking tables

All .txt files can be copied to a spreadsheet with a column separator (",") for further processing and presentation.

The final ranking according to the procedure described in 4.5 and the one that we are interested in is in the file "FinalGeneralRankingTable.txt". Only the final Scores of deconvolved images for all channels are included, as well as two types of ranking one that summarizes "Histogram_Score" and one without it. The following are the images and the ranking tables according to which the comparison of the results is assumed.

6.4 Results View

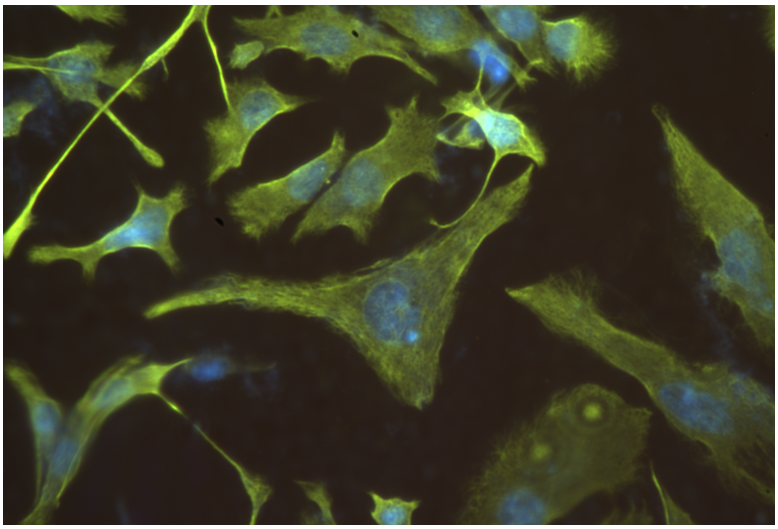

Figure 6.1: The original sample image.

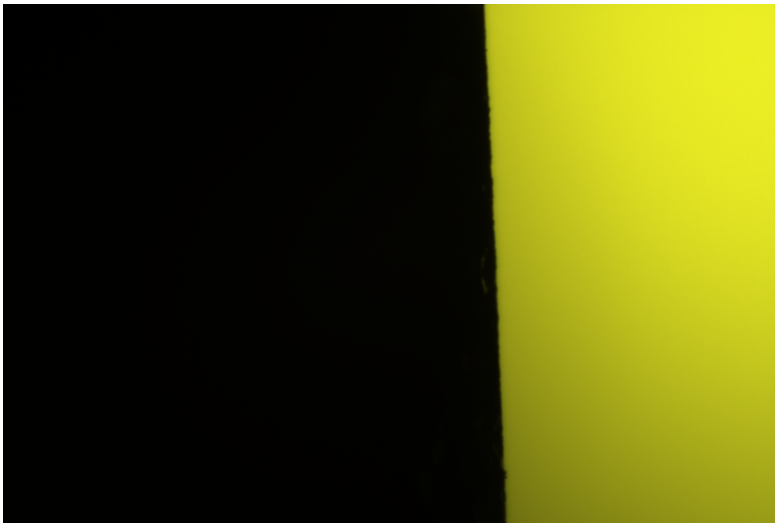

Figure 6.2: The slanted edge sample image.

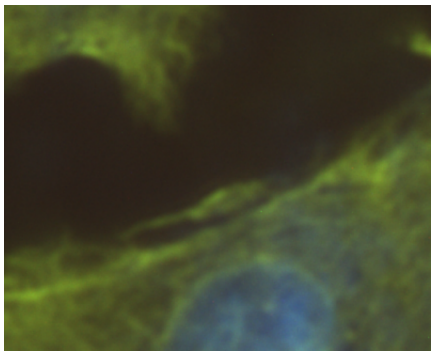

(a) Original sample image.

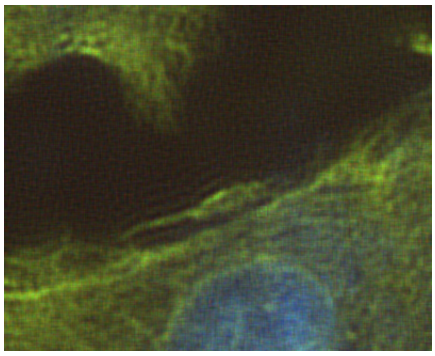

(b) Blind

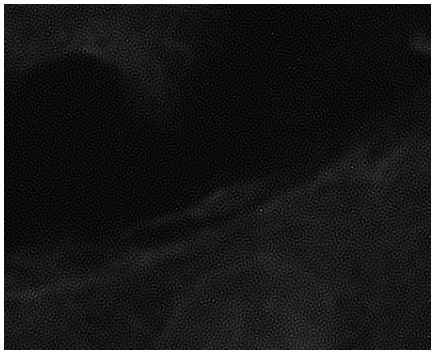

(c) Regularized filter

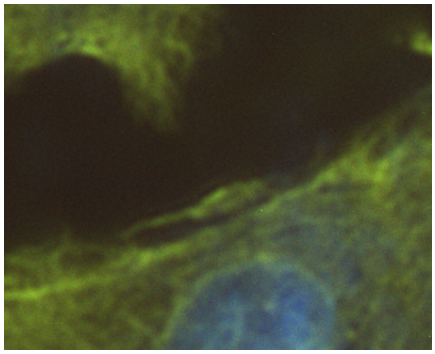

(d) SeDDaRA

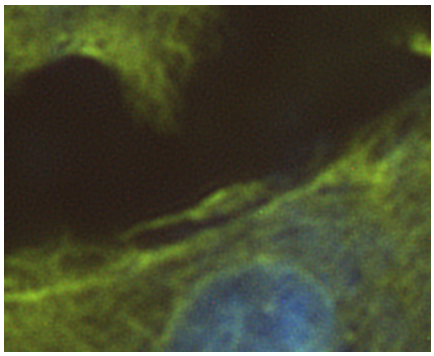

(e) Wiener

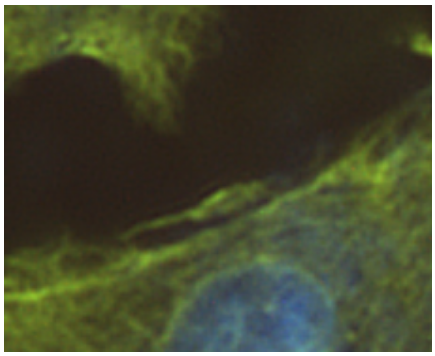

(f) Fista

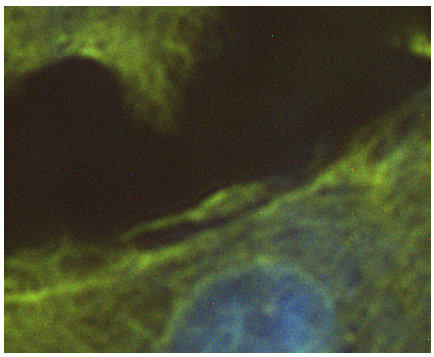

(g) Gold

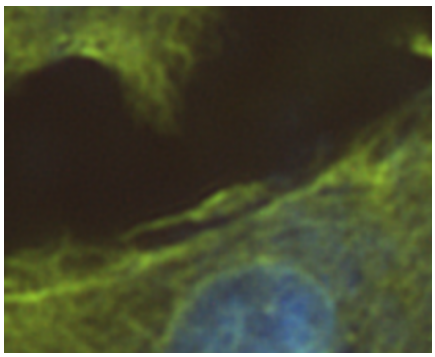

(h) ICTM

Figure 6.3: Deconvolution image results (part 1)

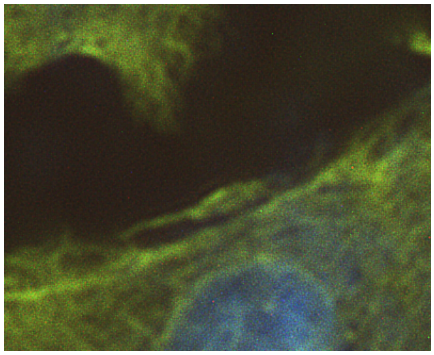

(i) JVC

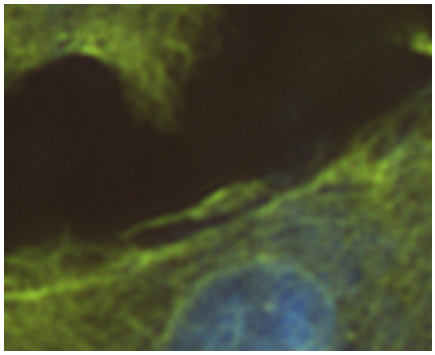

(j) LW

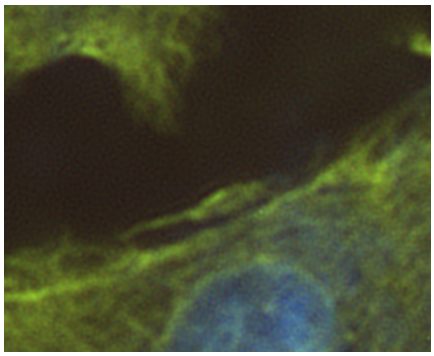

(k) RIF filter

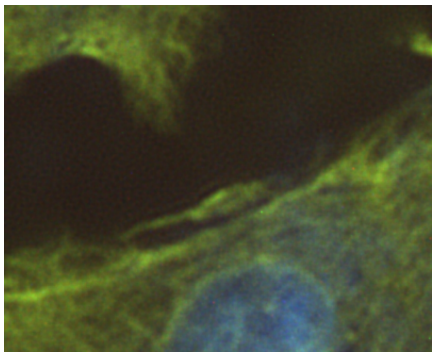

(l) RL

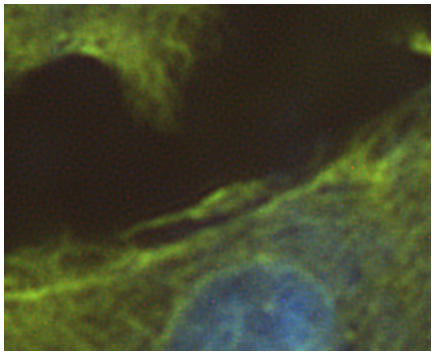

(m) RLTV

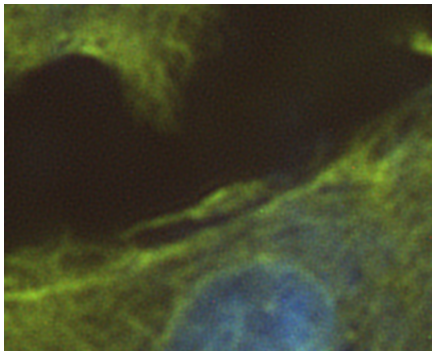

(n) TRIF

Figure 6.3: Deconvolution image results (part 2)

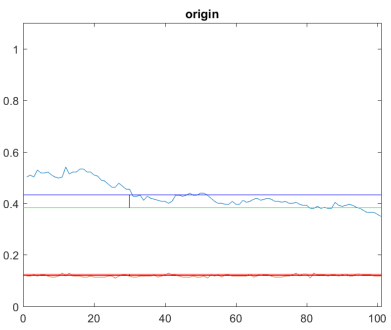

(a) original image.

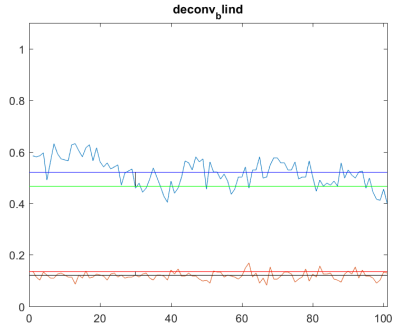

(b) Blind

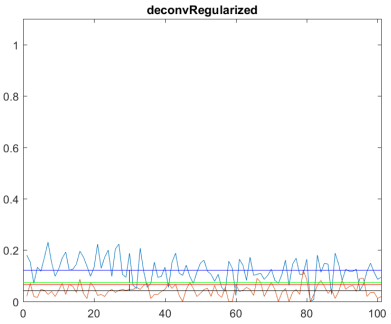

(c) Regularized filter

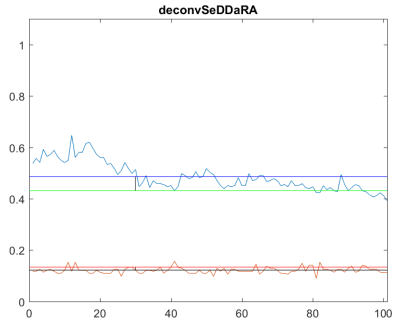

(d) SeDDaRA

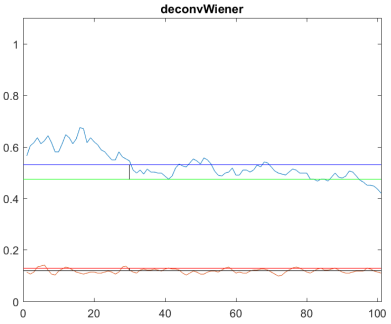

(e) Wiener

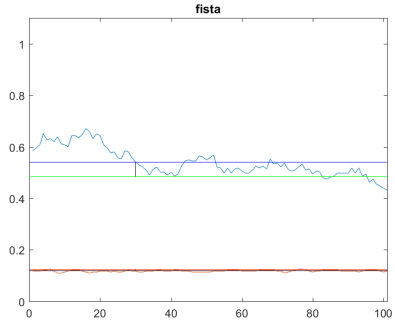

(f) Fista

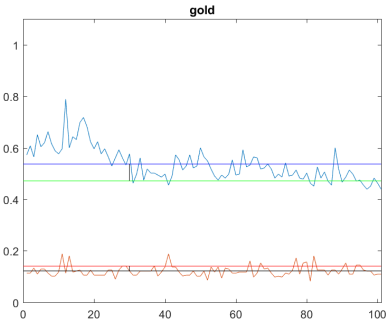

(g) Gold

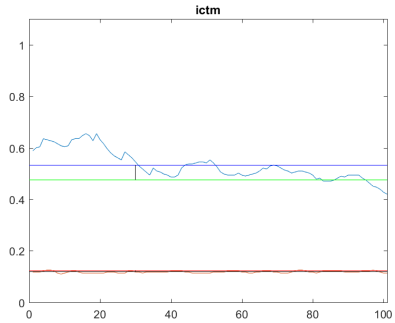

(h) ICTM

Figure 6.4: Deconvolution results SNR Score estimation (part 1)

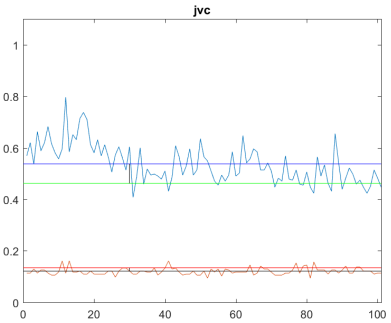

(i) JVC

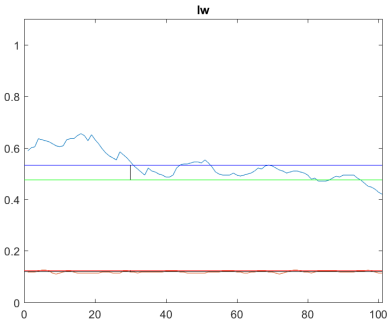

(j) LW

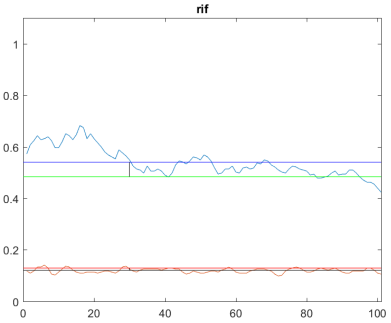

(k) RIF filter

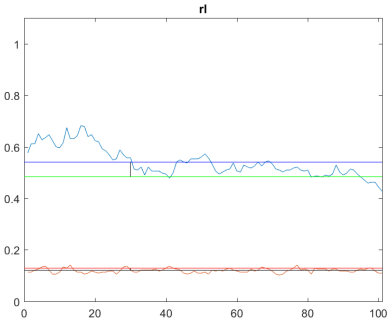

(l) RL

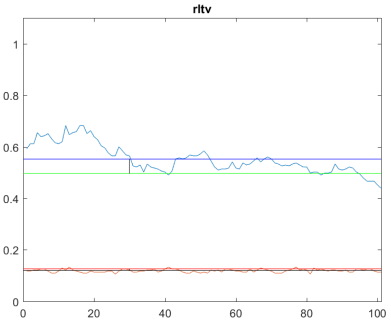

(m) RLTV

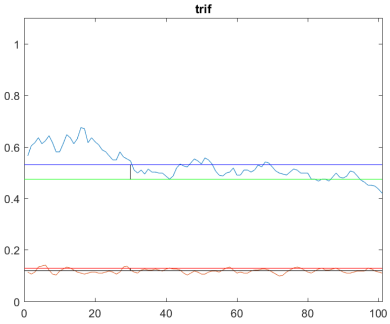

(n) TRIF

Figure 6.4: Deconvolution results SNR Score estimation (part 2)

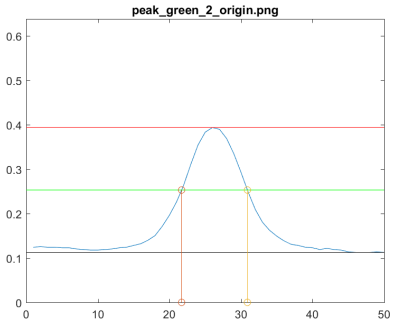

(a) original image.

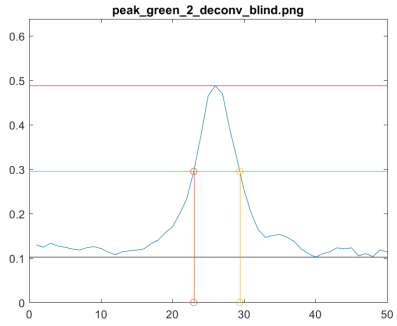

(b) Blind

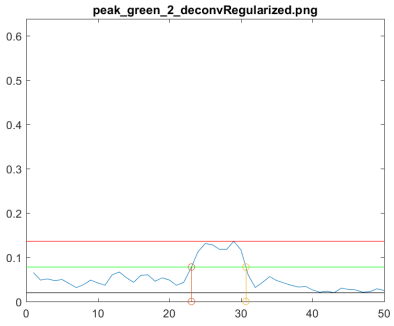

(c) Regularized filter

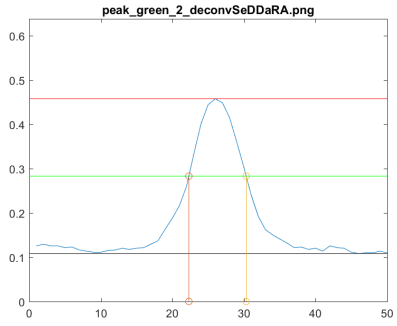

(d) SeDDaRA

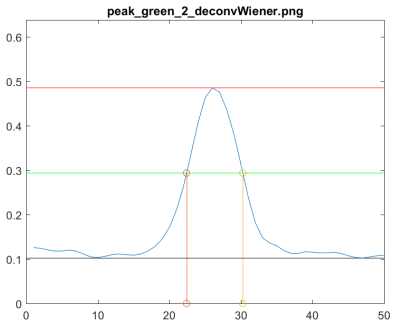

(e) Wiener

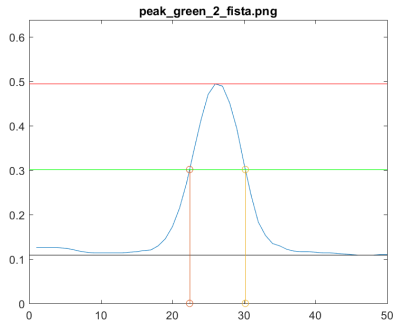

(f) Fista

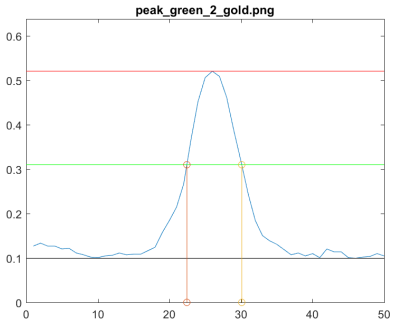

(g) Gold

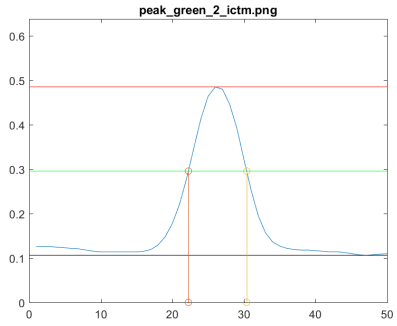

(h) ICTM

Figure 6.5: Deconvolution results peak profiles (part 1)

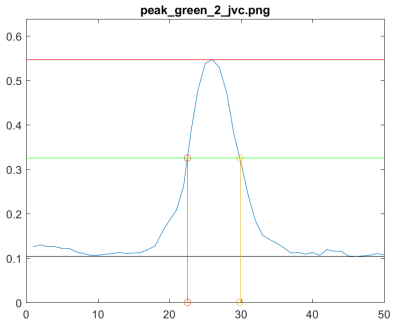

(i) JVC

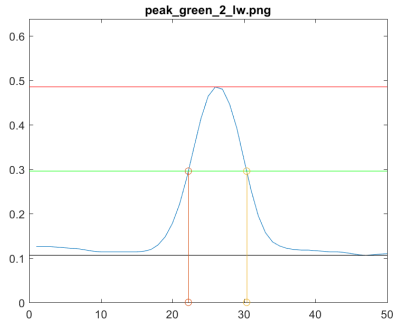

(j) LW

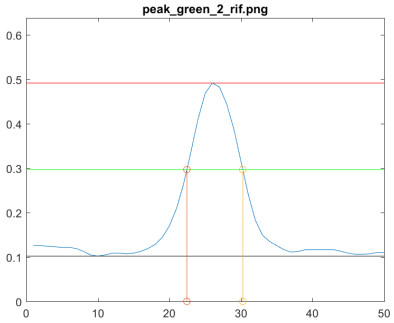

(k) RIF filter

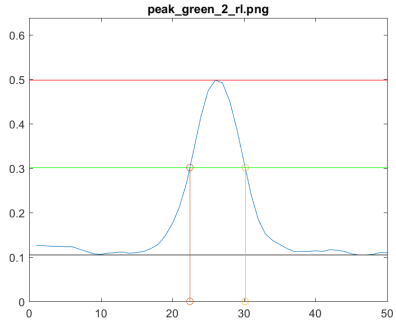

(l) RL

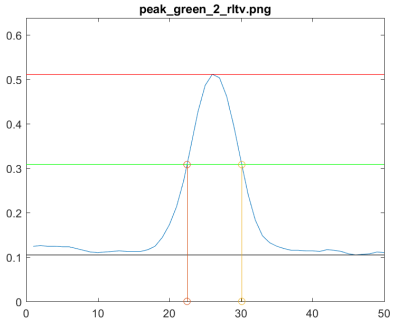

(m) RLTV

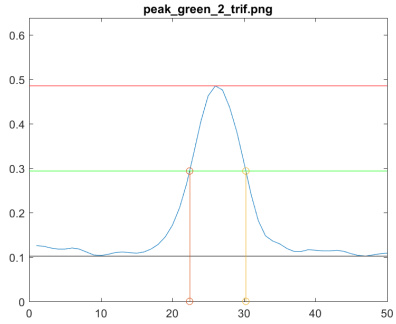

(n) TRIF

Figure 6.5: Deconvolution results peak profiles (part 2)

Algorithm	fwhmValues_1	fwhmValues_2	fwhmValues_3	fwhmValues_4	fwhmValues_5	FWHM_Mean
origin	*8.73*	*9.19*	*8.88*	*8.54*	*10.18*	*9.1*
deconv_blind	6.72	6.43	6.29	5.89	8.04	6.67
rltv	6.96	7.65	7.12	6.93	8.09	7.35
jvc	6.35	7.32	7.69	7.2	8.47	7.4
rl	7.08	7.72	7.36	7.1	8.35	7.52
fista	7.25	7.78	7.22	7.06	8.32	7.53
gold	6.86	7.67	7.68	7.25	8.6	7.61
rif	7.34	7.81	7.38	7.17	8.36	7.61
deconvWiener	7.47	7.86	7.46	7.24	8.46	7.7
trif	7.47	7.86	7.46	7.24	8.46	7.7
ictm	7.57	8.15	7.53	7.36	8.61	7.84
lw	7.57	8.15	7.53	7.36	8.61	7.84
deconvSeDDaRA	7.37	8.01	8.01	7.47	9.09	7.99
deconvRegularized	21.94	7.6	34.57	16.32	5.44	17.17

Figure 6.6: Full Width at Half Maximum Table for chosen peaks

Algorithm	Peak_Score_1	Peak_Score_2	Peak_Score_3	Peak_Score_4	Peak_Score_5	Peak_Score_Mean
origin	*0.02*	*0.03*	*0.03*	*0.04*	*0.04*	*0.03*
deconv_blind	0.04	0.06	0.06	0.08	0.06	0.06
jvc	0.06	0.06	0.05	0.07	0.06	0.06
rltv	0.04	0.05	0.06	0.07	0.06	0.06
gold	0.05	0.05	0.05	0.06	0.06	0.06
rl	0.04	0.05	0.05	0.06	0.06	0.05
rif	0.04	0.05	0.05	0.06	0.06	0.05
fista	0.04	0.05	0.05	0.06	0.06	0.05
deconvWiener	0.04	0.05	0.05	0.06	0.06	0.05
trif	0.04	0.05	0.05	0.06	0.06	0.05
ictm	0.04	0.05	0.05	0.06	0.06	0.05
lw	0.04	0.05	0.05	0.06	0.06	0.05
deconvSeDDaRA	0.04	0.04	0.04	0.05	0.05	0.04
deconvRegularized	0	0.02	0	0.01	0.03	0.01

Figure 6.7: Peak Scores for chosen peaks

Algorithm	Peak_Score_Mean	FWHM_Mean	Signal_Mean	Signal_Std	Background_Mean	Background_Std	Signal_Score	Bckgrnd_Score	Snr_Score	Histogram_Std	Final Score
origin	0.03	9.1	0.43	0.05	0.12	0	0.38	0.12	4.73	70066.13	10601.34
fista	0.05	7.53	0.54	0.06	0.12	0	0.48	0.12	6.07	74615.68	24285.22
rltv	0.06	7.35	0.55	0.06	0.12	0.01	0.5	0.13	5.97	70614.12	24111.24
lw	0.05	7.84	0.53	0.06	0.12	0	0.48	0.12	5.77	74485.58	21583.96
ictm	0.05	7.84	0.53	0.06	0.12	0	0.48	0.12	5.77	74492.13	21572.77
rl	0.05	7.52	0.54	0.06	0.12	0.01	0.48	0.13	5.49	66779.85	19926.83
rif	0.05	7.61	0.54	0.06	0.12	0.01	0.48	0.13	5.47	65736.61	19271.58
deconvWiener	0.05	7.7	0.53	0.06	0.12	0.01	0.47	0.13	5.28	65328.97	17887.37
trif	0.05	7.7	0.53	0.06	0.12	0.01	0.47	0.13	5.28	65328.97	17887.37
deconv_blind	0.06	6.67	0.52	0.05	0.12	0.01	0.47	0.13	4.77	54284.09	15885.87
jvc	0.06	7.4	0.54	0.08	0.12	0.01	0.46	0.13	3.69	60891.94	12943.75
deconvSeDDaRA	0.04	7.99	0.49	0.05	0.12	0.01	0.43	0.13	4.51	60324.23	12089.62
gold	0.06	7.61	0.54	0.07	0.12	0.02	0.47	0.14	3.91	54548.95	11766.45
deconvRegularized	0.01	17.17	0.12	0.05	0.04	0.02	0.07	0.07	0.11	63751.53	79.87

Figure 6.8: Full Peak Analysis Table

Algorithm	Peak_Score	Snr_Score	Histogram_Score	Final_Score
fista	0.87	1	1	1
rltv	0.93	0.98	0.95	0.99
lw	0.82	0.95	1	0.89
ictm	0.82	0.95	1	0.89
rl	0.89	0.9	0.89	0.82
rif	0.88	0.9	0.88	0.79
deconvWiener	0.85	0.87	0.88	0.74
trif	0.85	0.87	0.88	0.74
deconv_blind	1	0.79	0.73	0.65
jvc	0.94	0.61	0.82	0.53
deconvSeDDaRA	0.73	0.74	0.81	0.5
gold	0.9	0.64	0.73	0.48
deconvRegularized	0.19	0.02	0.85	0

Table 6.1: Final Score Results Table

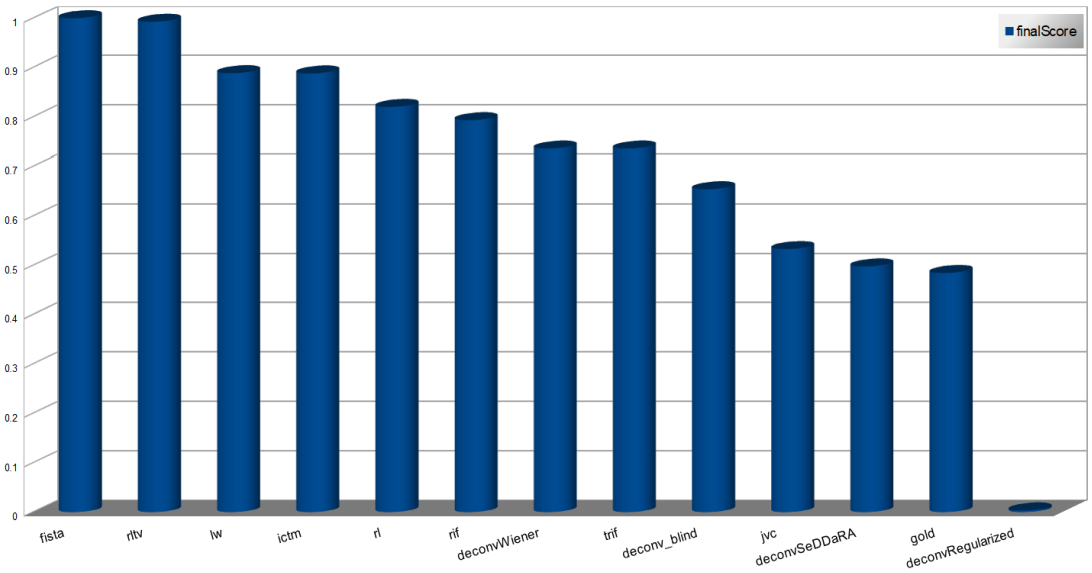

Figure 6.9: The final Scores diagram

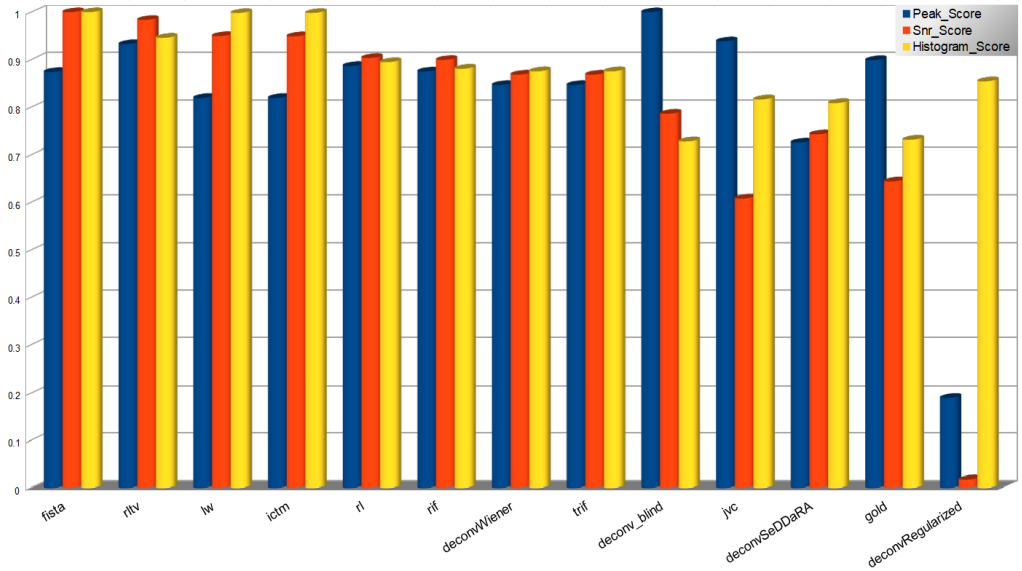

Figure 6.10: The final Scores Details Diagram

Chapter 7

Explanation Of Software Experiments Results

7.1 Conclusions

Qualitative assessment of microscopic images is a chapter that the scientific community has researched for many years. The differences and discrepancies in the eye's view with digital image measurements are a factor that makes this process more difficult and complicated. Each visual system has a different effect on capturing an image, and each algorithm treats its statistics differently. This has the effect of rendering virtually impossible the theoretical modeling of these systems, making their prediction and evaluation of the results impossible. Thus, there is a need to approach this problem from another direction by analyzing the requirements of the applications that serve these systems each time. So, drawing on the parameters of interest and finding ways to measure them, we constructed a method that can explain in numbers the degree of satisfaction of the human eye. In other words, the evaluation method developed in this diplomatic research attempts to answer the question of "which image is better than the other" according to eye view.

Based on an optical system, ie the microscope used and a series of deconvolution algorithms, we extracted results that show us the behavior of each algorithm in our samples. This measure of behavior is expressed in a number so that it is comparable and expresses the qualitative appearance of the results. Thus, looking at the final classification of the produced images, we can perceive and compare them in terms of noise, spatial analysis and universal opposition. We also have the ability to classify them according to one characteristic, and to evaluate the behavior of the algorithms with respect to the other features. For example, if we want to see which algorithm produced the best spatial resolution irrespective of the final noise.

7.2 FWHM and Peak_Score results

Starting from the table 7.1 showing the table of FWHMs extracted from our experiment, we notice that blind_deconvolution has the most acceptable spatial resolution. As explained

in section 4.4, the less FWHM the better spatial resolution we have. This means that the top selected is sharper than the rest. RLTV, JVC, RL, FISTA, GOLD, RIF, WIENER, TRIF, ICTM, LW, SeDDaRA, and Regularized are ranked as shown in the table. Seeing the Peak_Score table we see that best top score is achieved in a similar way. It is recalled that Peak_Score takes into account the FWHM and peak height (see 4.5.1). The resulting order for Peak_Score is as follows: blind_deconvolution, JVC, RLTV, GOLD, RL, RIF, FISTA, WIENER, TRIF, ICTM, LW, SeDDaRA and Regularized. The two ranking tables are listed below for easier comparison. The results are normalized to the largest of each column, because we are interested in the comparison between them and not the individual results. The result of the original image is included in the first line without being classified for comparison of the price difference.

Algorithm	FWHM Mean
origin	0.53
deconv_blind	0.39
rltv	0.43
jvc	0.43
rl	0.44
fista	0.44
gold	0.44
rif	0.44
deconvWiener	0.45
trif	0.45
ictm	0.46
lw	0.46
deconvSeDDaRA	0.47
deconvRegularized	1

Algorithm	Peak_Score Mean
origin	0.52
deconv_blind	1
jvc	0.94
rltv	0.93
gold	0.9
rl	0.89
rif	0.88
fista	0.87
deconvWiener	0.85
trif	0.85
ictm	0.82
lw	0.82
deconvSeDDaRA	0.73
deconvRegularized	0.19

Table 7.1: FWHM and Peak_Score Results Comparison

As we can see in the comparison of tables 7.1, the second place is claimed by RLTV with a slightly better FWHM than JVC, which eventually presents a better Peak_Score. This is because the maximum peak value with the RLTV algorithm is less than the maximum value of the same peak as JVC while having the same FWHM. So JVC has a better contrast. This actually serves the use of Peak_Score. Corresponding phenomena are also presented with the other algorithms, which eventually gain a more distinct position in the Peak_Score table.

7.3 Background(Noise)_Score, Signal_Score and SNR_Score

In order to understand the importance of SNR_Score, the results of Background_Score and Signal_Score should be explained. Background_Score is the sum of the average value of the background with the standard deviation. This practically means that the higher Background_Score value indicates either higher background values or higher standard deviation, or both. In any case, it entails a "worst quality" background than a lower Background_Score

image. Signal_Score is the difference in the mean value of the signal minus the standard deviation. This indicates that the larger Signal_Score implies either increased intensity values or lower standard deviation ie noise, or both. So larger Signal_Score equals "better quality" of the signal. Ultimately, what interests us is whether noise and image processing affect the quality of the signal and the noise and the noise tendency to weaken the distinction between signal and noise. So the *Signal_Score/Background_Score* ratio, SNR_Score, shows us the value of the "quality" of the contrast (noise-driven) compared to the other effects as well as the original image.

Algorithm	Bckgrnd_Score	Algorithm	Signal_Score	Algorithm	Snr_Score
origin	0.88	origin	0.77	origin	0.78
deconvRegularized	0.47	rltv	1	fista	1
fista	0.88	fista	0.98	rltv	0.98
ictm	0.88	rl	0.98	lw	0.95
lw	0.88	rif	0.97	ictm	0.95
rltv	0.89	lw	0.96	rl	0.9
deconvWiener	0.91	ictm	0.96	rif	0.9
trif	0.91	deconvWiener	0.95	deconvWiener	0.87
rl	0.91	trif	0.95	trif	0.87
rif	0.92	gold	0.95	deconv_blind	0.79
deconvSeDDaRA	0.95	deconv_blind	0.94	deconvSeDDaRA	0.74
jvc	0.95	jvc	0.93	gold	0.64
deconv_blind	0.96	deconvSeDDaRA	0.87	jvc	0.61
gold	1	deconvRegularized	0.15	deconvRegularized	0.02

Table 7.2: Background_Score, Signal_Score and SNR_Score Results Comparison

By looking at the results of our experiment in the table 7.2, we see that the better-less Background_Score has first the Regularized algorithm then FISTA, and in ascending order ICTM, LW, RLTV, TRIF, WIENER, RL, RIF, SeDDaRA, JVC , BLIND and GOLD. Unlike Background_Score, Regularized has the worst Signal_Score, this is confirmed by viewing the image produced by this algorithm. At Signal_Score we have the following ranking, with RLTV first, FISTA followed by RL, RIF, LW, ICTM, WIENER, TRIF, GOLD, BLIND, JVC, SeDDaRA and Regularized. So far there is no clear picture of how the result is processed by the processing of each algorithm for this answer gives the SNR_Score ranking where the higher value implies a better image.

7.4 Final_Score

By combining the above results with Histogram_Score where we are a general improvement of the universal image contrast we get the table Final_Score (table 6.1) where is the final proposition of the algorithms according to the desired result. This list tells us that an image with a higher value of Final_Score fits better to the general requirements of deconvolution processing than a picture with a lower value of Final_Score. Also, this ranking shows us

which image satisfies the "eye" better. That is, an image with a larger Final_Score has a relatively better definition than another with a smaller one. So the resulting final ranking is as follows. In the first place is the FISTA algorithm and almost the same rating, RLTV is second. The next two positions then go to LW and ICTM respectively. RL, RIF, WIENER, TRIF, BLIND, JVC, SeDDaRA, GOLD and Regularized algorithms are followed by a lower score and a descending order.

7.5 Conclusion

Finally, the proposed ranking of results expresses a more general success of algorithms in meeting the selected criteria set at the beginning of the experiment. However, more specialized information can be deduced for the behavior of these algorithms, if needed. For example, if we want to investigate more specifically which algorithm produces more focused results regardless of noise, or if we have a restriction on the maximum allowable noise limit or Background_Score, then we can look at the Peak_Score table and sort the results by flipping what do not meet the noise criterion.

Also in the same way it can be used to evaluate different PSFs, if they are produced by different methods, such as the various theoretical models or experimental MTF extraction models. This can be implemented by having a fixed algorithm as a fixed parameter and performing the experiment for many different PSFs. The program developed in this thesis supports this process, as well as selecting multiple PSFs and multiple algorithms at the same time, extracting the results for combining all options exhaustively. Thus, it can be investigated how each algorithm reacts to each PSF output method, displaying "success" correlations between deconvolution algorithms and PSF extraction methods for specific samples.

7.6 Discussion

It is known that the processing of the image as a field is not completely independent of the human factor, which means that the visual perception of images in many cases may contradict mathematical models, relationships or results in general. This vacuum attempts to cover this thesis, proposing a new way of correlating visual opacity with the mathematical assessment of the results. The initial results of this method seem to be usable as a compass for the automated rank and success rate of deconvolution results.

Due to the ability of this method to compare results on specific characteristics such as spatial analysis, noise effects and changes in the overall contrast of the image, it could play a catalytic role in the manufacture of both PSF extraction methods and building new improved deconvolution algorithms that can "be aware" of their effect on the image and accordingly adapt themselves to achieve the best possible results according to the needs of the user or purpose of their application. In the context of this idea and knowing that the method of this thesis depends on the human factor for the selection of background, signal and edge areas, we could suggest extending the method to automatic search for these domains so that

it can be used , as an independent and integrated method, either to be used singly or to be incorporated into new methods of deconvolution.

Finally, the characteristics examined and considered by the method developed were the basic features that were necessary for the characterization of specific microscope specimens used for this thesis. Correspondingly, other features and factors can be added in the future that will contribute to the production of even more targeted and integrated comparisons and rankings so that it can be universally established as the method of evaluation and assessment of deconvolution algorithms and not only.

Bibliography

[1] Full width at half maximum explained. https://www.noao.edu/image_gallery/text/fwhm.html.

[2] Introduction to modulation transfer function. https://www.edmundoptics.com/resources/application-notes/optics/introduction-to-modulation-transfer-function.

[3] Mtf - modulation transfer function. https://www.telescope-optics.net/mtf.htm.

[4] Residual sum of squares. https://en.wikipedia.org/wiki/Residual_sum_of_squares.

[5] Signal-to-noise ratio (imaging). https://en.wikipedia.org/wiki/Signal-to-noise_ratio_(imaging).

[6] Spatial resolution. http://www.medimaging.gr/cd/pages/par2.htm.

[7] *Comparison of reconstruction algorithms for images from sparse-aperture systems*, volume 4792, 2002.

[8] Explaining standard deviation. https://www.spcforexcel.com/knowledge/basic-statistics/explaining-standard-deviation, Aug 2015.

[9] Mortimer Abramowitz, Brian Herman, Douglas B. Murphy, and Michael W. Davidson. Anatomy of the fluorescence microscope. https://www.olympus-lifescience.com/en/microscope-resource/primer/techniques/fluorescence/anatomy/fluoromicroanatomy.

[10] Mortimer Abramowitz, Kenneth R. Spring, and Michael W. Davidson. Introduction to lenses and geometrical optics. https://www.olympus-lifescience.com/en/microscope-resource/primer/lightandcolor/lensesintro.

[11] Costas Balas. Advanced topics in electronic imaging - hpy 603 - lecture 7:microscopy basics. In *Lecture notes*, pages 2–8.

[12] Costas Balas. Transport phenomena - basic optics. In *Lecture notes*, pages 18–34.

[13] M. Born and E. Wolf. *Principles of Optics*, chapter 8.5, page 436–445. 7th edition, 2003.

[14] Peter D. Burns. Slanted-edge mtf for digital camera and scanner analysis. In *Proc. PICS Conf. , IS&T*, page 135, 2000.

[15] C C. Cunningham and D Anthony. Image deconvolution of extended objects: A comparison of the inverse fourier and the lucy techniques. *Icarus*, 102:307–315, 04 1993.

[16] James N. Caron, Nader M. Namazi, and Chris J. Rollins. Noniterative blind data restoration by use of an extracted filter function. *Appl. Opt.*, 41(32):6884–6889, Nov 2002.

[17] I. Csiszar. i-divergence geometry of probability distributions and minimization problems. *The Annals of Probability*, 3(3):146–158, 1975.

[18] Brian Herman, Victoria E. Centonze Frohlich, Joseph R. Lakowicz, Douglas B. Murphy, Kenneth R. Spring, and Michael W. Davidson. Basic concepts in fluorescence. `https://www.olympus-lifescience.com/en/microscope-resource/primer/techniques/fluorescence/fluorescenceintro`.

[19] Will Hossack. Operation of simple lens. `https://www2.ph.ed.ac.uk/~wjh/teaching/mo/slides/lens/lens.pdf`.

[20] Sibarita JB. Microscopy techniques. advances in biochemical engineering. volume 95, pages 11–14.

[21] Anton M. Jopko. Fraunhofer diffraction by a circular aperture. `http://math.jbpub.com/advancedengineering/docs/Project15.4_FraunhaferDefractionCircularApature.pdf`.

[22] Douglas A. Kerr. Determining mtf with a slant edge target, issue 2. pages 11–14, 2010.

[23] J N Caron, N.M. Namazi, R L Lucke, C J Rollins, and P R Lynn. Blind data restoration with an extracted filter function. *Optics letters*, 26:1164–6, 09 2001.

[24] The Editors of Encyclopaedia Britannica. Aberration optics. `https://www.britannica.com/technology/aberration`.

[25] Peter J. Shaw. Comparison of widefield/deconvolution and confocal microscopy for three-dimensional imaging. `http://www.microscopist.co.uk/wp-content/uploads/2017/04/Shaw_Handbook_ch23_05.pdf`.

[26] Ferréol Soulez, Denis Fortun, Guillaume Schmit, Arne Seitz, Romain Guiet, Cédric Vonesch, Michael Unser, Daniel Sage, and Lauréne Donati. Deconvolutionlab2: An open-source software for deconvolution microscopy. In *Methods*, volume 115, 2017.

[27] Kenneth R. Spring, Brian O. Flynn, John C. Long, and Michael W. Davidson. Spatial resolution in digital imaging. `https://www.microscopyu.com/tutorials/spatial-resolution-in-digital-imaging`.

[28] Tsardis Vangelis. Measurement and modeling of point spread function for improving the spatial resolution in microscopy. diploma thesis, Technical University of Crete, October 2017.

[29] Wes Wallace, Lutz H. Schaefer, and Jason R. Swedlow. Introduction to deconvolution. `https://www.olympus-lifescience.com/en/microscope-resource/primer/digitalimaging/deconvolution/deconintro`.

[30] Hamid R. Sheikh Zhou Wang, Alan C. Bovik and Eero P. Simoncelli. Image quality assessment: From error visibility to structural similarity. `https://ece.uwaterloo.ca/~z70wang/publications/ssim.html`.